Advanced Gravitational Wave Detectors and Detection: Arm Length Stabilization and Directed Searches for Isolated Neutron Stars

by

Jaclyn R. Sanders

A dissertation submitted in partial fulfillment
of the requirements for the degree of
Doctor of Philosophy
(Physics)
in The University of Michigan
2016

Doctoral Committee:

Professor Keith Riles, Chair
Professor Fred C. Adams
Professor Dante E. Amidei
Associate Professor Oleg Y. Gnedin
Professor Timothy A. McKay

Babcia - ja cię kocham.

ACKNOWLEDGEMENTS

Every nineteen year old kid applying to a doctoral program should be sent a kind but firm letter telling them to go do something else for a year - if only so they can commiserate with friends over a very stiff drink. Since I was too stubborn to even consider that possibility, I have to thank everyone who helped me deal with the consequences of that youthful indiscretion.

John, you stuck with me through the worst, celebrated me at my best, gave me perspective, and helped me thrive. In the words of Constantine Cavafy, I "hope the voyage is a long one / full of adventure, full of discovery".

Mom, you encouraged my love of science, up to and including letting me read about the industrial hygiene of abattoirs and write my eighth grade research paper on anthrax. I'm grateful to have you as a role model and proud to carry on the tradition of strong, stubborn Sanders women.

Dad, you taught me how to use power tools, which got me my first job, which got me my SURF position at Hanford, which got me here. So really, this is all your fault.

Keith Riles, thank you for your guidance, mentorship, and most of all patience. I am so proud of the work I've done with LIGO, and none of it would have happened if you hadn't taken me on and worked with me while I put myself back together after the disaster that was my first few years.

Daniel Sigg, I may not have ever told you, but when describing our relationship, I call you "the grizzled old trainer to my 80s montage". I learned so many things working at Hanford, but above all, I got my confidence back. I look forward to working with you in the future, and I especially look forward to eating more of your cooking!

Dick Gustafson, thank you for your unshakeable faith in how “the girl scientist” can and will do something worthy of meeting the King of Sweden.

Alexa, Sheila, and all my friends at LIGO Hanford - I have never had more fun working late nights and weekends, and wouldn’t have wanted to be exiled to a radioactive wasteland with anyone else.

This thesis has LIGO document number P1500234.

TABLE OF CONTENTS

CHAPTER

LIST OF FIGURES

Figure

LIST OF TABLES

Table

LIST OF APPENDICES

Appendix

LIST OF ABBREVIATIONS

CBC compact binary coalescence

GRB gamma ray burst

NS-NS neutron star-neutron star

NS-BH neutron star-black hole

BH-BH black hole-black hole

CMB cosmic microwave background

ITM input test mass

ETM end test mass

aLIGO Advanced Laser Interferometer Gravitational-Wave Observatory

LIGO Laser Interferometer Gravitational-Wave Observatory

PRM power recycling mirror

PRC power recycling cavity

SRM signal recycling mirror

SRC signal recycling cavity

ISI internal seismic isolation

HEPI hydraulic external pre-isolator

LISA Laser Interferometer Space Antenna

AdV Advanced Virgo

KAGRA KAmiokande GRAvitational Wave Telescope

eLISA evolved LISA

DECIGO DECi-hertz Interferometer Gravitational Wave Observatory

ESA European Space Agency

iLIGO Initial LIGO

ISC Interferometer Sensing and Control

LSC Length Sensing and Control

PDH Pound-Drever-Hall

PSL Pre-Stabilized Laser

ALS Arm Length Stabilization

LLO LIGO Livingston Observatory

LHO LIGO Hanford Observatory

DRMI Dual-Recycled Michelson Interferometer

OAT One Arm Test

HIFO-Y Half Interferometer Test Y

HIFO-XY Half Interferometer Test XY

IMC Input Mode Cleaner

FSR free spectral range

PLL phase-locked loop

FWHM full width at half maximum

TCS Thermal Compensation System

WFS wavefront sensor

SSB solar system barycenter

SNR signal-to-noise ratio

LAT Large Area Telescope

FSSC Fermi Science Support Center

3FGL Third Fermi Large Area Telescope Source Catalog

SFT Short Fourier Transform

FFT Fast Fourier Transform

ABSTRACT

Advanced Gravitational Wave Detectors and Detection: Arm Length Stabilization and Directed Searches for Isolated Neutron Stars

by

Jaclyn R. Sanders

Chair: Keith Riles

The equations of General Relativity admit wave solutions, known as gravitational waves. Gravitational waves have been indirectly detected through observations of the decay of binary neutron star orbits, but have yet to be observed directly. Advanced LIGO aims to make the first direct detection of gravitational waves using a network of two interferometric gravitational wave detectors. Observations of gravitational waves would not only verify an important prediction of general relativity, but also provide information about some of the most extreme environments in the universe, such as supernovae, black holes, and neutron stars. This thesis covers issues related to both the operation of the Advanced LIGO interferometer and its potential use for neutron star multimessenger astronomy. Principal results include a method for dynamic characterization of long Fabry-Perot optical cavities, the implementation of an auxiliary differential wavefront sensing subsystem for Advanced LIGO arm locking, and the development of a search method for gravitational waves from unassociated gamma-ray emitters in the Fermi 3FGL catalog.

CHAPTER I

Introduction

Despite its mathematical complexity, the theory of general relativity is easily explained to a child. When presented with a taut rubber sheet and a selection of weighted balls, children will roll the balls across the sheet, observing them interact as they warp the "spacetime" around them. Of course, this generally occurs after they are discouraged from their first impulse - to throw the balls into the sheet, violently shaking the simulated spacetime. The emergence of waves in Einstein's gravity is no surprise to the science educator.

When Einstein predicted their existence in 1916, gravitational waves were thought to be unobservably small. Now, almost a century later, the Advanced LIGO project seeks the first direct detection of gravitational waves. Such a detection could distinguish between General Relativity and alternative theories of gravity, probe the interiors of neutron stars, and shed light on black holes.

The Advanced LIGO project would not be possible without contributions from hundreds of scientists and engineers from universities and institutions around the world, in fields ranging from applied statistics to structural engineering. This thesis covers work done during the commissioning of the Advanced LIGO interferometer, bringing the most sensitive gravitational detector to date online, as well as the development of a search for gravitational waves from unknown neutron stars, preparing for a new era of multimessenger astronomy.

In Chapter II, gravitational waves are derived from the equations of general relativity, their predicted properties are discussed, and the indirect evidence for the existence of gravitational waves is reviewed. Chapter III discusses the theory of interferometric gravitational wave detection and the technological basis of the Advanced Laser Interferometer Gravitational-Wave Observatory (aLIGO) detectors. Chapter V reviews the properties of neutron star electromagnetic and gravitational wave emission, the methods used to search for continuous gravitational waves, and the potential contributions of gravitational wave observations to the study of neutron stars.

Original work by the author is covered in Chapter IV and Chapter VI. The author's contributions to the commissioning of the aLIGO Interferometer Sensing and Control (ISC) system and lock acquisition procedure are discussed in Chapter IV, including the characterization of the aLIGO arm cavity optics and thermal compensation systems and the development of an auxiliary optic stabilizer using differential wavefront sensing. Chapter VI presents preliminary results from a pilot search for gravitational waves from unassociated sources catalogued by the Fermi gamma-ray telescope developed by the author.

CHAPTER II

Gravitational Waves

2.1 Gravitational Waves in General Relativity

2.1.1 General Relativistic Model of Gravity

Gravitational waves are a fundamentally relativistic effect, and to understand their origin, we must consider them in the context of Einstein's *general theory of relativity* (General Relativity).

Newton's law of universal gravitation, as presented in the *Principia Mathematica*, was a triumph of early scientific thought. Previous scientific laws, such as Hooke's law of elasticity and Kepler's laws of orbital motion, were solely phenomenological descriptions. They made no attempt to articulate an underlying mechanism for behaviors observed on scales ranging from falling apples to orbiting planets. Newton's insight that gravitational force was a universal property of matter was profound and influential, but even he found fault in this description of gravity. Newtonian gravity requires instantaneous transmission of force, has no clear mechanism of action, and does not explain the connection between gravitational and inertial mass. General Relativity solved these problems by completely changing the concepts of gravity, space, and time.

The motivation for General Relativity started with the principle of special rela-

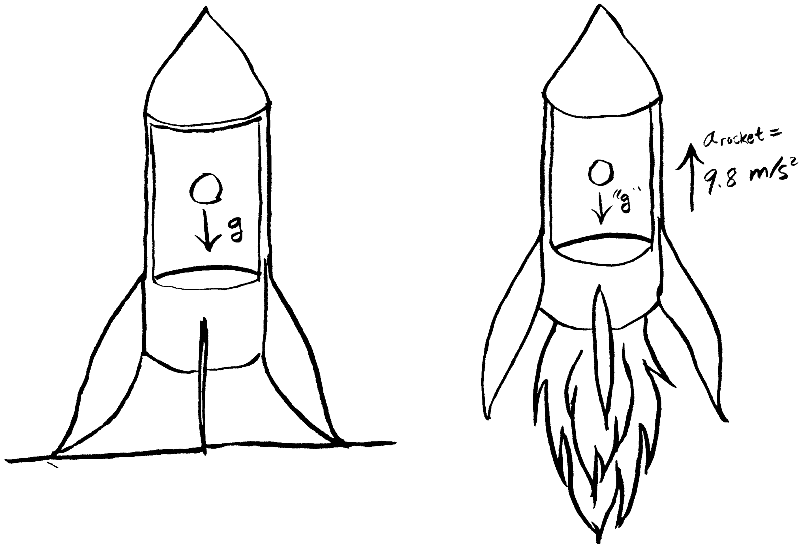

Figure 2.1: Illustration of the equivalence principle. On the left, the rocket is at rest on the surface of the earth. On the right, the rocket is accelerating at 9.8 m/s^2 in the absence of gravity. To an observer inside the rocket, the ball appears to fall with acceleration g in both cases.

tivity, which states that there is no privileged inertial frame of reference. Einstein extended this to the *principle of general covariance*, which states that the laws of physics are invariant under arbitrary coordinate transformation, as coordinate systems are not a fundamental physical property.

Einstein described the connection between general covariance and gravity as his "happiest thought" - *"For an observer falling from the roof of a house, the gravitational field does not exist"*. That is, for a freely falling system, the gravitational field can be locally eliminated by a coordinate transformation into an accelerating frame. The thought experiment that this suggests, shown in Figure 2.1, has been exploited by countless writers of speculative fiction to produce artificial gravity. Consider dropping a test particle in a windowless laboratory. Our intuition for the behavior of particles on Earth suggests that we should expect the particle to accelerate toward the Earth at $g = 9.8\ \mathrm{m} \cdot \mathrm{s}^{-2}$. The equivalence principle states that the same result would occur if the laboratory was accelerating upward at g. Therefore, producing artificial gravity in a space station is as simple as keeping the station accelerating at a constant rate. The great insight of the equivalence principle is that all gravity is artificial.

The mathematical representation that follows from the equivalence principle describes gravitational fields as the result of the curvature of spacetime in the presence of matter. The presence of mass-energy causes spacetime to curve. Particles then follow the shortest possible distances over the curved surfaces, or *geodesics*, giving the appearance of gravitational pull. As summarized by John A. Wheeler, *"spacetime tells matter how to move, matter tells spacetime how to curve."*

A full mathematical treatment of General Relativity is beyond the scope of this work; the following brief introduction to the quantities and concepts needed for discussing the generation of gravitational waves summarizes ideas explained in numerous textbooks on the subject, including [53], [119], and [56].

For the flat spacetime of special relativity, the *spacetime interval* is

$$ds^2 = -c^2 dt^2 + dx^2 + dy^2 + dz^2. \tag{2.1}$$

Introducing the Einstein convention of summing over repeated indices, this can be expressed as

$$ds^2 = \eta_{\mu\nu} dx^\mu dx^\nu \tag{2.2}$$

where $\eta_{\mu\nu}$ is the Minkowski metric (2.3),

$$\eta_{\mu\nu} = \begin{pmatrix} -1 & 0 & 0 & 0 \\ 0 & 1 & 0 & 0 \\ 0 & 0 & 1 & 0 \\ 0 & 0 & 0 & 1 \end{pmatrix}. \tag{2.3}$$

The spacetime interval can be generalized to any metric $g_{\mu\nu}$,

$$ds^2 = g_{\mu\nu} dx^\mu dx^\nu. \tag{2.4}$$

To mathematically describe curved space, we use the covariant equation of motion,

$$\frac{d^2 x^\nu}{dt^2} = -\Gamma^\nu_{\lambda\rho} \frac{dx^\lambda}{dt} \frac{dx^\rho}{dt} \tag{2.5}$$

where $\Gamma^\nu_{\lambda\rho}$ is the Christoffel symbol, or connection coefficient, defined in relation to the metric by

$$g_{\mu\nu} \Gamma^\nu_{\lambda\rho} = \frac{1}{2} \left[\frac{\partial g_{\mu\lambda}}{\partial x^\rho} + \frac{\partial g_{\mu\rho}}{\partial x^\lambda} - \frac{\partial g_{\lambda\rho}}{\partial x^\mu} \right]. \tag{2.6}$$

This is used to define the Riemann curvature tensor,

$$R^\alpha_{\beta\gamma\delta} = \frac{\partial \Gamma^\alpha_{\beta\delta}}{\partial x^\gamma} - \frac{\partial \Gamma^\alpha_{\beta\gamma}}{\partial x^\delta} + \Gamma^\alpha_{\gamma\epsilon} \Gamma^\epsilon_{\beta\delta} - \Gamma^\alpha_{\delta\epsilon} \Gamma^\epsilon_{\beta\gamma}, \tag{2.7}$$

which defines three useful quantities for General Relativity. Contracting two indices of the Riemann tensor forms the Ricci tensor,

$$R_{\beta\gamma} = R^\alpha_{\beta\alpha\gamma}. \tag{2.8}$$

Applying the metric to the Ricci tensor forms the Ricci scalar R:

$$R \equiv g^{\mu\nu} R_{\mu\nu} \tag{2.9}$$

The Ricci tensor and Ricci scalar are used to define the Einstein tensor $G_{\alpha\beta}$:

$$G_{\alpha\beta} = R_{\alpha\beta} - \frac{1}{2} g_{\alpha\beta} R \tag{2.10}$$

which appears in the *Einstein field equation*,

$$G_{\alpha\beta} = \frac{8\pi G}{c^4} T_{\alpha\beta}. \tag{2.11}$$

$T_{\alpha\beta}$ is the stress-energy tensor,

$$T_{\alpha\beta} = \left[\begin{array}{c|c} \begin{pmatrix} \text{mass density} \\ \rho \end{pmatrix} & \begin{pmatrix} \text{momentum density} \\ \mathbf{j} \end{pmatrix} \\ \hline \begin{pmatrix} \text{momentum density} \\ \mathbf{j} \end{pmatrix} & \begin{pmatrix} \text{stress tensor} \\ \mathbf{S} \end{pmatrix} \end{array} \right]. \tag{2.12}$$

2.1.2 The Nature of Gravitational Waves

The derivation of gravitational waves begins with the assumption that the metric of interest can be expressed as a small perturbation $h_{\mu\nu}$ from the Minkowski metric,

$$g_{\mu\nu} = \eta_{\mu\nu} + h_{\mu\nu}. \tag{2.13}$$

Substituting into the expressions for the Ricci scalar and tensor, applying the Lorentz gauge, and dropping terms of $O(h^2)$ (see [56][119][53]), we find the linearized Einstein equation,

$$\Box h_{\mu\nu} = \frac{16\pi G}{c^4} T_{\mu\nu}, \tag{2.14}$$

where the d'Almebertian $\Box \equiv \left(\nabla^2 - \frac{1}{c^2} \frac{\partial^2}{\partial t^2} \right)$. For the vacuum case,

$$\Box h_{\mu\nu} = 0, \tag{2.15}$$

and plane wave solutions can be found:

$$h_{\mu\nu}(x) = \epsilon_{\mu\nu} e^{ik_\alpha x^\alpha} \tag{2.16}$$

These solutions represent a plane wave propagating at the speed of light in the direction $\hat{k}$. There is residual gauge freedom in this expression, and an appropriate choice of coordinates reduces the degrees of freedom in the polarization tensor $\epsilon_{\mu\nu}$ to two. A convenient choice is the *transverse traceless* gauge, corresponding to coordinates defined by the world lines of freely falling masses [147]. In this gauge, for a wave propagating along the $\hat{z}$ axis, an arbitrary wave can be written as the sum of two polarization components, ϵ_+ and $\epsilon_\times$, where

$$\epsilon_+ = \begin{pmatrix} 0 & 0 & 0 & 0 \\ 0 & 1 & 0 & 0 \\ 0 & 0 & -1 & 0 \\ 0 & 0 & 0 & 0 \end{pmatrix} \tag{2.17}$$

and

$$\epsilon_\times = \begin{pmatrix} 0 & 0 & 0 & 0 \\ 0 & 0 & 1 & 0 \\ 0 & 1 & 0 & 0 \\ 0 & 0 & 0 & 0 \end{pmatrix} \tag{2.18}$$

The plus and cross polarizations of gravitational waves are a signature of General Relativity. Alternative theories of gravity, such as scalar-tensor theories, admit as many as six polarizations of gravitational waves. These polarizations are shown in Figure 2.2.

The physical effect of a passing gravitational wave can be determined through examining its effect on a set of test particles. A single point in space cannot demonstrate the effect of a gravitational wave. To prove this, consider a particle at rest, $x^\mu = (c, 0, 0, 0)$. The motion of this particle will be determined by the geodesic equation (2.5). For a particle initially at rest, this can be simplified to

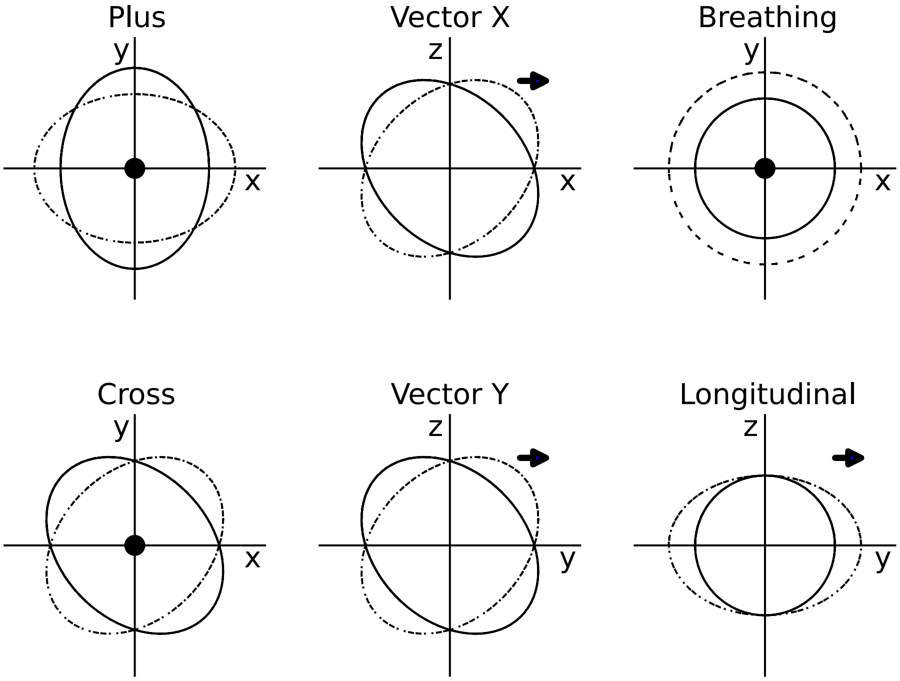

Figure 2.2: The effect of the six possible polarizations of gravitational waves on a ring of test particles. The arrow indicates the direction of travel of the gravitational wave, with a dot indicating a gravitational wave traveling out of the page. The plus and cross polarizations are the only polarizations allowed in General Relativity; the other four are permitted in alternative theories.

$$\left(\frac{\partial x^\mu}{\partial \tau}\right) = -c^2\Gamma^\mu_{00} \tag{2.19}$$

For the transverse-traceless gauge, $h_{\nu 0} = h_{0\nu} = h_{00} = 0$, and the Christoffel symbol Γ^μ_{00} goes to zero.

$$\Gamma^\mu_{00} = \frac{1}{2}\eta^{\mu\nu}(\partial_0 h_{\nu 0} + \partial_0 h_{0\nu} - \partial_\nu h_{00}) = 0 \tag{2.20}$$

To observe the effect of gravitational waves, we must consider the separation between two particles. Let two particles have an infinitesimal separation ξ, such that $dx^\mu = (0, \xi, 0, 0)$. The spacetime interval ds in a metric perturbed by the passage of a plus-polarized gravitational wave, $h_{\mu\nu} = h\epsilon_+ e^{ik^\alpha x^\alpha}$, is given by:

$$\begin{aligned} ds &= \sqrt{g_{\mu\nu}dx^\mu dx^\nu} && (2.21)\\ &= \xi\sqrt{\eta_{11} + h_{11}} && (2.22)\\ &\approx \xi(1 + \frac{1}{2}he^{ik^\alpha x^\alpha}) && (2.23) \end{aligned}$$

Similarily, for separations in the x^2 direction, $\epsilon_{22} = -1$ and $ds \approx \xi(1 - \frac{1}{2}he^{ik^\alpha x^\alpha})$. In the transverse traceless gauge, the polarization is zero for the direction of propagation, defined here as the x^3 direction. To be consistent with General Relativity, gravitational waves must be transverse to their direction of propagation both in mathematical expression and physical effect.

2.1.3 The Energy Scale of Gravitational Waves

The generation of gravitational waves can be described through analogy with electromagnetic waves. Standard analyses of electromagnetic waves consider the production of radiation by terms of a multipole expansion of increasing order. The monopole term for electromagnetism, $L_{EM\,monopole} \propto \ddot{q}$, is necessarily zero due to conservation of charge. Monopole radiation is forbidden for gravitational waves as well, due to conservation of mass-energy.

The first electromagnetically radiative term is the electric dipole. The luminosity of electric dipole radiation is given by [86]

$$L_{electric\,dipole} = \frac{2}{3}e^2\vec{a}^2 = \frac{2}{3}\ddot{d}^2. \tag{2.24}$$

This mode of gravitational radiation will be generated by the second derivative of the mass dipole.

$$\begin{aligned} d_{mass} &= \sum_A m_A x_A & (2.25)\\ \dot{d}_{mass} &= \sum_A m_A \dot{x}_A & (2.26)\\ &= \sum_A p_A & (2.27)\\ \ddot{d}_{mass} &= \sum_A \dot{p}_A. & (2.28) \end{aligned}$$

Therefore, mass "electric" dipole radiation is produced by the change in the momentum of the particles in the source. Conservation of momentum requires this to be zero at all times, forbidding gravitational radiation from this mode.

For magnetic dipole radiation, the luminosity is proportional to the second derivative of the magnetic moment, $\ddot{\mu}$. The mass analogue to the magnetic moment is the angular momentum:

$$\vec{\mu}_{mass} = \sum_A (\text{position}) \times (\text{current}) = \sum_A \vec{r}_A \times m\vec{v}_A = \vec{J}. \tag{2.29}$$

As the mass "magnetic" moment is identical to the angular momentum, conservation of angular momentum disallows mass "magnetic" dipole radiation.

Fortunately for the aspiring observer of gravitational waves, no such conservation law prohibits mass quadrupole radiation. Electric quadrupole radiation has luminosity

$$L_{electric\ quadrupole} = \frac{1}{20}\dddot{Q}^2 \equiv \frac{1}{20}\dddot{Q}_{jk}\dddot{Q}_{jk}, \tag{2.30}$$

where

$$Q_{jk} \equiv \sum_A e_A(x_{Aj}x_{Ak} - \frac{1}{3}\delta_{jk}r_A^2). \tag{2.31}$$

The mass quadrupole is typically considered in the form of the *reduced quadrupole moment*,

$$I_{jk} = \int dV\rho(r)(x_j x_k - \frac{1}{3}\delta_{jk}r^2). \tag{2.32}$$

As radiation is dominated by the lowest allowed multipole moment, gravitational waves are primarily quadrupolar in nature. Gravitational waves are generated by the second derivative of the reduced quadrupole moment [144],

$$h_{\mu\nu}(t,\vec{x}) = \frac{2G}{Rc^4}\ddot{I}_{\mu\nu}. \tag{2.33}$$

The energy scale set by the leading term is $2G/c^4 \approx 1.7 \times 10^{-44}\ \mathrm{m}^{-1} \cdot \mathrm{kg}^{-1} \cdot \mathrm{s}^2$. Therefore, an observable gravitational wave requires values of $\ddot{I}$ unattainable by an artificial generator. As a demonstration, consider a system described by Saulson [147]. A rotating dumbbell consisting of masses of 1000 kg connected by a rod 2 meters in length and rotating at $f_{rot} = 1$ kHz (see Figure 2.3) will produce gravitational waves of amplitude

$$h_{dumbbell} = 2.6 \times 10^{-33}\mathrm{m} \times \frac{1}{R}. \tag{2.34}$$

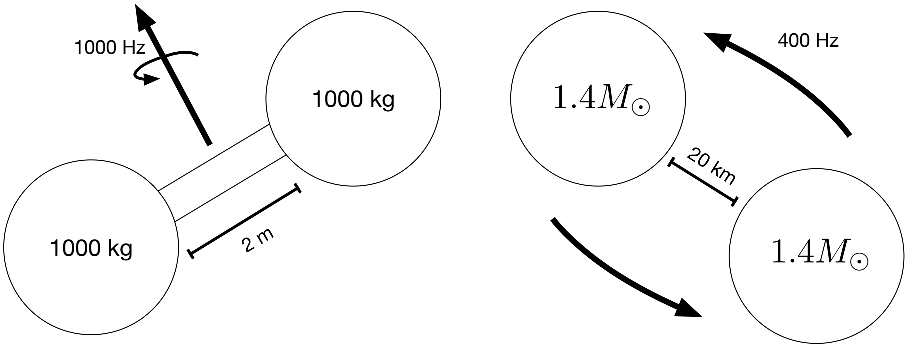

Figure 2.3: Left image: "laboratory" gravitational wave generator discussed in text. Right image: Neutron star binary with values discussed in text.

The requirement that we measure in the wave zone, $R > \lambda$, sets our minimum measurement distance at $\lambda = c/1$ kHz ≈ 300 km. At this distance, the gravitational wave amplitude from the rotating dumbbell is

$$h_{lab} = 9 \times 10^{-39}. \tag{2.35}$$

Realistic versions of this calculation are even more discouraging, as attaining even this small strain requires ignoring the constraints set by the tensile strength of structural steel [119].

Where, then, should the aspiring observer search for gravitational waves? Begin with the luminosity of gravitational waves [119],

$$L_{GW} = \frac{G}{5c^5}\langle \dddot{I}_{jk}\dddot{I}_{jk}\rangle. \tag{2.36}$$

Here, the leading term is $O(10^{-53})$. The third derivative of the reduced quadrupole moment can be approximated by $\left(E_{kin}^{NS}/T\right)^2$, where E_{kin}^{NS} is the non-symmetric kinetic energy of the system, and T is the crossing time. Replacing E_{kin}^{NS} with Mv_{NS}, and T with R_{system}/v_{NS}, where v_{NS} is the non-symmetric velocity and R_{system} is the system dimension, the luminosity can be rewritten as

$$L_{GW} \sim \frac{c^5}{G}\left(\frac{GM}{c^2 R_{system}}\right)^2 \left(\frac{v_{NS}}{c}\right)^6. \tag{2.37}$$

In this form, the leading constant has been inverted; the maximum gravitational wave luminosity is $O(10^{53}\ \mathrm{W})$. The next term resembles the Schwarzchild radius, the radius of a black hole of mass M.

$$r_{Schwarzchild} = \frac{2GM}{c^2}. \tag{2.38}$$

The highest possible value for $GM/c^2 R_{system}$ is 0.5; to maximize gravitational wave output, the radius of the system should approach this limit. The third term is the non-symmetric velocity in speed-of-light units; this term must be less than one. We see that an ideal system for the generation of gravitational waves consists of compact and massive objects moving at relativistic speeds. These are found only in the realm of astrophysics. An analogous system to the rotating dumbbell, two corotating 1.4 $M_\odot$ neutron stars in a circular orbit of 20 km with an orbital frequency of 400 Hz, emits gravitational waves with approximate amplitude[147]

$$h \approx \frac{10^{-21}}{d/15\ \mathrm{Mpc}}. \tag{2.39}$$

Although the strain amplitude of gravitational waves decreases as d^{-1} from the source, astrophysical systems are still promising sources of gravitational waves, as will be shown below.

2.2 Indirect Evidence for Gravitational Radiation

Astronomical observations of binary neutron star systems have indirectly confirmed the existence of gravitational waves. The first such system discovered, PSR B1913+16, consists of a radio millisecond pulsar orbiting a non-pulsing neutron star companion [162]. The stable pulse characteristics of the millisecond pulsar allow for precise measurements of the properties of the system [163][167].

$$\begin{aligned} m_1 &= 1.4393 \pm 0.0002 M_\odot && (2.40) \\ m_2 &= 1.3886 \pm 0.0002 M_\odot && (2.41) \\ a &= 6.5011 \pm 0.0005 \text{ lt-sec} && (2.42) \\ &\sim 1.949 \times 10^9 \text{ m.} && (2.43) \end{aligned}$$

Although the gravitational waves produced by this system have not been directly observed, gravitational waves have been indirectly detected from measurements of the decay of the orbital period of the neutron star system. The prediction of orbital decay due to gravitational wave emission by point masses in a Keplerian orbit was made by Peters and Mathews [132],

$$\dot{P}_b^{GR} = \frac{-192\pi G^{5/3}}{5c^5} \left(\frac{P_b}{2\pi}\right)^{-5/3} \left(1 + \frac{73}{24}e^2 + \frac{37}{96}e^4\right) (1-e^2)^{-7/2} m_1 m_2 (m_1+m_2)^{-1/3}, \tag{2.44}$$

where P_b is the orbital period and e is the eccentricity of the orbit. For PSR B1913+16, the predicted orbital decay due to gravitational radiation is

$$\dot{P}_b^{GR} = -2.402532 \pm 0.000014 \times 10^{-12}. \tag{2.45}$$

In 1989, the rate of orbital decay was measured as $\dot{P}_b = -2.427 \pm 0.026 \times 10^{-12}$, an error of approximately 1% [163]. Twenty years later, this agreement still held; in 2010, the rate of orbital decay was measured as $\dot{P}_b = -2.423 \times 10^{-12}$ (Figure 2.4). After taking into account other sources of orbital decay at the level of $\Delta\dot{P}_b = -0.027 \pm 0.005 \times 10^{-12}$, the ratio between the measured and predicted values of $\dot{P}_b$ is

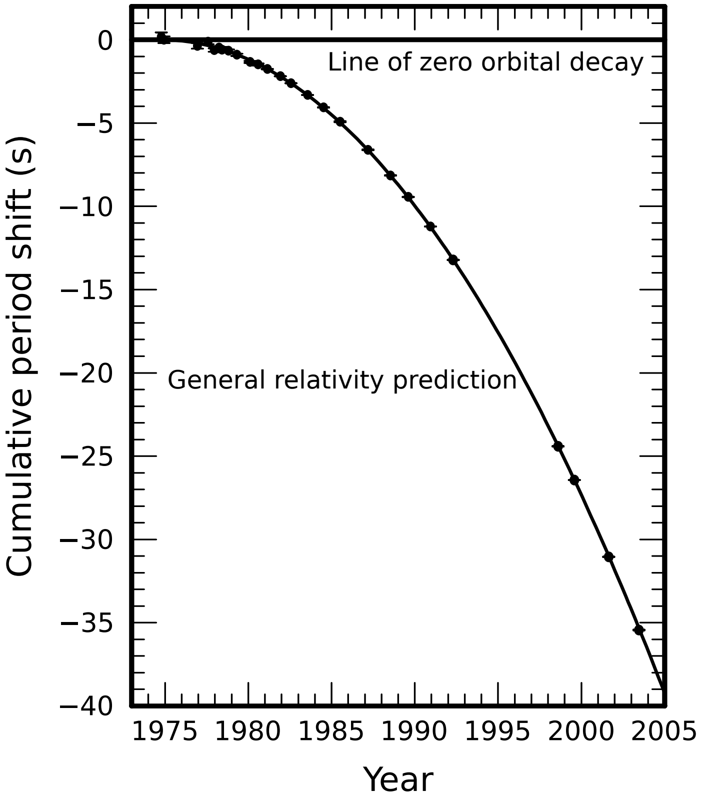

Figure 2.4: Indirect evidence for gravitational waves. The orbital decay of PSR B1913+16 agrees to within less than 0.5% of the prediction from general relativity.

$$\frac{\dot{P}_b}{\dot{P}_b^{GR}} = 0.997 \pm 0.002, \tag{2.46}$$

an error of approximately 0.5%, and within the margin of error due to uncertainty in source distance [167]. This work was awarded the Nobel Prize in Physics in 1993, "for the discovery of a new type of pulsar, a discovery which has opened up new possibilities for the study of gravitation" [125].

This effect has been observed in the other double neutron star systems discovered, most notably J0737-3039 [109][97][108], a double pulsar system consisting of a millisecond pulsar and a young pulsar in a tight orbit. For this system, the orbital decay and ratio between measurement and prediction are

$$\dot{P}_b^{meas} = -1.252(17) \times 10^{-12} \tag{2.47}$$

$$\dot{P}_b^{GR} = -1.24787(13) \times 10^{-12} \tag{2.48}$$

$$\frac{\dot{P}_b}{\dot{P}_b^{GR}} = 1.003814. \tag{2.49}$$

This is consistent with general relativity to within 0.3% [97]. The agreement between general relativistic predictions and astrophysical systems is powerful indirect evidence for the existence of gravitational waves.

2.3 Projected Sources of Gravitational Waves

The potential sources of gravitational waves are typically divided into four categories based on knowledge of signal characteristics and expected duration of the signal. Compact binary coalesences, mergers of compact objects, have well-modeled signals and short durations. Continuous wave signals have well modeled signals with longer duration. Burst signals are unmodeled transients from high energy processes ranging from supernovae to cosmic strings. Stochastic backgrounds of gravitational waves take the form of a stationary Gaussian distribution of incoherent signals.

As this work focuses on the LIGO instruments and their data, the following sections address sources that are predicted to emit in the audio band ($\sim$1Hz $-$ 10kHz), the operational frequencies of ground-based gravitational wave detectors. Sources of interest for space-based detectors, including white dwarf binaries and supermassive black hole inspirals, emit in the mHz range. Pulsar timing arrays, sensitive to gravitational waves of nHz frequencies, have already placed upper limits on the stochastic background of gravitational waves from supermassive black hole binaries. For more information about gravitational waves in the mHz-nHz regime, see references [146] and [142].

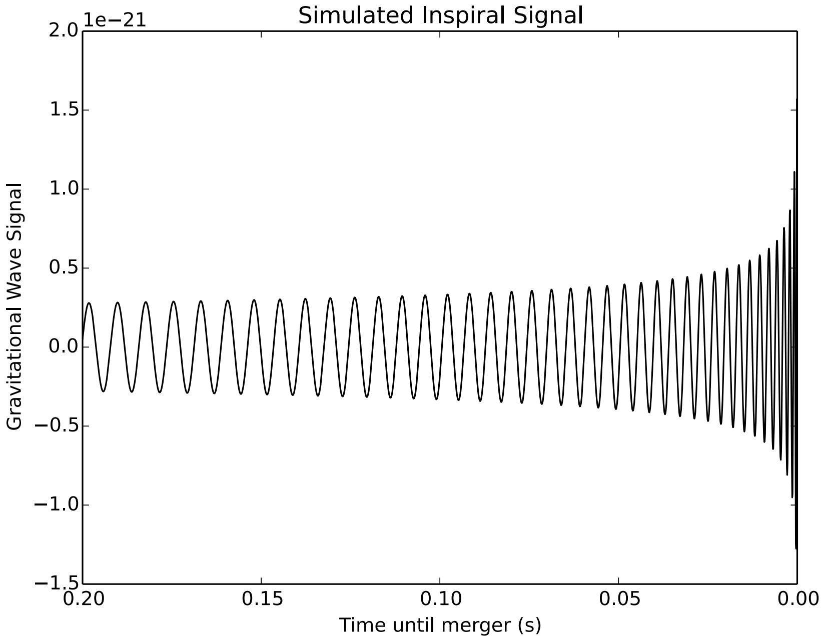

Figure 2.5: Simulated gravitational wave signal from compact binary coalesence, using equations 2.50 and 2.51, assuming chirp mass $M = 2M_\odot$ at distance $d = 15$ Mpc.

2.3.1 Compact Binary Coalescence

As discussed in section 2.2, the orbits of neutron star binaries decay due to gravitational wave emission. The end result of this orbital decay is the merger of the two neutron stars in a compact binary coalescence (CBC). This is a promising source for ground-based gravitational wave detections, as the signal has a high amplitude and well modeled evolution. The inspiral phase prior to the collision can be determined using post-Newtonian approximation, the merger can be modeled using full numerical relativity methods, and the ringdown phase can be modeled using the quasinormal oscillations of black holes [56].

The frequency evolution of the characteristic CBC "chirp" signal (Figure 2.5) is

$$f_{GW}(t) = 1.9 \text{ Hz} \left(\frac{1.4M_\odot}{M}\right)^{5/8} \left(\frac{1 \text{ day}}{\tau}\right)^{3/8} \tag{2.50}$$

and the amplitude evolution is

$$h_0(t) = 1.7 \times 10^{-23} \left(\frac{15\text{Mpc}}{d}\right) \left(\frac{1 \text{ day}}{\tau}\right)^{1/4} \left(\frac{M}{1.4M_\odot}\right)^{5/4} \tag{2.51}$$

where τ is the time remaining until coalescence and d is the distance to the source.

Although binary star systems are common, the conditions required to form an observable coalescing binary are strict. The component stars of the system must be large enough to collapse to form a neutron star or black hole, the system must not be disrupted during the collapse, and the resulting binary must be close enough that a coalescence will occur within the age of the Universe. Alternatively, a coalescing binary can be formed through N-body interactions in dense stellar enviroments, such as globular cluster cores [37]. Rate estimates are made through population synthesis models or extrapolation from known systems. A simple estimate can be made by taking the binary pulsar J0737-3039 as a representative system [56]. J0737-3039 is ~ 200 Myr old, and will coalesce in ~ 85 Myr. Given that pulsar surveys are estimated to detect approximately one in 10^4 such systems, the rate of binary mergers in the Milky Way can be estimated to be

$$R_G \sim \frac{10^4}{285 \text{ Myr}} \approx 40 \text{ Myr}^{-1}. \tag{2.52}$$

Conversion of the observed rate of merger in the Milky Way to a rate density for the local Universe requires estimates based on star formation rates. Given the star formation rate in the Milky Way ($\sim 3M_\odot$/yr) and the star formation rate in the local universe ($\sim 0.03M_\odot$/yr), the rate density $\mathcal{R}$ is estimated to be [56],

$$\mathcal{R} \approx 0.01\text{Mpc}^{-3} R_G \sim 4 \times 10^{-7}\text{yr}^{-1}\text{Mpc}^{-3}. \tag{2.53}$$

The estimates of neutron star-neutron star (NS-NS) inspiral rates are firmer, as there are known systems that will merge within a Hubble time (~ 13 Gyr). There is an

Source	R_{low}	$R_{\text{realistic}}$	R_{high}
NS-NS	1	100	1000
NS-BH	0.05	3	100
BH-BH	0.01	0.4	30

Table 2.1: Summary of rates for compact binary coalescence signals in units of $\text{MWEG}^{-1}\text{Myr}^{-1}$.

additional external check on models of neutron star mergers. The merger hypothesis states that the disruption of neutron stars during mergers is the source of short hard gamma ray bursts, and estimates of merger rates are consistent with observed gamma ray burst (GRB) rates [128]. The rates for neutron star-black hole (NS-BH) and black hole-black hole (BH-BH) systems are more speculative, as no such system has been observed.

After a CBC signal is detected, comparisons of the signal to the detailed models can be used to answer many scientific questions. The inspiral and merger are strong-field gravitational processes that can test modified theories of gravity. Measurements of tidal disruption during the inspiral can probe the neutron star equation of state [99]. Inspirals can potentially be used as "standard sirens", a gravitational analog to the standard candles of Type 1A supernovae. [144].

2.3.2 Continuous Waves

For the frequency band of ground-based gravitational wave detectors, the dominant source of continuous gravitational waves will likely be galactic non-axisymmetric neutron stars. These neutron stars may be isolated pulsars, or accreting pulsars in binary systems. As a large portion of this work concerns searches for gravitational waves from neutron stars, this section will provide a brief overview of material covered in more detail in Chapter V.

The signal model for continuous wave emission is a slowly evolving sinusoidal signal with $f_{GW} \propto f_{\text{rotation}}$ (Figure 2.6), with a constant of proportionality dependent on the

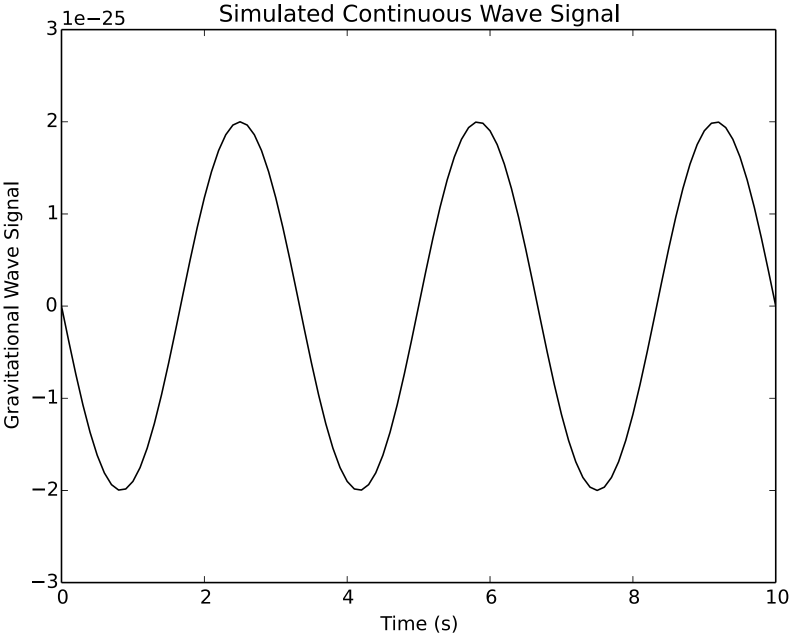

Figure 2.6: Simulated gravitational wave signal for a rotating neutron star. The frequency is twice the frequency of rotation of the Crab pulsar (29.7 Hz), and the amplitude is the $h_{95\%}$ limit for the Crab from [16].

mechanism. One model is a neutron star with a small deformation. The frequency of emission is $2f_{\text{rotation}}$, and the strength of the signal depends on the degree of non-axisymmetry in the neutron star, which we parameterize by the ellipticity,

$$\epsilon \equiv \frac{I_{xx} - I_{yy}}{I_{zz}}, \tag{2.54}$$

where I_{xx}, I_{yy}, and I_{zz} are components of the neutron star moment of inertia. The strain amplitude of the signal is

$$h_0 = \frac{4\pi^2 G I_{zz} f^2}{c^4 r}\epsilon = (1.1 \times 10^{-24}) \left(\frac{I_{zz}}{I_0}\right) \left(\frac{f_{GW}}{1 \text{ kHz}}\right)^2 \left(\frac{1 \text{ kpc}}{d}\right) \left(\frac{\epsilon}{10^{-6}}\right), \tag{2.55}$$

where d is the distance to the source and $I_0 = 10^{38}$ kg $\cdot$ m^2 is a nominal value for the neutron star moment of inertia.

A priori estimates of continuous wave strain amplitude are not made as easily as those for CBC. The ellipticity depends on the neutron star equation of state and the mechanism of non-axisymmetry production, neither of which is well understood. Estimates of the maximum strain are made based on the energy loss inferred from the decrease in electromagnetic pulse frequency, or *spindown.* For isolated stars, the *spindown limit* is the amplitude of gravitational waves that would be observed if the entirety of the observed frequency evolution of the neutron star was due to gravitational wave emission,

$$\begin{aligned} h_{spindown} &= \frac{1}{d}\sqrt{\frac{-5G}{4c^3} I_{zz} \frac{\dot{f}_{GW}}{f_{GW}}} & (2.56) \\ &= (2.5 \times 10^{-25}) \left(\frac{1 \text{ kpc}}{d}\right) \sqrt{\left(\frac{1 \text{ kHz}}{f_{GW}}\right) \left(\frac{-\dot{f}_{GW}}{10^{-10} \text{ Hz/s}}\right) \left(\frac{I_{zz}}{I_0}\right)}. & (2.57) \end{aligned}$$

Because this assumption is based on observation of electromagnetic radiation, the actual strain amplitude of gravitational waves is expected to be below the spindown limit. The spindown limits of most known pulsars are out of the range of current gravitational-wave detectors. The spindown limit has been surpassed, however, for the Crab and Vela pulsars, allowing statements to be made about the percentage of energy loss due to gravitational radiation. Gravitational wave emission from the Crab pulsar is less than $\sim 1\%$ of the observed energy loss. For the Vela pulsar, gravitational wave emission is limited to less than $\sim 10\%$ of the observed energy loss [6].

2.3.3 Bursts

A *burst* signal is a generic term for any unmodeled gravitational wave transient. The prototypical burst source is the emission of gravitational waves during a core-collapse supernova. This requires asymmetry in the explosion/implosion of a $> 8M_\odot$ star, as a spherically symmetric collapse would only admit the forbidden monopole

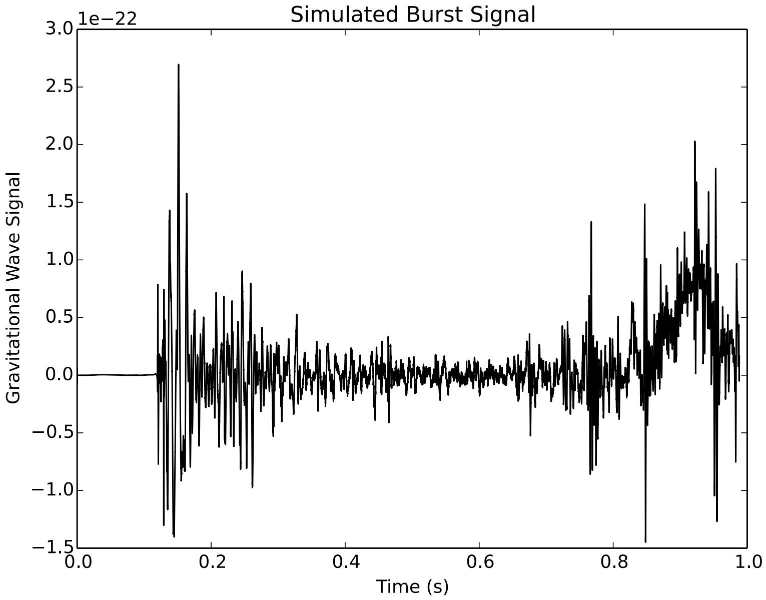

Figure 2.7: Simulated gravitational wave signal for a core-collapse supernova. The data for this plot was provided by stellarcollapse.org [160] and is from 2-D simulations of neutrino-driven core-collapse supernovae described in reference [124].

modes. Asymmetry is expected due to the observation of high transverse velocities of neutron stars found in supernovae. Although the large energy scale of supernovae suggests that gravitational wave production may be observable, the form of the signal is unknown; a simulated signal is shown in Figure 2.7.

For a burst event, we can estimate the amplitude of gravitational waves by parameterizing in terms of the gravitational wave energy, E_G [146],

$$h \sim \left(\frac{E_G}{10^{-7} M_\odot c^2}\right)^{1/2} \left(\frac{1\ \mathrm{ms}}{T}\right) \left(\frac{1\ \mathrm{kHz}}{f}\right) \left(\frac{10\ \mathrm{kpc}}{d}\right), \tag{2.58}$$

where T is the timescale of the gravitational wave signal and $d = 10$ kpc is the characteristic distance to a galactic supernova. Assuming that the nominal values of the variables in the equation hold, the initial LIGO and Virgo detectors were sensitive to gravitational waves from supernovae anywhere in the Milky Way galaxy. Unfortunately for gravitational wave detection efforts, estimates of galactic supernova rates range over $0.01-0.1\mathrm{MWEG}^{-1}\mathrm{yr}^{-1}$, with a favored rate of one galactic supernova per 40 years.

Core-collapse supernovae are not the only possible burst signals. Gravitational wave bursts could originate from more exotic phenomena, including cosmic string cusps, magnetar flares, pulsar glitches, and gravitational brehmsstrahlung radiation. Unmodeled transient gravitational waves could reveal new processes and objects invisible to the electromagnetic spectrum and entirely new to science.

2.3.4 Stochastic Background

By the central limit theorem, any superposition of unresolved incoherent sources will form a Gaussian signal distribution (Figure 2.8). These *stochastic backgrounds* allow statements to be made about the emitters without detailed knowledge of their signals or positions. However, many noise sources also form Gaussian distributions, so stochastic backgrounds must be resolved through measurement of the modulation of signals with detector position or cross-correlation between detectors with uncorrelated noise sources [56].

The quantum fluctuations in the early universe that produced the cosmic microwave background (CMB) are associated with small fluctuations in spacetime geometry. The gravitational waves produced by these fluctuations form a gravitational wave background. The CMB carries information about the universe at the time of recombination, when nuclei and electrons formed neutral atoms and the universe became transparent to electromagnetic radiation approximately 380,000 years after the Big Bang. The universe is expected to have been transparent to gravitational waves at the Planck time, $t_{Planck} = \sqrt{\hbar G/c^5} \sim 10^{-43}$ s [56]. Hence, a gravitational wave background can carry information from the very beginning of the universe.

Cosmological quantities are customarily parameterized as the ratio of their energy densities to the critical density $\rho_{crit} = 3H_0^2c^2/8\pi G$, where H_0 is the Hubble constant.

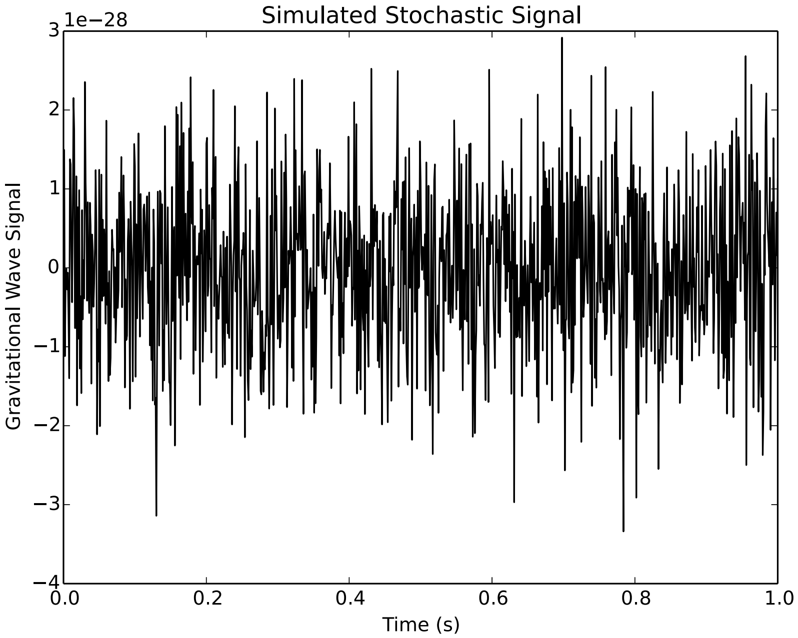

Figure 2.8: Simulated gravitational wave signal from a stochastic background. The signal was drawn from a Gaussian distribution with $\mu = 0$ and $\sigma = 1 \times 10^{-28}$.

The formal expression for energy density of the gravitational wave background is:

$$\Omega_{GW}(f) = \frac{1}{\rho_{crit}} \frac{d\rho_{GW}(f)}{d\ln(f)}. \tag{2.59}$$

$\Omega_{GW}(f)$ sets the energy scale for the power spectral density and amplitude spectral density for gravitational waves,

$$\begin{aligned} S_{GW}(f) &= \frac{3H_0^2}{10\pi^2} f^{-3}\Omega(f) && (2.60)\\ h(f) &\equiv [S_{GW}(f)]^{1/2} && (2.61)\\ &= (5.6 \times 10^{-22}) h_{100} (\Omega_{GW}(f))^{1/2} \left(\frac{100Hz}{f}\right)^{3/2} Hz^{-1/2} && (2.62) \end{aligned}$$

where $h_{100} = H_0/(100\text{km s}^{-1}\text{ Mpc}^{-1})$ [144]. The observability of gravitational waves depends on $\Omega_{GW}(f)$. Big Bang nucleosynthesis requires the gravitational wave background to be $O(10^{-5})$ or less, while inflationary arguments set the scale of gravitational wave density at $O(10^{-12})$ [56]. Measurements from the initial generation of gravitational wave detectors ruled out a gravitational wave background at the 10^{-6} level, and although second-generation detectors are expected to set limits at the 10^{-9} level, ground-based gravitational wave detectors are unlikely to be able to directly detect a primordial gravitational wave background.

Astrophysical stochastic backgrounds may prove to be of more interest to gravitational wave observations. These backgrounds arise from the superposition of many unresolved continuous wave signals. Assuming that all energy loss in observed neutron stars is due to gravitational radiation, the energy density expected from the background of all galactic rotating neutron stars is

$$\Omega_{NS} \approx 2 \times 10^{-7} \left(\frac{R}{(30\ \mathrm{yr})^{-1}}\right)^{1/2} \left(\frac{I}{I_0}\right) \left(\frac{f}{100\ \mathrm{Hz}}\right)^{2} \left(\frac{\langle d \rangle}{10\ \mathrm{kpc}}\right)^{-2}, \tag{2.63}$$

where R is the neutron star formation rate and $\langle d \rangle$ is the mean source distance [56]. Recall that the assumption of only gravitational wave emission is suspect; a physical background will be less than a few percent of this value.

Looking to the future, a particularly interesting astrophysical background is the superposition of all white dwarf binaries in the galaxy,

$$\Omega_{WDB} \approx 4 \times 10^{-8} \left(\frac{R}{(100\ \mathrm{yr})^{-1}}\right) \left(\frac{M}{M_\odot}\right)^{5/3} \left(\frac{f}{10^{-3}\ \mathrm{Hz}}\right)^{2/3} \left(\frac{\langle d \rangle}{10\ \mathrm{kpc}}\right)^{-2}. \tag{2.64}$$

Although the characteristic frequency range of continuous waves from white dwarf binaries is $O(\mathrm{mHz})$ and out of the operating range of ground-based detectors, this white dwarf background is expected to be a significant noise source for space-based detectors.

CHAPTER III

Gravitational Wave Detectors

3.1 Theory of Gravitational Wave Detectors

As of this writing, gravitational waves have not been directly detected. Neutron star binaries, such as PSR B1913+16 and J0737-3039, exhibit orbital period decay at a rate consistent with energy loss due to the production of gravitational waves. Although this is strong evidence for General Relativity, it is not a definitive measurement of the presence of gravitational radiation. The first attempts at the direct detection of gravitational waves were made by Joseph Weber. In 1960, he proposed the detection of gravitational waves through the measurement of energy deposited by gravitational waves into the resonant modes of a solid mass [166]. Weber reported anomalies attributed to gravitational waves, but these detections were never confirmed [144]. Although resonant bar detectors remain in operation and development [55], this work focuses on laser interferometric gravitational wave detectors.

Interferometric gravitational wave detectors were first proposed by Gertsenshtein and Pustovoit in a 1962 criticism of Weber's sensitivity estimates [75]. Their argument for using interferometry for the measurement of gravitational waves was that inherently relativistic light should be an effective probe of the relativistic effects of gravity. In practice, both methods have advantages; resonant mass detectors store energy for longer but only detect in narrow bands, while interferometers observe in

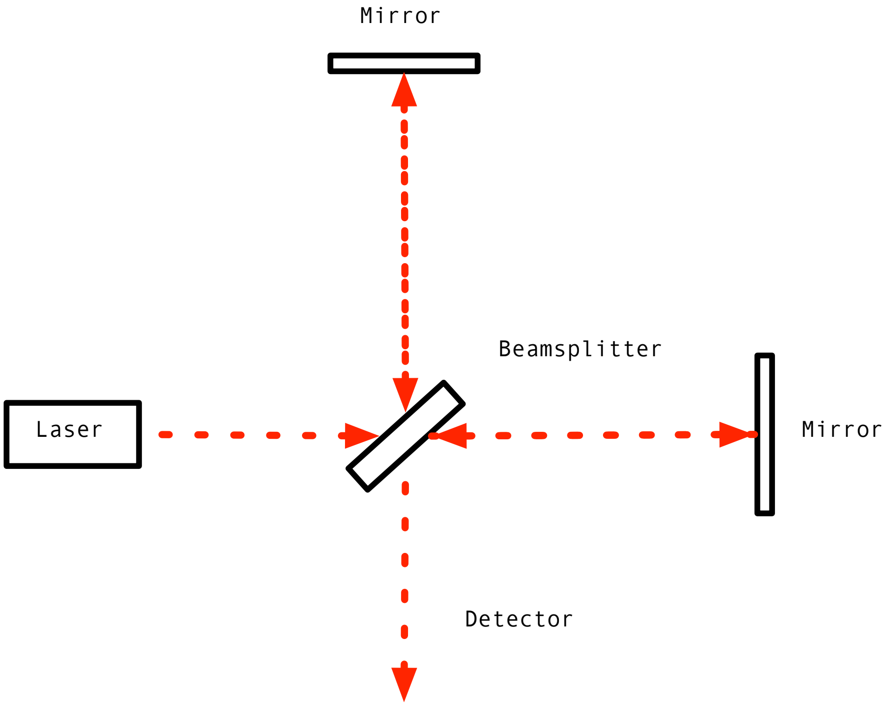

Figure 3.1: Schematic depiction of a Michelson interferometer. The input light from the laser splits at the beamsplitter, traverses each arm, reflects off the mirror at the end, recombines at the beamsplitter, and is measured at the detector at the output.

real time over broad frequency bands.

Modern gravitational wave interferometers are based on the Michelson interferometer, shown in Figure 3.1. To understand why the Michelson interferometer is useful for gravitational wave measurement, consider a time of flight measurement of a monochromatic light wave in the interferometer,

$$E_{in} = E_0 e^{i(\omega_L t - \vec{k}\cdot\vec{x})}, \tag{3.1}$$

where k is the wavevector and ω_L is the laser frequency.

For simplicity, assume the beamsplitter has equal power in transmission and reflection, with reflectivity $r = 1/\sqrt{2}$ and transmissivity $t = 1/\sqrt{2}$. Each wavefront travels down its respective arm, returns to the beamsplitter, and combines at detector at the anti-symmetric port as shown in Figure 3.1. Neglecting the thickness of the beamsplitter, the wavefronts have phases:

$$
\begin{aligned}
E_2^{(x)} &= \frac{1}{2} E_0 e^{i(\omega_L t - 2kL_x)} && (3.2)\\
E_2^{(y)} &= \frac{1}{2} E_0 e^{i(\omega_L t - 2kL_y)}. && (3.3)
\end{aligned}
$$

The magnitude of the electric field at the output port is dependent on the difference between the path lengths:

$$
\begin{aligned}
E_{out} &= \frac{1}{2} E_0 e^{i\omega_L t} \left(e^{-i2kL_x} + e^{-i2kL_y} \right) && (3.4)\\
&= E_0 e^{i(\omega_L t - kL_x - kL_y)} \frac{1}{2} \left(e^{ik(L_x - L_y)} + e^{-ik(L_x - L_y)} \right) && (3.5)\\
&= E_0 e^{i(\omega_L t - kL_x - kL_y)} \cos[k(L_x - L_y)]. && (3.6)
\end{aligned}
$$

By squaring this electric field, it is shown that the Michelson interferometer transduces path length difference to output power:

$$
\begin{aligned}
P_{out} &\equiv |E_{out}|^2 && (3.7)\\
&= E_0^2 \cos^2(k(L_x - L_y)) && (3.8)\\
&= \frac{P_{in}}{2} (1 + \cos[2k(L_x - L_y)]). && (3.9)
\end{aligned}
$$

The orthogonal beam paths of the Michelson interferometer are convenient for measuring gravitational waves because quadrupolar gravitational wave polarizations cause differential path length changes. As a demonstration, consider a plus-polarized gravitational wave, $h_+(t) = h_0 \cos(\omega_{GW} t)$, normally incident on a Michelson interferometer such that the x and y axes of the polarization are aligned with the interferometer arms [147][111]. The general spacetime interval in this case is:

$$\begin{aligned} ds^2 &= g_{\mu\nu}x^\mu x^\nu && (3.10)\\ &= (\eta_{\mu\nu} + h_{\mu\nu})x^\mu x^\nu && (3.11)\\ &= -c^2dt^2 + (1 + h_{11})dx^2 + (1 + h_{22})dy^2 + dz^2 && (3.12)\end{aligned}$$

As this experiment uses light as a probe, the changes in path length are lightlike spacetime intervals, $ds^2 = 0$. For a plus-polarized gravitational wave, $h_{11} = -h_{22} = h$, and the effect on the x-axis can be considered without significant loss of generality; only a change in sign of h is required for the y-axis solution. For a probe beam traveling in the $\hat{x}$ direction, $dy^2 = dz^2 = 0$, and

$$c^2dt^2 = [1 + h(t)]dx^2. \tag{3.13}$$

To simplify the derivation, assume that the metric perturbation caused by the gravitational wave does not change over the course of the time of flight measurement, $2\pi f_{GW}\tau_{rt} \ll 1$. For the trip from the beamsplitter to the end mirror, the time difference is

$$t_1 - t_0 = \frac{1}{c}\int_0^{L_x} \sqrt{1+h}\; dx \approx \int_0^{L_x} 1 + \frac{1}{2}h\; dx \tag{3.14}$$

and for the return trip,

$$t_2 - t_1 = -\frac{1}{c}\int_{L_x}^{0} 1 + \frac{1}{2}h\; dx. \tag{3.15}$$

Combining the two equations, the time of flight in the x arm is:

$$\tau_x = \frac{2L}{c} + \frac{hL}{c}. \tag{3.16}$$

Repeating the above integrals incorporating the change in sign for h and assuming the same nominal arm length L, the time of flight in the y arm is:

$$\tau_y = \frac{2L}{c} - \frac{hL}{c} \tag{3.17}$$

and the difference in phase between the two arms is

$$\Delta\phi = (\tau_x - \tau_y)\frac{2\pi c}{\lambda_L} = h\frac{2L}{c}\frac{2\pi c}{\lambda_L}. \tag{3.18}$$

The Michelson interferometer converts the differential length change caused by gravitational waves to phase difference between wavefronts. Unlike resonant bars, gravitational wave interferometers do not measure deposited energy; they directly measure the dimensionless strain h due to the gravitational wave,

$$h = \frac{\Delta L}{L}, \tag{3.19}$$

where ΔL is the change in length due to the gravitational wave.

3.2 Advanced LIGO: a case study in gravitational wave interferometry

Recall that gravitational wave strain is expected to be less than $h \sim 10^{-21}$. For a Michelson interferometer with kilometer-scale arms, using light with wavelength of 1 μm, the measurable strain will be of order

$$h \sim \frac{10^{-6}\text{ m}}{10^{3}\text{ m}} \sim 10^{-9}. \tag{3.20}$$

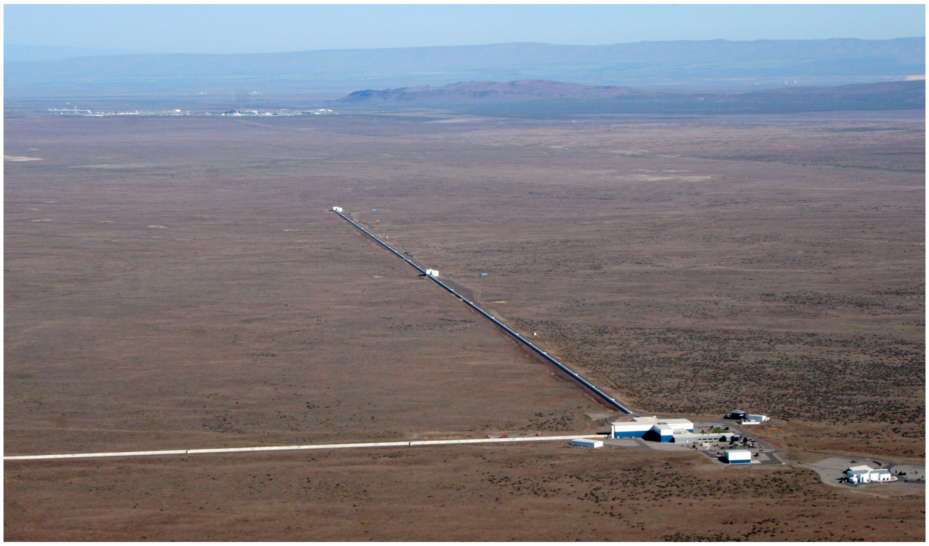

Figure 3.2: Aerial view of LIGO Hanford Observatory, Hanford, Washington. Image courtesy of LIGO Laboratory.

In a real gravitational wave detector, there are two variables that can be manipulated to span the twelve orders of magnitude required to measure a realistic gravitational wave strain - the length L can be increased, and the measurable change in length ΔL can be decreased. As this work concerns the installation and characterization of the aLIGO instrument, the implementation of gravitational wave interferometry will be considered in the context of aLIGO technology. Other interferometers will be discussed briefly in the next section.

3.2.1 The LIGO Project

Advanced LIGO is the most recent upgrade to the LIGO gravitational wave observatory network. There are two LIGO facilities: LIGO Hanford Observatory (LHO) in Hanford, Washington (Figure 3.2), and LIGO Livingston Observatory (LLO) in Livingston, Louisiana (Figure 3.3). Each of these sites houses a gravitational wave interferometer with four-kilometer long arms.

The first iteration of the LIGO interferometers was Initial LIGO (iLIGO), which ran from November 2005 to September 2007 [15]. iLIGO consisted of three interfer-

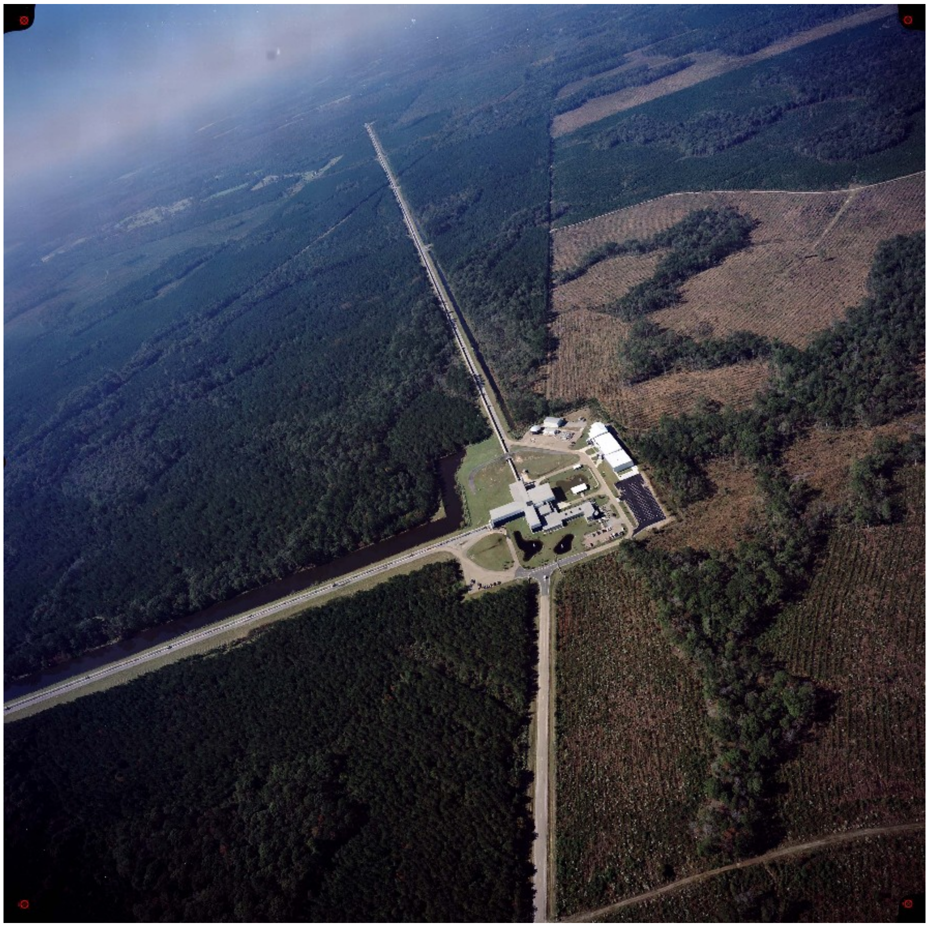

Figure 3.3: Aerial view of LIGO Livingston Observatory, Livingston, Louisiana. Image courtesy of LIGO Laboratory.

ometers; one 4-km interferometer at LLO, one 4-km interferometer at LHO, and one 2-km interferometer at LHO. The initial LIGO instrument was always intended to be upgraded to an advanced configuration [19]; estimates of compact binary coalescence rates set the initial LIGO detection rate at approximately one per 50 years [11]. The first of these upgrades was Enhanced LIGO (eLIGO), which ran from July 2009 - October 2010 [8]. The laser source was upgraded to a power of 10 W, and the readout subsystems were replaced. The most sensitive frequencies saw a 30% improvement in strain sensitivity, with a minimum instrument root-mean-square noise of 2×10^{-22} in a 100 Hz band. A factor of two improvement was achieved for the higher frequencies most directly impacted by laser shot noise. There was no direct detection of gravitational waves in either iLIGO or eLIGO, although interesting limits on astrophysical sources of gravitational waves were achieved [6][56][144].

Advanced LIGO is the first operational second-generation gravitational wave interferometer experiment. From October 2010 to March 2015, the aLIGO project upgraded the interferometers for improved sensitivity and astrophysical reach [8]. aLIGO began its first observating run on September 18, 2015.

3.2.2 A Real Gravitational-Wave Interferometer

In the theoretical description of gravitational wave measurement, the test masses are assumed to be in free fall, with differential motion solely from the gravitational wave of interest. In aLIGO, each of the core optical components is seismically isolated and mounted a pendulum to approximate free fall. To damp pendulum resonances and mitigate suspension thermal noise, aLIGO uses quadruple pendulum suspensions, as shown in Figure 3.4 [25]. The top mass and second mass are made of stainless steel, as are the wires suspending them and the fused silica penultimate mass. As the stainless steel wires in the Initial LIGO (iLIGO) suspensions contributed significant noise to the interferometer, the fused silica aLIGO optics are suspended from the penultimate

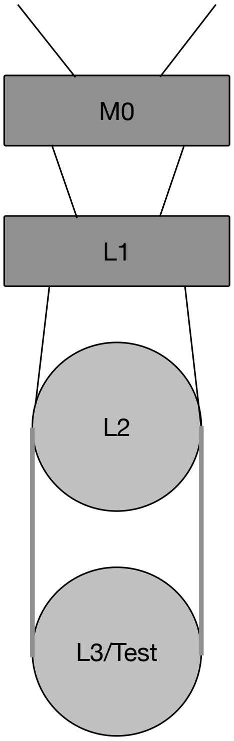

Figure 3.4: Schematic depiction of the aLIGO quadruple pendulum suspensions. The top mass (M0) and second mass (L1) are made of stainless steel, as are the wires suspending them and the penultimate mass (L2), which is made of fused silica. The fused silica test mass (L3) is bonded to the penultimate mass with fused silica fibers.

mass using fused silica fibers, which have sharper mechanical resonances and reduce the impact of suspension noise.

The aLIGO interferometer uses light to measure the differential motion of the test masses. As derived in the discussion of the electric fields in a Michelson interferometer above, the total output power of an interferometer is a function of the path length difference. To measure the change in path length difference induced by a gravitational wave, aLIGO directly measures the output power; the change in measured power on the output photodiode will contain any gravitational wave signal [25].

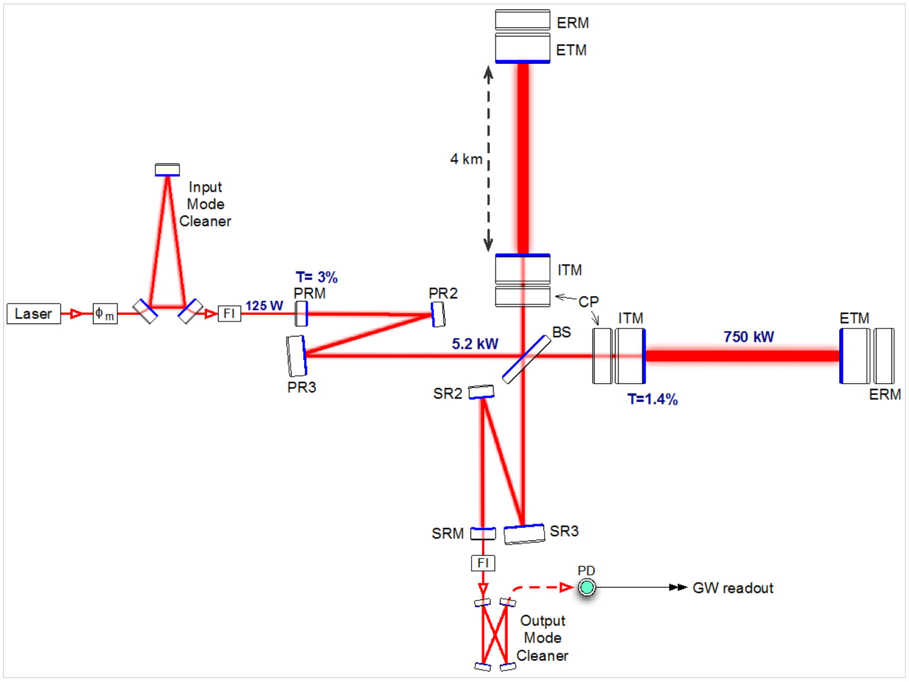

Figure 3.5: Advanced LIGO system diagram from the aLIGO Systems Description [25]. aLIGO is a dual-recycled Fabry-Perot Michelson, an enhanced version of the Michelson interferometer shown in Figure 3.1. To measure the change in path length difference induced by a gravitational wave, aLIGO directly measures the change in output power. The interferometer output is measured by a photodiode; the changes in measured power will contain any gravitational wave signal.

3.2.3 The Dual-Recycled Fabry-Perot Michelson

To achieve scientifically interesting sensitivity, aLIGO modifies the basic form of the Michelson interferometer; a simplified version of the layout is shown in Figure 3.5. The effective length of the interferometer is increased through the use of Fabry-Perot cavities in the arms, the optical power in the instrument is increased through the use of a power recycling cavity, and the output is enhanced using a signal recycling cavity.

3.2.3.1 Fabry-Perot Arm Cavities

The first possibility for strain improvement is increasing the length L of the Michelson arms. The aLIGO arms are 4 km long, and increasing their physical size by

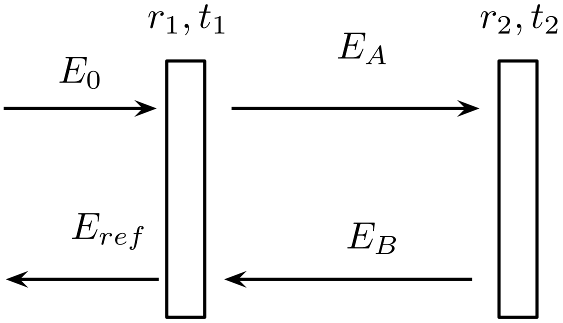

Figure 3.6: A schematic Fabry-Perot cavity, with fields labeled as in the system of equations 3.21. Light enters through the partially transmissive input mirror, resonates in the cavity, and leaves through the transmissive input mirror. In a real Fabry-Perot cavity, the input light will be Gaussian beams rather than plane waves, and the mirrors will be curved accordingly.

orders of magnitude would require a comparable investment in facilities[1]. A more space-effective solution is to increase the effective arm length through optical folding techniques. The optical delay line, used by Michelson and Morley in their 1881 ether experiment [147], is one such method; by using many mirrors separately aligned, the path traversed by light can be made many times the physical length of the beam enclosure. Harriot delay lines, which replace many mirrors with large curved mirrors with entry holes, were used in early interferometers [168] but fell out of favor due to issues with stray light contamination. Development of optical feedback control systems by Pound, Drever, and Hall [61] made optical resonant cavities viable for kilometer-scale interferometry. The advantage of Fabry-Perot cavities over delay lines is that longer effective cavities can be achieved with smaller optics.

To understand how a Fabry-Perot cavity enhances arm length, simplify the model to two partially transmissive plane mirrors with plane electromagnetic waves resonating between them, as shown in Figure 3.6. For consistency with later discussion of the LIGO instrument, label the input mirror as the input test mass (ITM) and the end mirror as the end test mass (ETM). To simplify the derivation, assume that

---

[1] Building a third-generation instrument with 40 km arms has been a subject of discussion in the advanced interferometry community; see [64].

the thickness of the mirrors is negligible and the ETM has reflectivity $r_{\mathrm{ETM}} = 1$. The LIGO optics have non-zero transmission, which will be discussed in context of instrument commissioning in Chapter IV.

The fields within the cavity can be expressed as a system of equations:

$$\begin{aligned} E_A &= t_{\mathrm{ITM}} E_0 - r_{\mathrm{ITM}} E_B && (3.21) \\ E_B &= -e^{-2ikL} E_A && (3.22) \\ E_{ref} &= r_{\mathrm{ITM}} E_0 + t_{\mathrm{ITM}} E_B, && (3.23) \end{aligned}$$

which can be reduced to

$$E_A = \frac{t_{\mathrm{ITM}}}{1 - r_{\mathrm{ITM}} e^{-2ikL}} E_0. \tag{3.24}$$

Ignoring the effect of losses, the effective reflectance from the cavity is the ratio between the input and output fields,

$$r_{eff} = \frac{E_{ref}}{E_0} = r_{\mathrm{ITM}} - \frac{t_{\mathrm{ITM}}^2}{1 - r_{\mathrm{ITM}} e^{-2ikL}} = \frac{r_{\mathrm{ITM}} - e^{-2ikL}}{1 - r_{\mathrm{ITM}} e^{-2ikL}}. \tag{3.25}$$

On resonance,

$$e^{-2ikL_{res}} = 1 \tag{3.26}$$

and the effective reflectance is

$$r_{eff}(L_{res}) = \frac{r_{\mathrm{ITM}} - 1}{1 - r_{\mathrm{ITM}}} = -1, \tag{3.27}$$

corresponding to a phase shift of π in reflection. The Fabry-Perot cavity is senstive to small changes near resonance, which can be approximated as

$$
\begin{aligned}
r_{eff}(L_{res}+\Delta L) &\approx r_{eff}(L_{res}) + \left.\frac{dr_{eff}}{dL}\right|_{L=L_{res}} \Delta L &(3.28)\\
&= -1 + (-2ik\Delta L)\frac{t_{\mathrm{ITM}}^2}{(1-r_{\mathrm{ITM}})^2}. &(3.29)
\end{aligned}
$$

For a simple delay line, $t_{\mathrm{ITM}} = 1$ and $r_{\mathrm{ITM}} = 0$, the change in the phase shift of reflected light is $-2ik\Delta L$. The Fabry-Perot cavity enhances this change by a factor of the *cavity gain*,

$$
G = \frac{t_{\mathrm{ITM}}^2}{(1-r_{\mathrm{ITM}})^2}. \tag{3.30}
$$

The cavity gain can be physically interpreted as a consequence of the increased light storage time in the interferometer, equivalent to increasing the length of the arm cavity by a factor of the cavity gain. The Advanced LIGO input test masses have transmission $t_{\mathrm{ITM}}^2 = 1.4\%$, with a corresponding cavity gain of ~ 280 [8]. In this case, using a Fabry-Perot arm cavity enhances the sensitivity by more than two orders of magnitude. In the literature, the gain of a Fabry-Perot cavity is typically expressed as the ratio of the free spectral range, $f_{\mathrm{FSR}} = c/2L$, to the full width at half maximum of the cavity resonance, f_{FWHM}, or *finesse*:

$$
\mathcal{F} \equiv \frac{f_{\mathrm{FSR}}}{f_{\mathrm{FWHM}}} \approx \frac{\pi\sqrt{r_{\mathrm{ITM}}r_{\mathrm{ETM}}}}{1-r_{\mathrm{ITM}}r_{\mathrm{ETM}}}. \tag{3.31}
$$

Increasing the effective arm length indefinitely is undesirable because there is a lag in response of the cavity to a signal, equivalent to the storage time of light, $\tau_S \approx GL/2c$. The cavity acts as a low-pass filter with corner frequency at the *cavity pole* [139],

$$
f_{\mathrm{pole}} = \frac{1}{4\pi\tau_S} \tag{3.32}
$$

below which the amplitude of the cavity output falls off as f^{-1}. Increases in finesse also increase the displacement noise due to radiation pressure, which will be discussed further in section 3.2.3.

3.2.3.2 Dual recycling

Advanced LIGO is configured as a null instrument; the arms are aligned such that there is near-complete destructive interference at the output. Consequently, almost all of the input power is reflected towards the laser. Placing a power recycling mirror (PRM) between the laser and the beam splitter to form a resonant cavity between the PRM and the input test masses increases the effective power in the interferometer. For aLIGO, the power recycling cavity (PRC) increases the effective interferometer power by a factor of 50 [32].

The signal recycling cavity (SRC) is an unfortunate misnomer; in its standard configuration, aLIGO employs resonant sideband extraction. Both signal recycling and resonant sideband extraction require a partially-reflecting mirror at the output port. For resonant sideband extraction, the mirror is placed such that the carrier light is resonant in the SRC. When a gravitational wave interacts with the light in the interferometer, it induces frequency sidebands on the carrier light. In this case, the signal recycling mirror (SRM) forms a coupled cavity with the input mirrors, lowering the effective input test mass reflectivity for the gravitationally induced sidebands and decreasing their storage time [120]. In signal recycling, the mirror is placed such that the signal recycling cavity is resonant at $\nu_{\text{laser}} \pm \nu_{\text{signal}}$. This enhances the signal by the quality factor Q of the resonant cavity, at the cost of decreased sensitivity across the larger bandwidth [147]. This configuration may be pursued for future searches for continuous gravitational wave signals, particularly the low-mass X-ray binary Scorpius X-1 [165].

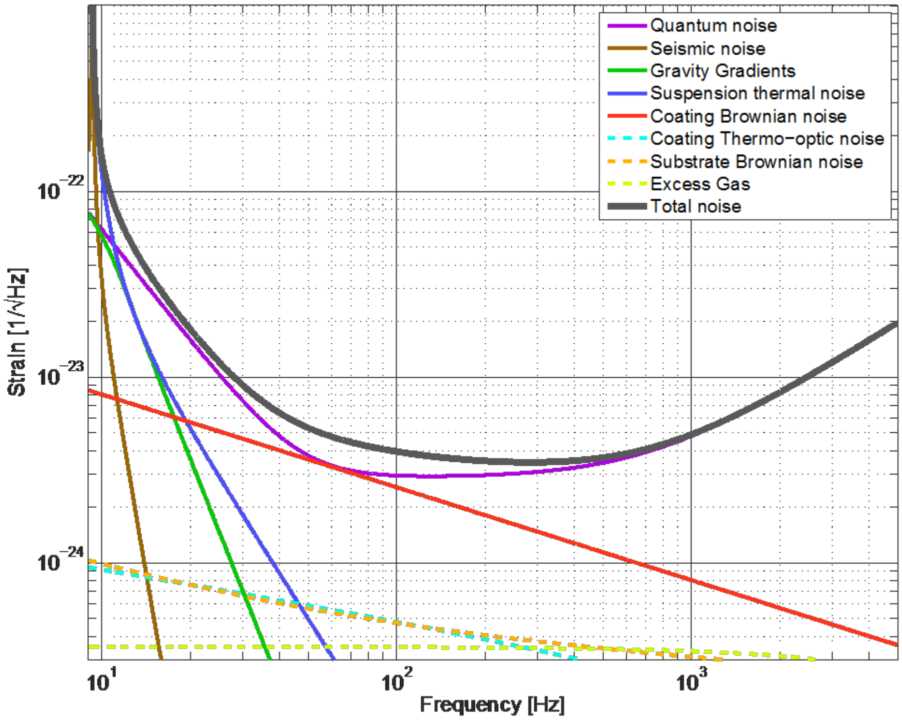

Figure 3.7: Advanced LIGO noise budget from the aLIGO Systems Description [25], showing the theoretical form of the dominant noise terms. Terms discussed in the text include the quantum noise (3.2.3), suspension thermal noise and coating Brownian noise (3.2.4), and seismic noise and gravity gradients (3.2.5).

3.2.4 The Standard Quantum Limit

As derived in equation 3.7, the output of a gravitational wave interferometer is a light power dependent on the path length difference between the two arms. Therefore, determining the possible precision on ΔL is equivalent to determining the measurable change in P_{out}. The fundamental limitation to measurement precision of power, and consequently ΔL, is the distinguishability of a change in power due to length change from a change in power due to quantum effects.

For the purpose of gravitational wave physics, a semiclassical approach is sufficient to describe the relevant quantum measurement effects. On a quantum level, the laser light arriving at a photodetector is made of individual photons, each with energy $E_\gamma = \hbar\omega_L$ with some mean number arriving per unit time, $\bar{N}$. This variation in power due to discrete photons arriving at random times is called *shot noise*. The probability distribution for discrete events characterized by some mean value $\bar{N}$ is the *Poisson distribution*,

$$p(N) = \frac{\bar{N}^N e^{-\bar{N}}}{N!}. \tag{3.33}$$

For large values of $\bar{N}$, the Poisson distribution can be approximated by a Gaussian distribution with mean $\bar{N}$ and standard deviation $\sqrt{\bar{N}}$. The relative fluctation in photon arrival rate will be the ratio of the standard deviation to the mean value,

$$\frac{\sigma_{\bar{N}}}{\bar{N}} = \frac{\sqrt{\bar{N}}}{\bar{N}} = \frac{1}{\sqrt{\bar{n}\tau}}, \tag{3.34}$$

with $\bar{N}$ recast as a rate per second, $\bar{n}$, over some measurement period τ. For the purpose of this derivation, assume the operating point of the interferometer is such that $P_{out} = P_{in}/2$, maximizing the response of power to length change, $dP_{out}/dL = 2\pi P_{in}/\lambda$. As the photon arrival rate per second is proportional to the power,

$$\bar{n} = \frac{P_{out}}{E_\gamma} = \frac{\lambda}{4\pi\hbar c} P_{in}, \tag{3.35}$$

it follows that the effect of shot noise decreases as laser power is increased. The corresponding noise in the strain signal is derived by dividing the fractional uncertainty in power due to statistical fluctuations by the fractional change in power due to length changes,

$$\sigma_{\delta L} = \frac{1/\sqrt{\bar{n}\tau}}{(dP_{out}/dL)/P_{out}} = \sqrt{\frac{\lambda\hbar c}{4\pi P_{in}\tau}}, \tag{3.36}$$

which is converted to strain noise by division by the interferometer arm length times the number of trips through the interferometer arms $\mathcal{N}$,

$$\sigma_h = \frac{1}{\mathcal{N}L}\sqrt{\frac{\lambda\hbar c}{4\pi P_{in}\tau}}, \tag{3.37}$$

which corresponds to a shot noise amplitude spectral density of

$$h_{shot}(f) = \frac{1}{\mathcal{N}L}\sqrt{\frac{\lambda\hbar c}{2\pi P_{in}}}. \tag{3.38}$$

Using realistic values of $\mathcal{N}L = 1000$ km, $\lambda = 1\ \mu$m, and $P_{in} = 1W$, the scale of shot noise amplitude spectral density is

$$h_{shot}(f) = 7 \times 10^{-23}\text{Hz}^{-1/2}\left(\frac{1000\text{km}}{\mathcal{N}L}\right)\sqrt{\frac{\lambda}{1\mu\text{m}}}\sqrt{\frac{1\text{W}}{P_{in}}}. \tag{3.39}$$

The fundamental limit of measurement precision is similar to the projected magnitude of gravitational wave strain. Improving shot noise is largely a function of increasing the effective power in the interferometer by using more powerful input lasers and the power recycling techniques discussed in the previous section. However, there is a conjugate noise source that limits the extent to which the power can be increased.

Light exerts radiation pressure force on the test masses,

$$F_{rp} = \frac{P}{c} \tag{3.40}$$

The fluctuation in photon number in the arms causes *radiation pressure noise* due to the motion of the test masses [147],

$$x(f) = \frac{1}{mf^2}\sqrt{\frac{\hbar P_{in}}{8\pi^3 c\lambda}}. \tag{3.41}$$

The power fluctations in the two arms will be anticorrelated; in the semiclassical picture, an increase of one photon in one arm requires a decrease of one photon in the other arm. Unlike the shot noise, the radiation pressure is increased by the folding of optical cavities; the light acts on each mass $\mathcal{N}$ times, rather than once, scaling up the radiation pressure noise by a factor of $\mathcal{N}^2$. The radiation pressure noise is thus

$$h_{rp}(f) = \frac{2\mathcal{N}^2}{\mathcal{N}L}x(f) = \frac{\mathcal{N}}{mf^2L}\sqrt{\frac{\hbar P_{in}}{2\pi^3 c\lambda}}. \tag{3.42}$$

Radiation pressure noise has the opposite scaling from shot noise, growing with power.

Shot noise and radiation pressure noise can be combined into a single *optical readout noise* term,

$$h_{\text{o.r.o.}} = \sqrt{h^2_{shot} + h^2_{rp}}. \tag{3.43}$$

The optimal input power to minimize optical readout noise is determined by setting $\frac{dh_{\text{o.r.o.}}}{dP_{\text{in}}}$ to zero. Equivalently, when the shot noise and the radiation pressure terms are equated, this optimal power is derived as a function of frequency f,

$$P_{opt}(f) = \frac{c\lambda m f^2}{2\mathcal{N}^2}. \tag{3.44}$$

This approach does not account for changes induced by the inclusion of the signal recycling mirror; in that case, the transmission of the signal recycling mirror becomes more important than the storage time of light in the cavities [8][49].

Advanced LIGO is designed as a quantum-limited instrument; at high frequencies, the limiting noise source is the quantum noise (the purple trace in Figure 3.7). To reach this level, the main laser power is increased from 10W to 180W, the quality of the arm and recycling cavities was improved, and the weight of the test masses was increased from 10 kg to 40 kg. Future upgrades plan to surpass the standard quantum limit through optical squeezing, which has been demonstrated on both the iLIGO [3] and GEO600 [14] detectors.

3.2.5 Thermal Noise

Another limit on detector sensitivity is the degree to which a test mass can remain at rest. Brownian motion in interferometer components causes small position fluctuations, and the effect of these fluctuations on measurements is the *thermal noise.*

The magnitude of thermal noise is characterized by the *fluctuation-dissipation theorem.* Introduced by Callen and Welton in 1951 [51], the fluctuation-dissipation theorem states that the power spectral density of fluctuations at equilibrium is proportional to the dissipative terms when the system is out of equilibrium. The magnitude of the thermal fluctuations is proportional to the temperature of the system and inversely proportional to the *quality factor* Q [158],

$$\langle x_{th}^2 \rangle \propto \frac{T}{Q}, \tag{3.45}$$

where Q is defined to be the ratio of the resonant frequency to the full width at half maximum of the resonance,

$$Q \equiv \frac{f_{res}}{f_{FWHM}}. \tag{3.46}$$

Formally, the power spectral density of thermal noise is given by

$$S_X(f) \approx \frac{k_B T}{2\pi^3 M} f_{res}^{-3} \begin{cases} \phi(f)(f_{res}/f) & f << f_{res} \\ Q/(1 + 4Q^2[(f/f_{res}) - 1]^2) & f \simeq f_{res} \\ \phi(f)(f_{res}/f)^5 & f >> f_{res} \end{cases} \tag{3.47}$$

where $\phi(f)$ is the loss angle, a measure of internal friction [56]. High-Q materials concentrate the thermal energy of vibrational modes near their resonance frequencies. Increasing Q and placing resonant frequencies outside of bands of interest reduces the impact of thermal noise on measurements.

For aLIGO, the dominant thermal noise terms come from the test mass coatings (the red trace in Figure 3.7) and the suspension fibers (the blue trace in Figure 3.7). Coating thermal noise was improved from iLIGO through developments in coating materials. Initial LIGO coatings were composed of alternating layers of SiO_2 (silica) and TaO_5 (tantala). Materials research showed that doping the tantala layers with 25% titanium dioxide reduced mechanical loss by 40% [82]. The suspensions were designed to reduce the impact of the suspension thermal noise by placing the stretch mode of the suspension fibers below the observation band at 9 Hz, and raising the violin mode to 510 Hz, above the most sensitive band of the interferometer [8]. Future improvements to gravitational wave interferometers will require additional advances in coatings research and the implementation of cryogenic cooling to reduce the effects of thermal noise well below the standard quantum limit [158].

3.2.6 Seismic Noise

Seismic noise is not a fundamental noise source; its characteristic scale is set by site-specific conditions rather than a physical constant such as k_B or $\hbar$. It is caused by continuous disturbances from wind and ocean waves and intermittent disturbances from earthquakes and human activity. A typical strain-equivalent power spectrum for seismic noise at the LIGO sites is [56]

$$S_{X,h}(f) \sim 10^{-12} \text{ m Hz}^{-1/2} \begin{cases} 1 & 1 \text{ Hz} \leq f \leq 10 \text{ Hz} \\ (10 \text{ Hz}/f)^2 & f > 10 \text{ Hz} \end{cases} . \tag{3.48}$$

At 100 Hz, the seismic noise has an equivalent strain of 10^{-14} m $\text{Hz}^{-1/2}$, seven orders of magnitude above the target strain sensitivity of 10^{-21}. Without extensive seismic isolation, gravitational wave interferometers are only expensive seismometers. Advanced LIGO uses both passive and active techniques to seismically isolate the interferometer components.

Each test mass is the bottom stage of a quadruple pendulum system. Pendula provide passive vibration isolation above their resonant frequency. Consider the equation of motion for a pendulum of length l with pivot point X,

$$l\frac{d^2x}{dt^2} = -g(x - X), \tag{3.49}$$

where g is the standard gravitational acceleration. The corresponding resonant frequency is $f_0 = (1/2\pi)\sqrt{g/l}$. Moving to the frequency domain, in the limit $f >> f_0$, the transfer function for the pendulum is

$$G_p(f) \approx \frac{f_0^2}{f^2}, \tag{3.50}$$

which is a low-pass filter for motion. For high frequencies, the transfer function for the quadruple pendulum is approximately the fourth power of the single-pendulum transfer function, f^{-8}. The coupled motions of the pendulums result in additional vibrational modes, which are damped using feedback control of the top mass.

The suspension is attached to the internal seismic isolation (ISI) system, a stack of three rigid plates separated by maraging steel cantilever blades [8]. The ISI is attached to the hydraulic external pre-isolator (HEPI), an active isolation system for frequencies from 0.1 - 10 Hz. HEPI controls six degrees of freedom using feedforward servos based on signals from geophones and inductive position sensors. This complex of seismic isolators causes the effect of seismic noise to be negligible above $\sim$ 11 Hz [8] (the brown trace in Figure 3.7).

A related noise source is gravity gradient noise (green curve in Figure 3.7), also known as *Newtonian noise*. This accounts for displacements in the position of the test masses due to the gravitational force between the test masses and changing densities in the surroundings. Although investigations have been undertaken to determine the Netwonian noise contributions from sources as exotic as the impact of tumbleweeds on the LIGO Hanford experiment hall [57], the most significant source of Newtonian noise is most likely to be changing densities in the ground underneath test masses due to seismic activity. Advanced LIGO is not expected to be limited by Newtonian noise, but further increases in sensitivity will require Newtonian noise isolation [117].

3.3 An Overview of Worldwide Gravitational Wave Research

Although this work focuses on aLIGO, it is only one of several interferometers under construction and operation around the world. The robust network of gravitational wave interferometers currently under construction will serve to verify signals, improve sky localization of detections, and explore a broad gravitational-wave frequency range.

3.3.1 Virgo

The Virgo interferometer, located in Cascina, Italy, is a French-Italian collaboration [20]. In its initial configuration, it was a power-recycled Fabry-Perot Michelson interferometer, similar to iLIGO. It had a slightly shorter arm length (3 km), slightly higher laser power (17 W), and a superior seismic isolation system. Aggressive seismic isolation improved its sensitivity at frequencies below 40 Hz, allowing searches for low frequency sources such as the Vela pulsar (PSR J0835-4510) [13].

Virgo is currently being upgraded to Advanced Virgo (AdV), an upgrade that is expected to increase its sensitivity by an order of magnitude [22]. AdV will be a dual-recycled Fabry-Perot Michelson interferometer with comparable sensitivity to aLIGO. Data-taking is expected to begin in 2016.

3.3.2 GEO 600

GEO 600 is a 600 m long interferometer located in Hanover, Germany [172]. To compensate for the smaller arm length, GEO 600 incorporated advanced technology in its initial configuration, including dual-recycling and multi-pendulum suspensions. GEO has served as a backup instrument, running in ”Astrowatch” mode to listen for nearby supernovae during the upgrade cycles of LIGO and Virgo. It also prototyped many advanced detector technologies, including improved lasers and optical squeezing [14]. Due to facility limitations, GEO 600 will not be able to achieve broadband sensitivities comparable to that of aLIGO or AdV. To compensate for this, GEO 600 has been moved towards a high-frequency focused configuration, GEO-HF [173]. GEO-HF will provide complementary observations for aLIGO and AdV at high frequencies, and is the only interferometer intending to use signal recyling to tune high frequency sensitivity.

3.3.3 KAGRA

The KAmiokande GRAvitational Wave Telescope (KAGRA) is currently under construction in Japan. This instrument is more ambitious than any other installation; the 3-km arms are housed in subterranean tunnels beneath Kamiokande mountain, and the test masses will be cryogenically cooled [98]. Building underground represses seismic noise due to surface waves and anthropogenic sources, and cryogenics reduce the effects of thermal noise. These technologies have been tested in the 100-m CLIO protototype, but have not been used in a kilometer-scale interferometer [127]. At design sensitivity, KAGRA will have comparable sensitivity to aLIGO and AdV. The 3-km arm tunnels have been drilled, and installation of internal components is in progress. A test run as a simple room-temperature Michelson interferometer is planned for late 2015, with runs in design configuration projected for 2018. [93].

3.3.4 Future interferometers

Next-generation interferometers are in the conceptualization and design phase. Further sensitivity improvements require a combination of reduction of quantum noise using squeezing, reduction of thermal noise through advanced materials and cryogenics, and interferometer baseline increase through new facilities [24]. The most complete conceptual design for a third-generation interferometer is the Einstein Telescope [18], a detector composed of three 10-km dual-recycled Fabry-Perot Michelson interferometers in a triangular configuration. The projected sensitivity for this instrument would be an order of magnitude better than aLIGO, opening up the possibility of measuring events at gigaparsec distances.

The LIGO collaboration is investigating a program of incremental upgrades to their current interferometer facilities. This would occur in two phases. The first step, A+, would require the addition of frequency-dependent squeezing, increase of mirror mass by a factor of 2, and the suppression of Newtonian noise. The next upgrade, Voyager, would achieve the best possible sensitivity at the current facilities. As proposed, Voyager would be fully cryogenic, with silicon mirrors, higher-power 1560-nm lasers, aggressive Newtonian noise suppression, and frequency-dependent squeezing [117].

Another proposal for improving the sensitivity of gravitational wave detectors is to scale up the current interferometer arm lengths by a factor of 10 [64]. Only modest improvements to current technologies are required to achieve a cosmological range ($z \simeq 1$) with a 40 km interferometer, reducing the research and design risk for future improvements to detectors.

Ground-based interferometers are limited to frequencies greater than ~ 1 Hz due to seismic and Newtonian noise. To probe gravitational waves at lower frequencies, interferometry must move into space. The Laser Interferometer Space Antenna (LISA) project was a joint mission of NASA and the European Space Agency (ESA), proposing to build a triangular interferometer with 6×10^6 km arms, trailing the Earth's orbit by 20 degrees. Due to budgetary concerns, NASA pulled out of the LISA project in 2010. ESA has approved a descoped version of LISA, evolved LISA (eLISA), an

L-shaped interferometer with 10^6 km arms, sensitive to frequencies between 0.001 and 0.1 Hz, with an intended launch date of 2034 [26]. In 2015, the LISA Pathfinder satellite was launched. LISA Pathfinder is the first test of LISA technology in space, and represents an important first step towards space-based interferometry [34].

A Japanese collaboration has proposed another space-based mission, the DECi-hertz Interferometer Gravitational Wave Observatory (DECIGO), to cover the frequency range between ground-based interferometers and eLISA, 0.1 - 10 Hz. The proposed form is a triangular set of differential Fabry-Perot interferometers with arm length 1000 km, with launch proposed for 2027 [94].

CHAPTER IV

Locking the Advanced LIGO Interferometer

4.1 Interferometer Sensing and Control

This chapter describes work done between June 2012 and March 2014 as part of the commissioning team for the Advanced LIGO ISC system, with a particular focus on the characterization and control of the Advanced LIGO arm cavities. As discussed in the previous chapter, the measurement of strain signals of order $h \sim 10^{-24}$ requires the use of multiple resonant optical cavities in a null-interferometer configuration. For successful operation, each of these cavities must be kept on resonance while simultaneously maintaining the null-output condition. The ISC subsystem manages the sensing and control of interferometer states, the process of achieving simultaneous multi-cavity resonance in the interferometer, and the maintenance of these resonances [149].

4.1.1 Control Theory

In the engineering discipline of control theory, three conditions are required to control a given *system*, defined as a group of elements connected by information links within some user-defined boundaries. A system consists of a definition of desired behavior, a method of generating actions on the system, and a method of making modifications to achieve the desired behavior, which is typically done in the form of a servomechanism, or servo [147]. Control theory is concerned with the topology of systems, the connections between elements in a system and the flow of information between them. This allows systems to be modeled using generic servo loops [100].

The aLIGO data acquisition system records over 300,000 control and status channels, corresponding to more than 257 degrees of freedom [149]. Consequently, aLIGO relies on principles of automatic control. Automatic control systems are based on control loops driven by error measurements with the goal of reducing error in the output. The majority of aLIGO systems operate in a feedback configuration, where the output of a system is compared to the desired output to produce an error signal.

The mathematical underpinnings of control theory are based on ordinary differential equations. Linearity is required to map a differential equation from time space into a complex frequency space $s = i2\pi f$ using Laplace transforms. So transformed, transfer functions can be convolved through direct multiplication [114]. On a practical level, linear systems have predictable, proportional responses to input. Although few systems are truly linear, the non-linear response curve of a system held near a chosen operating point can be approximated by the linear tangent to the curve at that point. The process of *locking* the interferometer brings the highly non-linear interferometer to a point where its response to input is linear.

A few basic concepts of linear control theory are useful for discussing the process of interferometer characterization and control. Consider the block diagram of a generic feedback servo in Figure 4.1. The controlled system, or *plant*, is represented by the transfer function $P(s)$. The generic gain block $G(s)$ is a convolution of all systems in the feedback path; for a real system, this would typically include transfer functions for sensors, filters, and actuators. The performance of a servo is characterized by its transfer function, which can be determined by solving the system of equations:

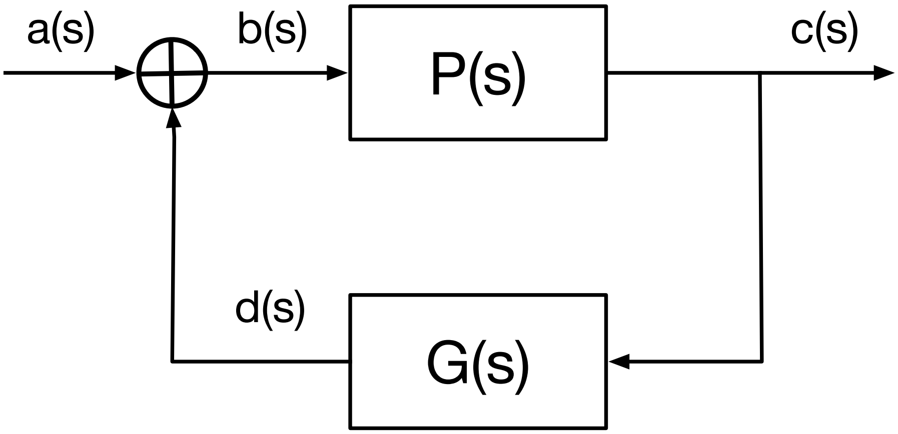

Figure 4.1: Topology of a generic feedback servo. The plant $P(s)$ is controlled by passing the output from the plant $c(s)$ through a gain $G(s)$ to produce an error signal $d(s)$. This error signal alters the input to the plant $b(s)$ to achieve the desired output $c(s)$.

$$\begin{aligned} b(s) &= a(s) \pm d(s) && (4.1) \\ c(s) &= P(s)b(s) && (4.2) \\ d(s) &= G(s)c(s) && (4.3) \end{aligned}$$

The transfer function from $a(s)$ to $c(s)$ is the *closed-loop transfer function*,

$$G_{CL} = \frac{PG}{1 \mp PG}. \tag{4.4}$$

As the closed-loop transfer gain is difficult to measure, servo transfer functions are typically characterized with the *open-loop gain*,

$$G_{OL} = PG. \tag{4.5}$$

Through factorization of the numerator and denominator, the closed-loop transfer function can be written in terms of a gain constant K, poles p_i, and zeroes z_j,

$$G_{CL} = K\frac{(s-z_1)(s-z_2)...(s-z_j)}{(s-p_1)(s-p_2)...(s-p_i)}. \tag{4.6}$$

The poles and zeroes determine the stability of the servo. A servo is asymptotically stable if and only if the impulse response goes to zero at infinity; if any pole has a positive real part, the component of the response at that frequency increases without bound, and the system is unstable. In practice, servos are designed such that there is a significant margin of stability. A typically sufficient criterion for servo instability is that at the *unity gain* point, the highest frequency where the open-loop gain magnitude equals 1, the phase of the transfer function response exceeds −180° [147]. For optimal stability, a phase margin of 40° from 180° is preferred for robustness against changes in systems.

4.1.2 Pound-Drever-Hall Locking

Pound-Drever-Hall (PDH) locking was developed by Drever and Hall in 1983 [62] as an optical analog to the Pound stabilizer used for microwave cavity stabilization [135]. The original purpose of PDH locking was to stabilize the frequency of a tunable laser by using a Fabry-Perot cavity as a frequency standard; a variation on the method is used to lock the aLIGO resonant cavities to the main laser.

A generic PDH servo is shown in Figure 4.2. Laser light of angular frequency ω is passed through an electro-optic modulator, which applies a phase modulation at sideband frequency Ω_m. This produces modulation sidebands on the light at harmonics of $\pm\Omega_m$, such that the electric field is described as a superposition of carrier and sideband, with implicit summation over the harmonics n,

$$E = E_0 i^n J_n(\beta) e^{i(\omega \pm n\Omega_m)}. \tag{4.7}$$

These sidebands are normally not resonant in the optical cavity and reflect nearly

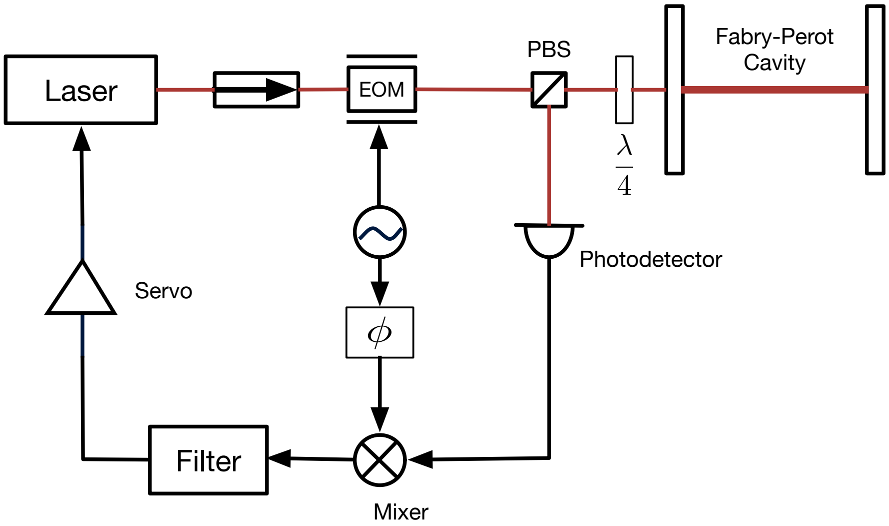

Figure 4.2: Example of locking a laser to a Fabry-Perot cavity using a Pound-Drever-Hall locking scheme. A laser of frequency Ω passes through an optical isolator to an electro-optic modulator (EOM), which applies modulation sidebands at frequency ω_m. The sidebands $\Omega \pm \omega_m$ reflect from the cavity. The beatnote between the sidebands and the reflected portion of the carrier Ω is measured at the photodetector and demodulated by mixing with the modulation frequency ω_m. This signal is low-pass filtered and used as the error signal to a servo, which changes the laser frequency to match the resonant frequency of the Fabry-Perot cavity.

completely, while the carrier resonates in the cavity with a fractional leakback given by the effective cavity reflectivity $F(\omega)$ is measured at the photodetector. The superposition of the electric fields due to carrier and sideband reflection is given by [41]

$$E_{\text{ref}} = E_0[F(\omega)J_0(\beta)e^{i\omega t} + F(\omega+\Omega_m)J_1(\beta)e^{i(\omega+\Omega_m)t} - F(\omega-\Omega_m)J_1(\beta)e^{i(\omega-\Omega)t}]. \tag{4.8}$$

The reflected field is measured at a photodetector as power $P_{\text{ref}} = |E_{\text{ref}}|^2$ [41],

$$\begin{aligned} P_{\text{ref}} =& P_c|F(\omega)|^2 + P_s\{|F(\omega+\Omega_m)|^2 + |F(\omega-\Omega_m)|^2\} \\ &+ 2\sqrt{P_cP_s}\{\Re[F(\omega)F^*(\omega+\Omega_m) - F^*(\omega)F(\omega-\Omega_m)]\cos\Omega_m t \\ &+ \Im[F(\omega)F^*(\omega+\Omega_m) - F^*(\omega)F(\omega-\Omega_m)]\sin\Omega_m t\} + (2\Omega_m \text{ terms}). \end{aligned} \tag{4.9}$$

The magnitude of the beat note between the carrier and the sideband is extracted by mixing the signal with a sine wave at the modulation frequency, $\sin\Omega_m t$. The resulting error signal is passed to a servo to adjust the laser frequency to match the resonant frequency of the cavity.

4.1.3 Resonances in Optical Cavities

Unlike the conceptual Fabry-Perot cavities discussed in Chapter III, the aLIGO arm cavities have curved mirrors. The fundamental mode of a resonant optical cavity with curved mirrors is a Gaussian beam [96]. For the purpose of this discussion, consider a laser beam of a single frequency ω propagating in the $\hat{z}$ direction. Under these conditions, the electric field can be expressed as the product of a polarized plane wave $e^{-ikz}e^{i\omega t}\hat{n}$ and a slowly varying distribution $A(r)$,

$$E(r, z, t) = A(r)e^{-ikz}e^{i\omega t}\hat{n} \tag{4.10}$$

where $r^2 = x^2 + y^2$, and $A(r)$ obeys the partial Helmholtz equation [145],

$$\frac{\partial^2 A}{\partial r^2} - 2ik\frac{\partial A}{\partial z} = 0. \tag{4.11}$$

The slowly varying distribution describes the macroscopic properties of the laser beam, including its spatial extent, phase propagation, and intensity distribution. One solution of the partial Helmholtz equation describes a Gaussian distribution,

$$A(r) = \exp\left[-i\left(P(z) + \frac{k}{2q(z)}r^2\right)\right], \tag{4.12}$$

where $P(z)$ describes a complex phase shift due to propagation, and $q(z)$ is a complex beam parameter describing the wavefront curvature and beam intensity. Resonant cavities also support higher order modes in the form of the polynomial Hermite-Gauss modes (Figure 4.3) and cylindrical Laguerre-Gauss modes (Figure 4.4).

The beam parameters for the (0,0) and higher order modes (Figure 4.5) are conventionally represented by transforming $q(z)$ into two real beam parameters $R(z)$ and $w(z)$,

$$\frac{1}{q(z)} = \frac{1}{R(z)} - i\frac{\lambda}{\pi w^2(z)}. \tag{4.13}$$

The physical interpretation of $w(z)$ is the size of the beam spot at a point z,

$$w^2(z) = w_0^2\left[1 + \left(\frac{\lambda z}{\pi w_0^2}\right)^2\right], \tag{4.14}$$

where $w_0 = w(0)$ is the minimum beam size or *beam waist*. The physical interpretation of $R(z)$ is the radius of curvature of the wavefront at z,

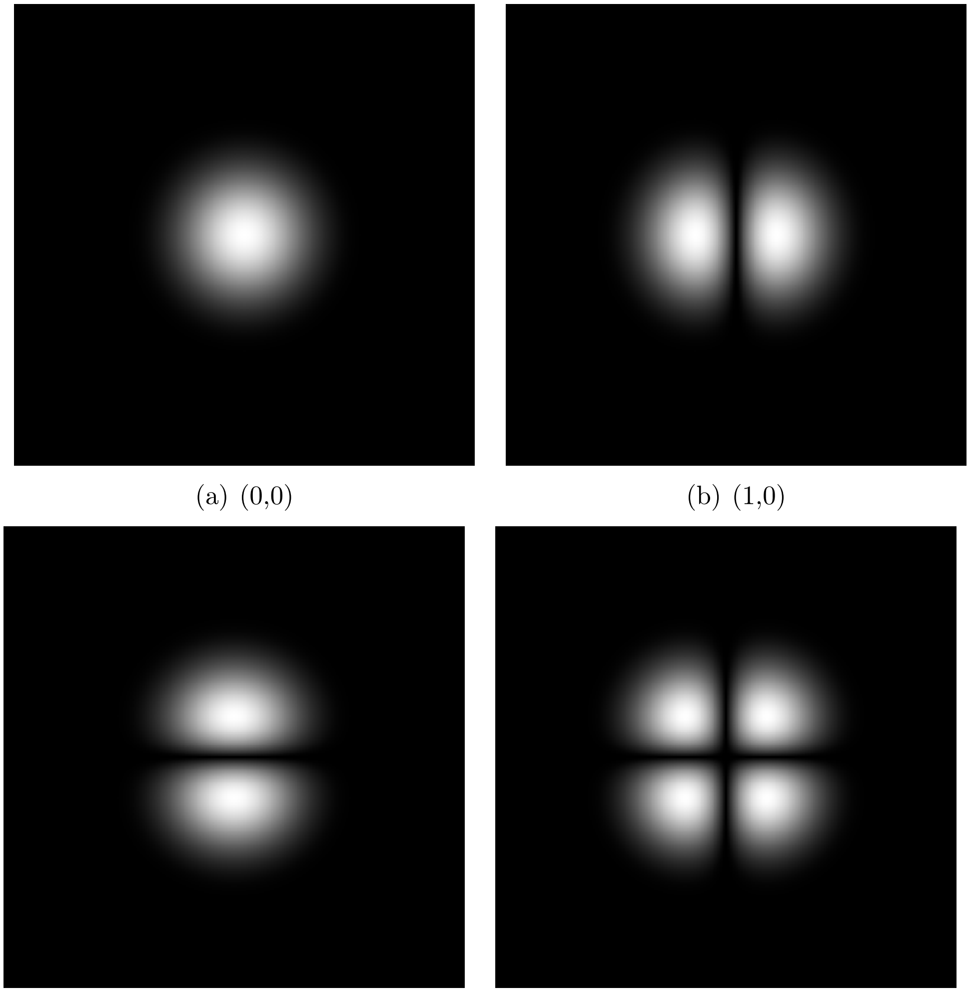

(a) (0,0) (b) (1,0)

(c) (0,1) (d) (1,1)

Figure 4.3: Intensity distributions of the lower-order Hermite-Gauss modes of an optical cavity.

$$R(z) = z\left[1 + \left(\frac{\pi w_0^2}{\lambda z}\right)^2\right]. \tag{4.15}$$

These can be simplified by defining the Rayleigh range z_R, the distance at which the cross-sectional area of the beam has doubled from its minimum at the waist,

$$z_R = \frac{\pi w_0^2}{\lambda}. \tag{4.16}$$

While these parameters are the same for Gaussian and for higher-order beams, the difference between the orders of beams appears in their phase shifts. The real

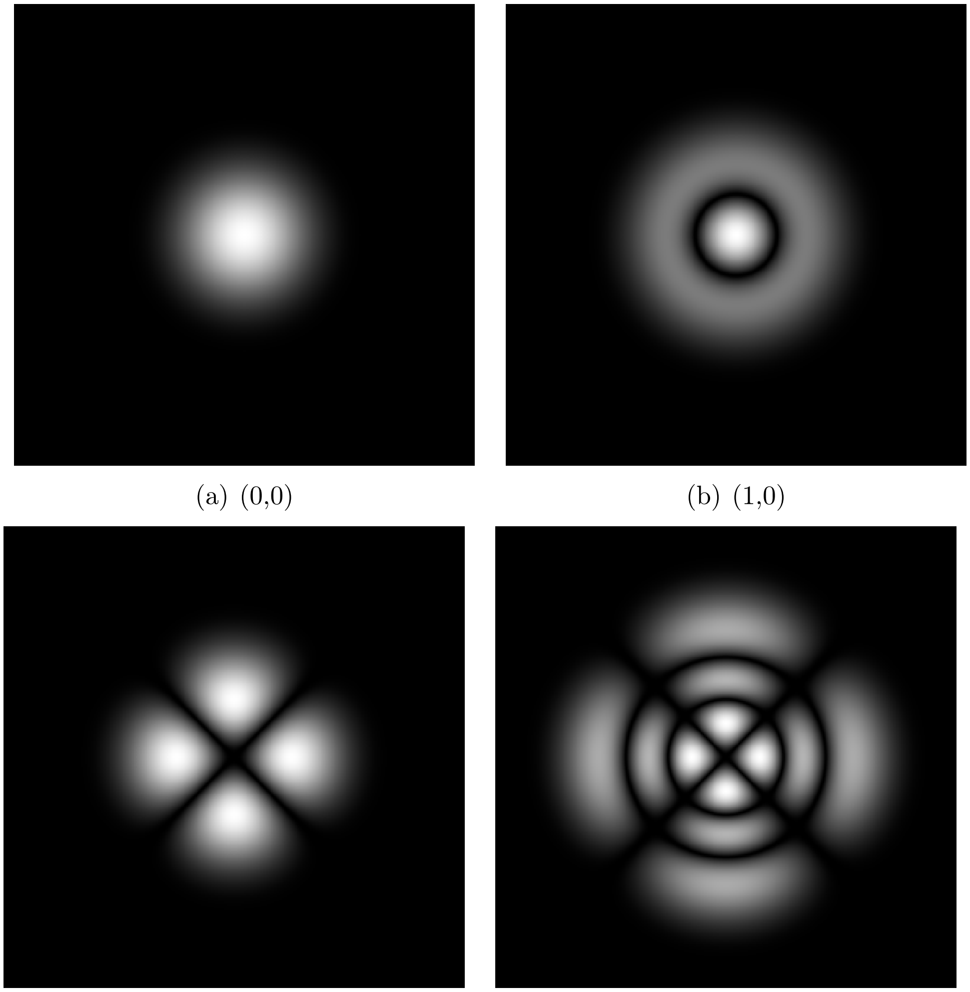

(a) (0,0) (b) (1,0)

(c) (0,2) (d) (2,2)

Figure 4.4: Intensity distribution of a selection of Laguerre-Gauss modes of an optical cavity.

part of the complex phase shift $P(z)$ can be reduced to a real phase shift $\zeta(z)$, called the *Gouy phase shift.* For a Hermite-Gauss beam of order (m, n), the Gouy phase is

$$\zeta_{mn}(z) = -(m+n+1)\arctan\left(\frac{\lambda z}{\pi w_0^2}\right), \tag{4.17}$$

while for a Laguerre-Gauss beam of order (p, l), the phase is

$$\zeta_{pl}(z) = -(2p+l+1)\arctan\left(\frac{\lambda z}{\pi w_0^2}\right). \tag{4.18}$$

Cavity characteristics are measured using observations of resonances in the cavity.

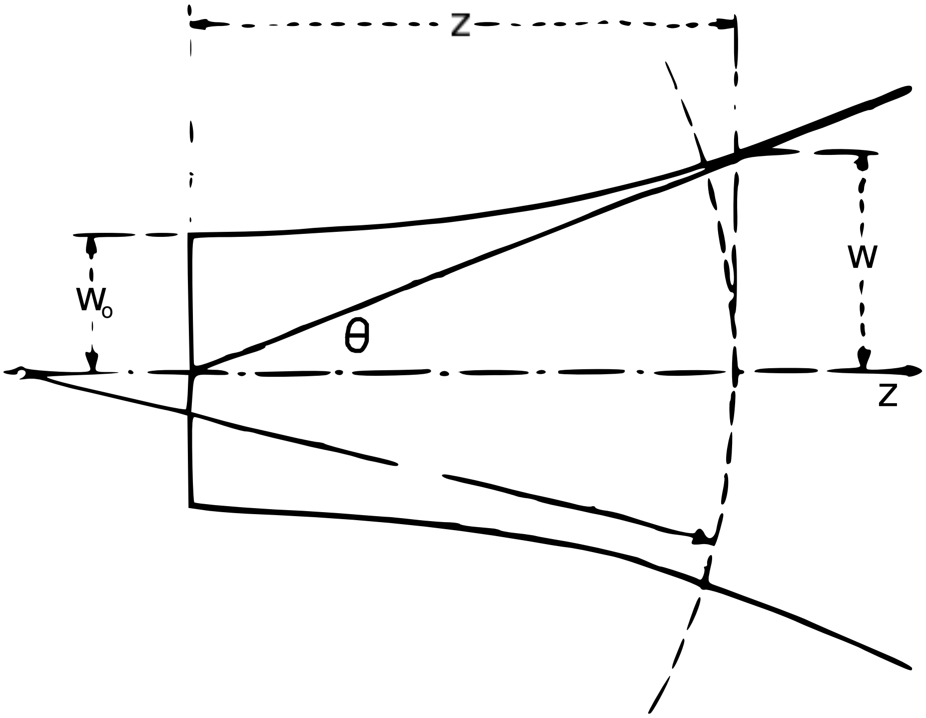

Figure 4.5: Parameters of a Gaussian beam. The beam waist w_0 is the point of smallest beam radius. The opening angle θ is the total angular spread of the beam.

Resonance occurs when the phase shift from one mirror to the other is a multiple of π [96],

$$kd - 2(m+n+1)\arctan\left(\frac{\lambda L}{2\pi w_0^2}\right) = \pi(j+1). \tag{4.19}$$

The first resonance of interest is the fundamental beat frequency, or free spectral range (FSR),

$$\nu_{\mathrm{FSR}} = \frac{c}{2L}. \tag{4.20}$$

Measuring the linewidth $\delta\nu$ of the primary resonance and dividing it by the FSR gives the finesse defined in Chapter III,

$$\mathcal{F} = \frac{\delta\nu}{\nu_{\mathrm{FSR}}}. \tag{4.21}$$

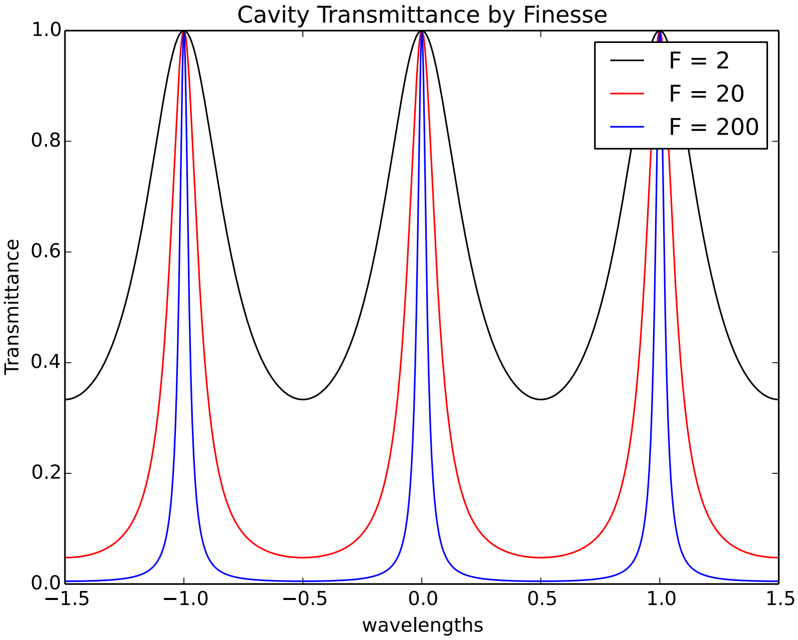

Figure 4.6: Effect of cavity finesse on linewidth. Higher finesse cavities have narrower linewidths, equivalent to higher Q resonance. Low finesse cavities are ineffective filters, allowing significant transmission even when the input signal is antiresonant.

The finesse is a measurement of the quality factor of the cavity resonance; as shown in Figure 4.6, the higher the finesse, the narrower the cavity resonance. Algebraic manipulation of the resonance condition gives the resonance frequency in terms of the FSR,

$$\frac{\nu}{\nu_{\mathrm{FSR}}} = (q+1) + \frac{1}{\pi}(m+n+1)\arccos\sqrt{g_1 g_2}, \tag{4.22}$$

where g_i is the *g-factor* for mirror i,

$$g_i = 1 - \frac{d}{R_i}, \tag{4.23}$$

a stability condition and proxy for the mirror radius of curvature R_i. For cavities with mirrors of unequal radius of curvature, such as the aLIGO arm cavities, the g-factor is typically expressed in terms of a weighted average of the g-factors for each mirror, the cavity G-factor G,

$$G = \sqrt{g_1 g_2} = \sqrt{\left(1 - \frac{d}{R_1}\right)\left(1 - \frac{d}{R_2}\right)}. \tag{4.24}$$

The absolute cavity length and mirror curvatures determine the free spectral range and the transverse mode spacing, and thus the cavity resonance characteristics.

4.2 Controlling the aLIGO Interferometer

4.2.1 Introduction

As discussed in Chapter 3, aLIGO is a dual-recycled Fabry-Perot Michelson interferometer. Interferometer operation requires simultaneous resonance in the arm cavities, power recycling cavity, and signal recycling cavity, while the internal Michelson is maintained at a dark fringe. The coupled resonant cavities of aLIGO have five degrees of freedom, as labeled in Figure 4.7 [123].

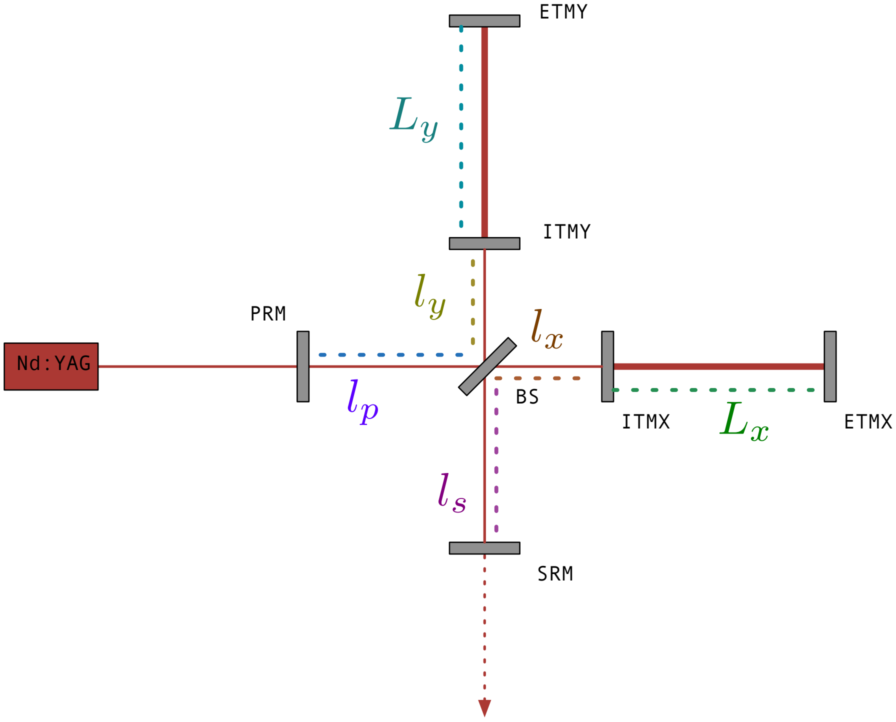

Figure 4.7: Advanced LIGO degrees of freedom. Advanced LIGO has five resonant cavities. The two arm cavities contribute degrees of freedom L_y and L_x, often reparameterized as L_{comm} and L_{diff}. The power recycling, signal recycling, and Michelson lengths contribute three more degrees of freedom, l_{PRC}, l_{SRC}, and l_{Mich}. These are collectively referred to as the corner degrees of freedom.

These are typically parameterized as the common and differential arm mode,

$$L_+ = \frac{L_x + L_y}{2} \tag{4.25}$$

$$L_- = L_x - L_y, \tag{4.26}$$

the power recycling cavity length,

$$l_{PRC} = l_p + \frac{l_x + l_y}{2}, \tag{4.27}$$

the signal reycling cavity length,

$$l_{SRC} = l_s + \frac{l_x + l_y}{2}, \tag{4.28}$$

and the Michelson length,

$$l_{Mich} = l_x - l_y. \tag{4.29}$$

The addition of the signal recycling cavity for aLIGO motivated the development of new control methods. During iLIGO, interferometer locking was achieved by locking the PRC and Michelson using the PDH method, then using a stochastic method to lock the arms. The arms were allowed to swing freely, and voice coils were used to stop the optics once resonance was observed [67]. This method of locking was unreliable and introduced additional noise into the system. Other modifications to the aLIGO arm cavities further reduce the potential effectiveness of this technique; the cavities have narrower linewidths, the test mass actuators are weaker, and the test masses are heavier [123]. An alternative variable-finesse locking method was devised for Virgo. In this method, the power recycling cavity was misaligned, preventing power buildup in the corner. The arms were locked using transmitted light at the ends of the arms, then the corner was brought into resonance [21]. This method relied on sending most of the power to the anti-symmetric port, with no clear extension to an interferometer with a signal recycling cavity.

In aLIGO, locking is achieved by decoupling the two arm cavity degrees of freedom from the three corner degrees of freedom by using two different wavelengths of light. During the commissioning process, these were similarly decoupled; the arm cavity control system was commissioned first at Hanford, while the corner control system was commissioned first at Livingston.

4.2.2 Arm Length Stabilization

The arm cavities are controlled by the Arm Length Stabilization (ALS) system (Figure 4.8), which decouples the arm cavities from the corner degrees of freedom by using an auxiliary laser injected into the cavity from behind the ETM. To prevent confounding signals from the main laser, this auxiliary laser is half the wavelength of the primary laser (532 nm). The auxilary laser is locked to the cavity with the PDH technique, and the frequency of the ALS laser is compared to twice the frequency of the main Pre-Stabilized Laser (PSL) to determine the offset of the PSL from resonance in the arms. These signals are used to actuate on the test masses to bring the cavity into resonance [123]. The ALS underwent three stages of integration testing at LIGO Hanford Observatory (LHO); One Arm Test (OAT) from June 2012 to September 2012 [157], Half Interferometer Test Y (HIFO-Y) from June 2013 to September 2013 [156], and Half Interferometer Test XY (HIFO-XY) from January 2014 to May 2014 [155].

The auxiliary laser is a dual-output frequency-doubled Nd:YAG, emitting at both the 1064-nm wavelength of the main laser and at the auxiliary 532-nm wavelength. The process of arm length stabilization begins by locking the green laser to the arm cavity. The 1064-nm output is compared to a signal from the PSL, sent through a

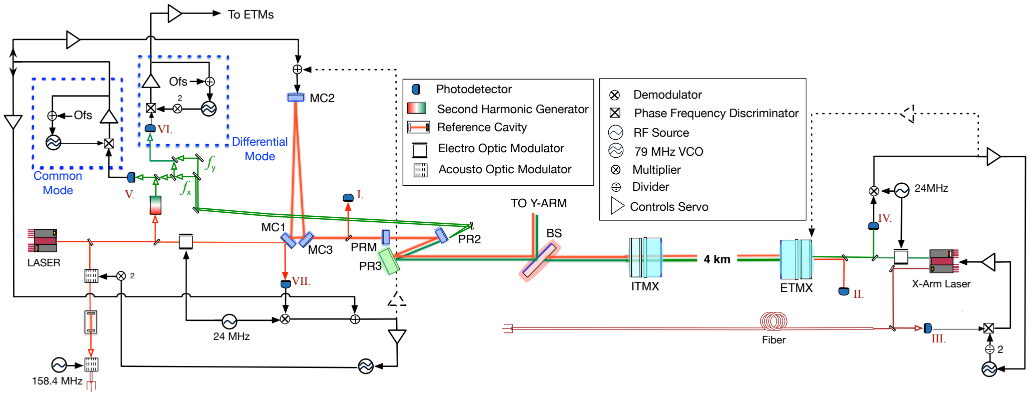

Figure 4.8: Advanced LIGO Arm Length Stabilization System. Only the X-arm is shown; the Y-arm is identical. The end station laser is a dual-frequency 532/1064-nm Nd:YAG laser. The 1064-nm beam is used to stabilize the auxiliary laser to a fiber-coupled beam from the main laser. The main laser in the corner station is stabilized to a reference cavity, then to the input mode cleaner cavity formed by optics MC1, MC2, and MC3. Interference between the transmitted light from the X-arm and a frequency-doubled pickoff from the main laser governs the common mode feedback path, while interference between the transmitted light from the X and Y arms governs the differential mode feedback path [159].

fiber to the end station. The resulting signal is used as the input to a phase-locked loop, which keeps the auxilary laser phase-locked to the main laser. The 532-nm output is used to sense and control the arm cavity length. Using the PDH method, the frequency of the 532-nm laser is changed such that the laser is resonant in the optical cavity.

The common and differential degrees of freedom, L_+ and L_-, are initially controlled using the 532-nm transmission through the arm cavities. First, the differential mode is controlled by comparing the transmitted signals from the X and Y arms, then feeding back to the test masses such that $L_- = 0$. Once this is achieved, the transmission from the X arm can be used as a proxy for the common arm mode L_+, and locked to a signal from the PSL sent through a second harmonic generator to control the offset of the PSL from the arm cavities.

4.2.3 Corner Locking

The ALS system also allows the arm cavities to be maintained at a fixed offset from resonance with the main laser, allowing the recycling cavities and Michelson to be locked independently. After the infrared resonance in the arms is found, the common frequency is offset by 500 Hz, then the corner is locked using a modified Pound-Drever-Hall method using both the first and third harmonic of the sidebands [30]. The corner locking method underwent two stages of integration testing at LIGO Livingston Observatory (LLO); the Input Mode Cleaner (IMC) test from August 2012 to February 2013 [72] and the Dual-Recycled Michelson Interferometer (DRMI) test from July 2013 to January 2014 [70].

The layout for the corner locking system is shown in Figure 4.9. The modulation sideband for the PDH control was chosen to be a multiple of the input mode cleaner free spectral range. As aLIGO requires the sensing and control of two corner resonant cavities, two modulation frequencies are used: one at 9 MHz for the power recycling cavity, and one at 45 MHz for the signal recycling cavity. The value of the SRC sideband was chosen to have sufficient separation from the third harmonic of the PRC modulation sideband at 27 MHz.

In iLIGO, the power recycling cavity was locked with the first harmonic of the modulation sideband. The normalized demodulated signals for this case are

$$\begin{aligned} V_1^{(I)} &= -J_0(m)J_1(m)g_0^2 r_{\text{rec1}}|r'_{\text{arm0}}|\delta L \\ &\quad -J_0(m)J_1(m)(g_0^2 r_{\text{rec1}} r_{\text{arm0}} + g_1^2 r_{\text{rec0}} r_{\text{arm0}} \cos\alpha)\delta l_+ \\ V_1^{(Q)} &= -J_0(m)J_1(m)g_1^2 r_{\text{rec0}} r_{\text{arm1}} \sin\alpha\delta l_-, \end{aligned} \tag{4.30}$$

where $V_1^{(I)}$ is in-phase with the initial modulation and $V_1^{(Q)}$ is in quadrature, 90° out of phase. The reflectivity of the modulation harmonic n from the arm or recycling

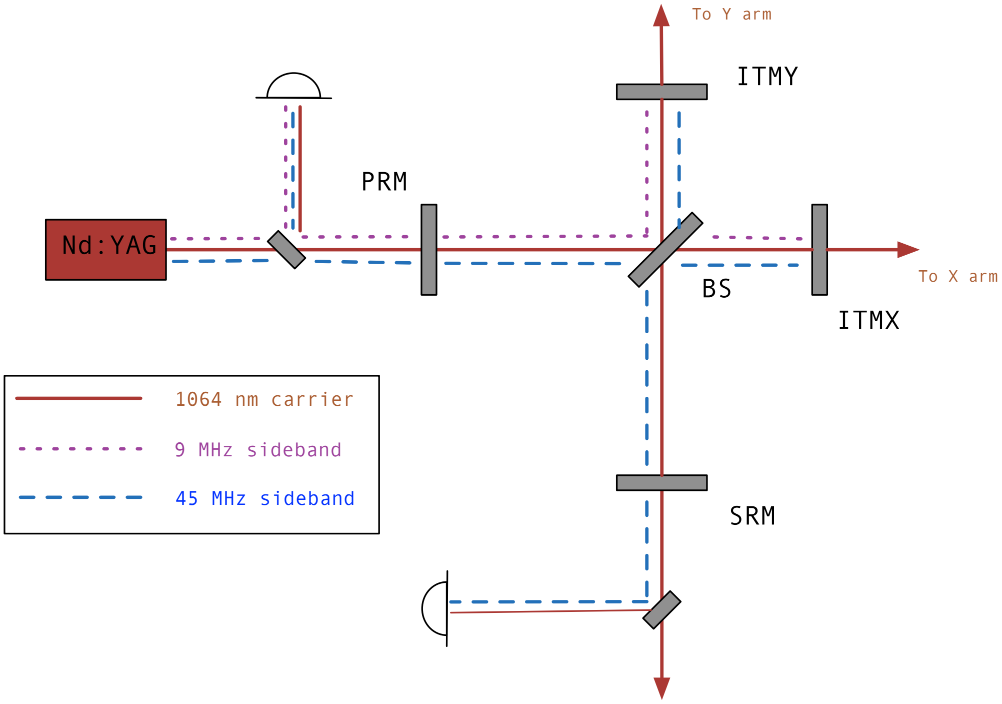

Figure 4.9: Schematic layout of Dual-recycled Michelson control signals. Two modulation sidebands are applied to the main laser. A-9 MHz sideband is used to sense and control the power recycling cavity, while a 45-MHz sideband is used for the signal recycling cavity. The cavities are locked such that the 9-MHz sideband is only resonant in the power recycling cavity, while the 45-MHz sideband is resonant in both the power and signal recycling cavities.

cavities is denoted by $r_{\mathrm{arm}n}$ or $r_{\mathrm{rec}n}$; $r'_{\mathrm{arm}0}$ is the derivative of the reflectivity of the carrier from the arms with respect to the round-trip phase in the arm ϕ [30]. These signals are sensitive to $\delta l+$, and $\delta l-$, and are effective control signals due to the relative strength of the first modulation sideband. There is, however, significant contamination of the common recycling cavity mode δl_+ signal by the common arm mode δL_+. Fluctuations in the arm cavity lengths can be enhanced by several hundred times, overwhelming the contribution of δl_+ to $V_1^{(I)}$ [30]. In addition, for a recycling cavity response that is equal for the carrier and first sideband, $r_{\mathrm{rec}0} = r_{\mathrm{rec}1}$, δl_+ vanishes, while for a carrier critically coupled to the recycling cavity, $r_{\mathrm{rec}0} = 0$, and δl_- vanishes. The solution, proposed by Arai et. al. [30] and implemented in aLIGO, is to use the third harmonic of the modulation frequency for lock acquisition, then use the stronger first harmonic signals for operational control. The process of using third harmonic modulation is referred to as 3F locking, while the first harmonic method is referred to as 1F locking.

The 3F signal is more complex than the 1F signal. The 1F signal is composed of the interaction between the carrier and the first harmonic of the modulation, while the 3F signal consists of the interaction between the carrier and the third modulation harmonic as well as the interaction between the first and second modulation harmonics. Although the amplitudes of these signals will be lower, they allow for a more complete and robust separation of variables. The in-phase and quadrature normalized demodulated signals for 3F locking are

$$\begin{aligned} V_3^{(I)} &= -J_0(m)J_3(m)g_0^2 r_{\text{rec}3}|r'_{\text{arm}0}|\delta L_+ \\ &\quad -J_1(m)J_2(m)g_1^2 r_{\text{rec}2}r_{\text{arm}1}\cos\alpha\delta l_+ \\ &\quad -J_0(m)J_3(m)(g_0^2 r_{\text{rec}3}r_{\text{arm}0} + g_3^2 r_{\text{rec}0}r_{\text{arm}3}\cos 3\alpha)\delta l_+ \\ V_3^{(Q)} &= -J_1(m)J_2(m)g_1^2 r_{\text{rec}2}r_{\text{arm}1}\sin\alpha\delta l_- \\ &\quad -J_0(m)J_3(m)g_3^2 r_{\text{rec}0}r_{\text{arm}3}\sin 3\alpha\delta l_-. \end{aligned} \tag{4.31}$$

Inspection of these equations shows a clear separation between δL_+ and δl_+; only the carrier $J_0(m)$ carries information about the arms, and the interaction between the first and second harmonic is not coupled to the arm motion. Additionally, there is no cavity geometry that results in a vanishing signal for either δl_+ or δl_-.

4.2.4 Performance

The full LIGO locking sequence shown in Figure 4.10 begins by misaligning the recycling cavities, then controlling the arms using the ALS system. First, the arms are locked to the laser in each end station. After the arms are locked to the auxiliary laser, the transmission from the cavities is combined at the corner station for control of the differential and common arm cavity modes. Then, the cavities are scanned for the resonance of infrared light. Once found, they are moved 500 Hz off resonance. Then, the recycling cavities are aligned from their initial misaligned state. The dual-recycled Michelson interferometer is locked using 1F signals, then moved to 3F signals for control during the process of bringing the arm cavities to resonance. Although the ALS was designed to control this process throughout, high transmissivity of the test mass coatings (discussed further in section 4.5) motivated a move to controlling the differential mode using arm cavity infrared transmission and the common mode using infrared reflection from the cavities. Once power is built up in the arm cavities,

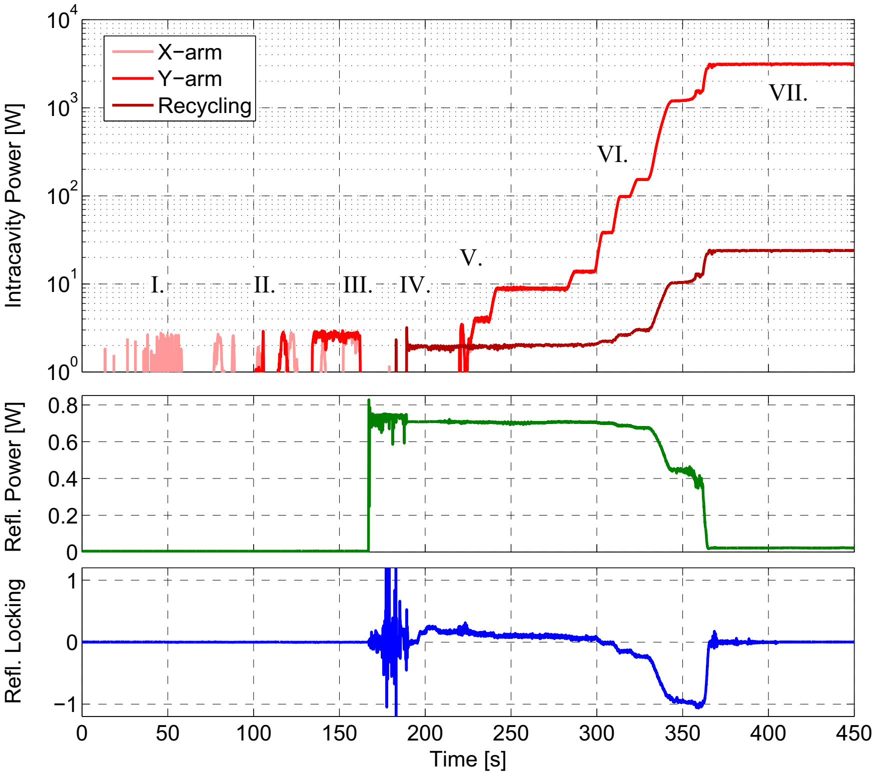

Figure 4.10: Advanced LIGO locking sequence. During phase I, the arm cavities are locked using the ALS auxiliary lasers in each end station, then switched over to control by the common and differential signals at the corner station. During phase II, the arm cavity common mode is scanned to find the infrared resonance. In phase III, the arm cavities are moved to 500 Hz from resonance and the recycling cavities are aligned. In phase IV, the dual-recycled Michelson is locked using 1F locking then immediately switched to 3F locking signals. In phase V, the arm cavity power buildup is sufficient for the differential arm control to be switched to IR transmission, and in phase VI, buildup is sufficient to control the common arm mode with IR reflection signals. In phase VII, the interferometer is switched to 1F locking, and the interferometer is in full lock [123].

the interferometer is switched from 3F to 1F signals for data taking.

The fully controlled locking method developed for aLIGO requires less than ten minutes to reach full lock from an unlocked state. This locking process is reliable, robust, and repeatable, and shows the value of multi-color interferometry for control of gravitational-wave interferometers. The two-hour lock stretch required for acceptance was achieved at Livingston on June 30, 2014 and at Hanford on February 6, 2015 [69][71].

4.3 Arm Cavity Characterization with Auxiliary Lasers

4.3.1 Introduction

An additional benefit to the auxiliary ALS laser is the potential for use as a measurement and diagnostic tool [123]. As part of the OAT, the ALS system was used to make measurements of the aLIGO arm cavity by observations of resonant cavity response.

The defining properties of a Fabry-Perot cavity are the absolute cavity length and the curvature of the mirrors. These uniquely determine the free spectral range (equation 4.20) and the modal spacing, or difference between the fundamental resonance frequency and the frequencies of higher-order cavity modes (equations 4.17 and 4.18).

The characterization of cavity properties is essential to the operation of gravitational-wave detectors. Controlling the five core interferometer degrees of freedom requires PDH modulation sidebands to be resonant in the corner cavities and antiresonant from the arm cavities. Therefore, matching the RF modulation frequency to the cavity lengths is an essential part of the control systems. In addition, mismatches in arm cavity lengths cause degradation of sensitivity due to cross-coupling of noise in the interferometer. Characterization methods also quantify changes in cavity characteristics over time, including drifts in mirror position due to ground motion and changes in mirror curvature due to thermal effects. Understanding changes in the cavity allows for optimal control of the system and improvement of noise characteristics.

Many methods have been used for measurement of cavity characteristics, with varying degrees of precision. Rakhmanov et. al. [141] used an optical vernier method to measure the length of the iLIGO arm cavity. This method exploited the phase modulation sidebands applied to the main laser for interferometer control. Typically, the phase modulation sidebands do not resonate in the arm cavities. By dithering the test mass mirror, the main laser and its sidebands were brought into resonance. Measurements obtained using this method were accurate to a precision of 4 mm, approximately one part in 10^6. However, this method is only useful for measuring the length of the arm cavity, and has no extension to allow for measurements of cavity g-factor.

Later, Rakhmanov et. al. [140] varied the laser RF modulation to measure the resonances of the dynamic interactions between the carrier and modulation frequencies. This method allowed for measurement of the cavity length to within 80 μm, one part in 10^8. It was recognized that this variation of the laser frequency allowed for measurement of the cavity g-factor through the dynamic resonances of TEM01 modes in the cavity, but no attempt was made to report the cavity g-factor. The IMC is designed to remove higher-order modes from the main laser beam, and allows for the injection of frequency signals only at multiples of its free spectral range; consequently, injections of arbitrary frequencies are not possible on the main laser.

Stochino et. al. [161] developed a method for measurement of the properties of a resonant cavity using two laser beams. The primary laser beam is locked to the cavity in the TEM00 mode. A secondary laser is phase-locked to the primary laser, then locked to the cavity. The frequency of the secondary laser is modulated with a local oscillator to establish resonances in higher-order modes of the cavity, and the beat note between the two beams is measured to determine the cavity resonances. At the 40m interferometer prototype, this method was used to measure the length of the cavity to a precision of 6 μm for the X-arm, and 30 μm for the Y-arm, approximately one part in 10^6-10^7, and the cavity g-factors for both arms to approximately one part in 10^5. This method is precise but requires the addition of dedicated measurement systems.

The unique geometry of the ALS system, as shown in Figure 4.11, allows for the measurement of cavity characteristics with no additional optical components. The ALS system is designed to be locked directly to the arm cavities. As the system is not intended for use during operation, the removal of higher order modes from the beam is not necessary, so there is no mode cleaner preventing the injection of arbitrary frequencies into the cavity. Using the ALS for cavity characterization can provide the depth of information of the Stochino method with the low experimental overhead of the Rakhmanov method, resulting in a method for accurate measurements of the characteristics of kilometer-scale Fabry-Perot cavities.

4.3.2 Method

The ALS method was implemented during the OAT integration test at LHO, from June 21, 2012 to September 16, 2012. The goal of OAT was to use the Y-arm cavity to demonstrate the effectiveness and quantify the performance of the ALS and investigate the low-frequency (< 1 Hz) performance of the seismic and suspensions systems, while aLIGO installation proceeded in the rest of the interferometer. The OAT cavity varied from the specifications set out for aLIGO core optics; its test masses were made from ETM blanks with ITM coatings [91]. These blanks were made of Corning 7980 fused silica, which was found to have poor stability at the temperatures required for coating application [33][38][39]. These blanks were subsequently used as test surfaces for coatings [38] and absorption measurements [40]. Because of the variance from aLIGO design parameters, the OAT cavity finesse for 532-nm light was

Configuration	ROC (m)	T_{ITM}	T_{ETM}
OAT	2307 (ITM) 2313 (ETM)	1.38%	1.03%
Nominal	1934(-5 +15) (ITM) 2245(-5 +15) (ETM)	0.5%-2%	1%-4%

Table 4.1: Radii of curvature and 532-nm transmissions for aLIGO optics, comparing design specifications to OAT cavity values [81][59][91][73].

~ 300, greater than the aLIGO design value of ~ 100.

The design of the ALS controls system allows cavity response measurements to be made using a commercial signal analyzer. The phase-locked loop (PLL) and PDH servos are both built on the Common Mode Servo platform, a two-input analog servo board with a fast output used for analog servo control loops and a slow output used for digital controls and readbacks [152]. This generic servo platform is used for laser and cavity locking throughout the aLIGO ISC system, and includes modifiable filter banks that are tuned to the needs of each control loop through modification of the analog filter components [151]. The design incorporates two excitation points for measurement of loop transfer functions a common excitation that acts on both the fast and slow paths, and a single-path excitation that can be used to apply excitations to either the fast or the slow path [150][68]. The integrated single-path injection port on the fast path of the PLL servo was used to apply a phase modulation to the ALS laser output.

The ALS laser is an Innolight Prometheus dual-frequency 532/1064-nm NPRO. A phase modulation applied to the laser through the PLL servo is applied to both the 532-nm and 1064-nm lasers, as shown in Figure 4.11. In typical operation, the 1064-nm laser is used to lock the ALS laser to a signal from the PSL, transmitted through a fiber to the end station. The 1064-nm beam does not interact with the cavity, and the demodulated RF photodiode signal (A) can be taken as a proxy for the signal injected into the arm cavity. The 532-nm beam is injected into the cavity. The cavity reflection is collected on a photodiode for use in the PDH servo, and the demodulated

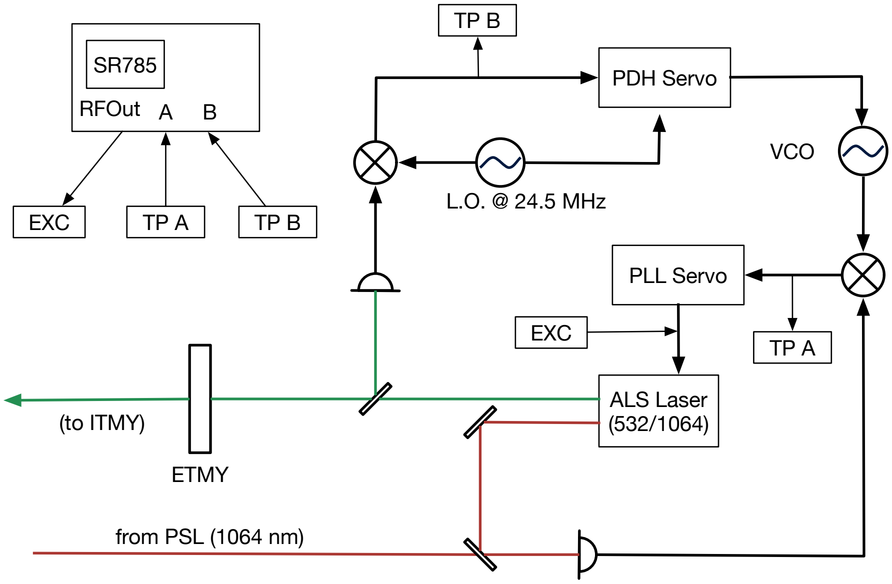

Figure 4.11: Schematic depiction of the cavity scan method. As part of the ALS system, the 532-nm output of a dual-wavelength 532/1064-nm auxiliary laser is locked to the aLIGO arm cavity, while the 1064-nm output is used to phase-lock the auxilary laser to the main laser. An excitation applied to the laser (EXC) will phase-modulate both outputs at the same frequency. The measured frequency response at TP A is a proxy for the input to the cavity, and the response at TP B is a proxy for the cavity response. The transfer function given by the ratio $\frac{B}{A}$ is used to measure cavity resonant frequencies in the cavity scan method.

input to the PDH servo (B) is the cavity response. For the cavity scan measurements, a Stanford Research Systems SR785 was used to take transfer functions in a swept-sine configuration. Measurements were automated using a Prologix GPIB-Ethernet controller to connect the SR785 to the site network.

The cavity response measurement is perfomed by injecting a frequency modulation into the PLL servo and measuring the transfer function between B and A,

$$H_{cavity}(s) = \frac{B(s)}{A(s)}. \tag{4.32}$$

At resonant frequencies, the reflection from the cavity will decrease, forming a dip in the transfer function. The primary resonance expected is the free spectral range frequency. A perfectly aligned Fabry-Perot cavity resonates in the TEM00 mode and only admits light with frequencies

$$\nu = N \times \nu_{FSR}. \tag{4.33}$$

Other resonances of interest include higher-order modes and dynamical resonances. In an imperfectly aligned system, a superposition of TEM modes is admitted, allowing resonances of the higher-order modes as stated in equation 4.22. Dynamic resonances between the PDH modulation sidebands and the free spectral range frequency are also expected [140]. Given a known PDH modulation frequency ν_{PDH}, a dynamical resonance ν_{res} will occur at a frequency such that

$$\nu_{\text{PDH}} = (N-1)\nu_{\text{FSR}} + \nu_{\text{res}}. \tag{4.34}$$

The cavity properties are determined from these resonance measurements. The primary TEM00 resonance is located at the free spectral range, and the ratio between the full width at half maximum (FWHM) of the resonance peak and the value of the FSR gives the cavity finesse, as defined in equation 4.21. The higher-order mode resonances determine the transverse mode spacing, which is used to derive the cavity G-factor given in equation 4.24. To derive this, let $q = 0$, and set $m + n$ equal to a mode number count variable, j. The modal spacing is the difference between two adjacent modes ν_j and ν_{j+1},

$$\Delta\nu_j = \nu_{j+1} - \nu_j = \nu_{\text{FSR}} \frac{\cos^{-1} G}{\pi}. \tag{4.35}$$

A simple rearrangment gives the cavity G-factor in terms of the modal spacing,

$$G = \cos\left(\pi \frac{\Delta\nu_j}{\nu_{\text{FSR}}}\right). \tag{4.36}$$

Measurement	Nominal Value	Measured Value
Length	3994.5 m	3995.7 ± 0.6 m (FSR) 3995.987 ± 0.0009 m(PDH)
Free Spectral Range	37.5256 kHz	37514 ± 6 Hz (direct) 37511.69 ± 0.008 Hz (PDH)
Finesse	260	375 ± 50
Modal Spacing	9.002 kHz	8.881 ± 0.001 kHz
Cavity G-factor	0.7292	0.736 ± 0.003

Table 4.2: Predicted and measured values for cavity scan quantities of interest.

4.3.3 Results

The SR785 signal analyzer has a maximum frequency of 100kHz. To measure the free spectral range peaks, a transfer function was taken from 35 kHz to 80 kHz. Signal analyzer power of 10 mV was used for these injections, corresponding to a modulation depth of 0.1. Sharp resonance peaks were observed at 37523 ± 3 Hz and 75028 ± 3 Hz, as shown in Figure 4.12, with full width at half maximum of 100 ± 10 Hz, corresponding to a cavity finesse of ∼ 375 ± 50 . For each of the resonance peaks, the data was fitted to a Lorentzian (Figure 4.13) of the form

$$G(f) = \frac{A}{(f-B)^2 + C} + D. \tag{4.37}$$

The position of the resonance peak was determined from the value of the parameter B, with the error on the location determined from the variance of parameter B. Taking the mean of the FSR from the first and second resonance results gives FSR value of 37514 ± 6 Hz, corresponding to a cavity length of

$$L_{\text{cavity}} = \frac{c}{2\nu_{\text{FSR}}} = 3995.7 \pm 0.6 \text{ m}. \tag{4.38}$$

As discussed in the previous section, the FSR measurement can be refined by measurement of the dynamic resonances with the PDH modulation sidebands. To determine which resonant features were due to the resonant sidebands, the PDH

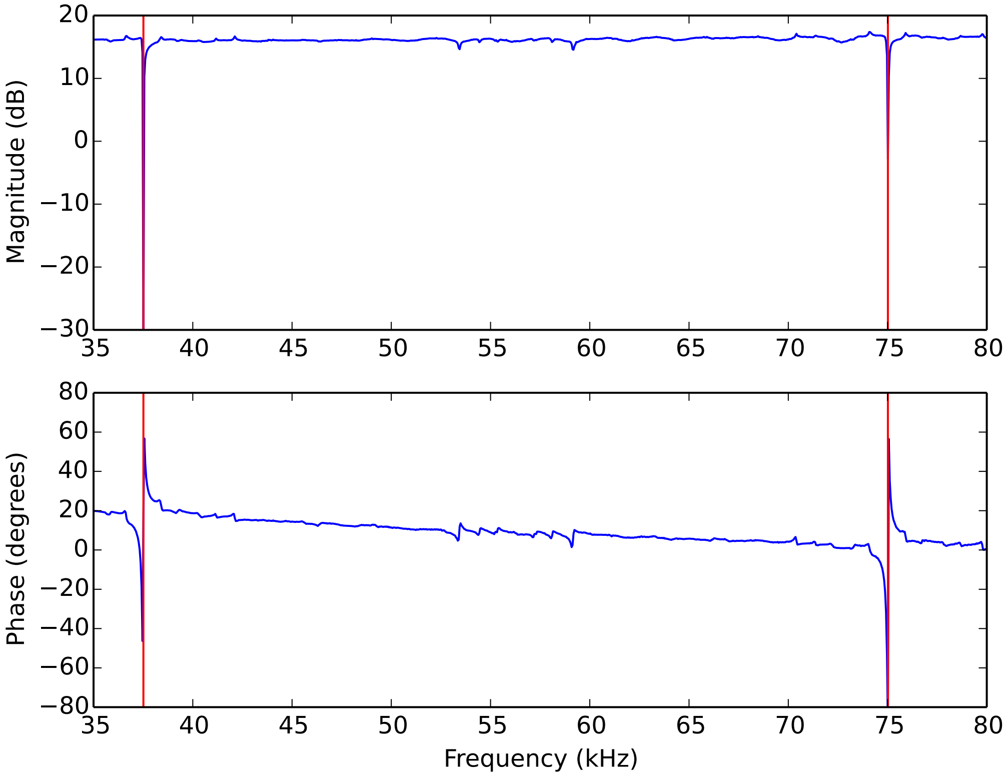

Figure 4.12: Direct measurement of cavity free spectral range. The measurement was performed using an SR785 signal analyzer in swept-sine configuration, with frequencies from 33 kHz to 80 kHz. The supplied power from the signal analyzer was 5 mV, corresponding to a modulation depth of 0.07. The transfer function output is shown as a blue trace, and the dips corresponding to the free spectral ranges are denoted with vertical red lines. The free spectral range resonances were measured at 37523 ± 3 Hz and 75028 ± 3 Hz, with a resonance full width at half maximum of 100 Hz.

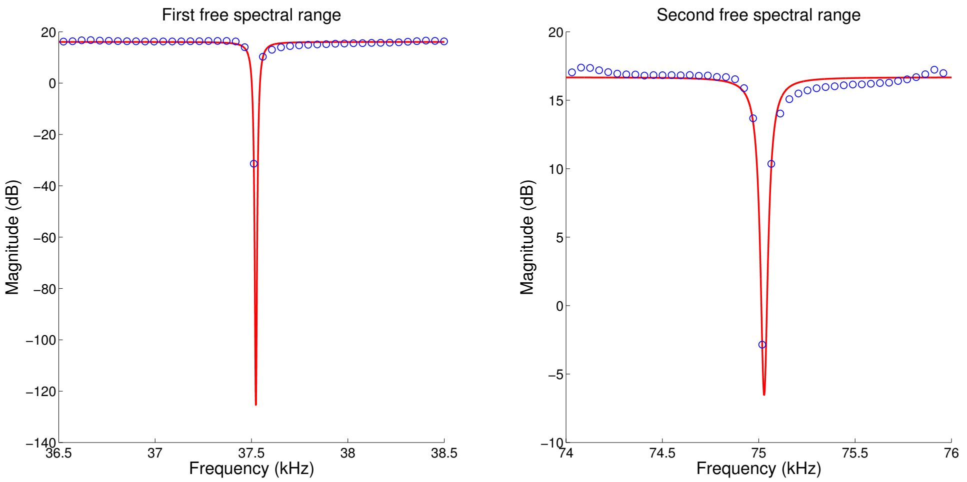

Figure 4.13: Demonstration of Lorentzian fit to free spectral range resonance peaks, used to determine the free spectral range resonant frequencies of 37523 ± 3 Hz and 75028 ± 3 Hz. The transfer function data is shown as blue circles, while the resulting fit is shown as a red line.

modulation frequency was increased 200 Hz for the measurement shown in Figure 4.14, from 24.515730 MHz to 24.515930 MHz. Using the expression given in equation 4.34 and using the cleanest resonant peak, $\nu_{res} = 58313 \pm 5$ Hz, the integer N is

$$N = \frac{\nu_{\text{PDH}} - \nu_{res}}{\nu_0} + 1 = \frac{24515930 - (58313 \pm 5)}{37514 \pm 6} + 1 \simeq 653. \tag{4.39}$$

Returning to equation 4.34, the FSR can be determined with greater precision,

$$\nu_0 = \frac{\nu_{\text{PDH}} - \nu_{res}}{N - 1} = \frac{24515930 - (58313 \pm 5)}{652} = 37511.69 \pm 0.008 \text{ Hz} \tag{4.40}$$

giving a cavity length with parts per million precision,

$$L_{\text{cavity}} = 3995.987 \pm 0.0009 \text{ m}. \tag{4.41}$$

To measure the frequency of higher-order modes, the cavity was deliberately mis-

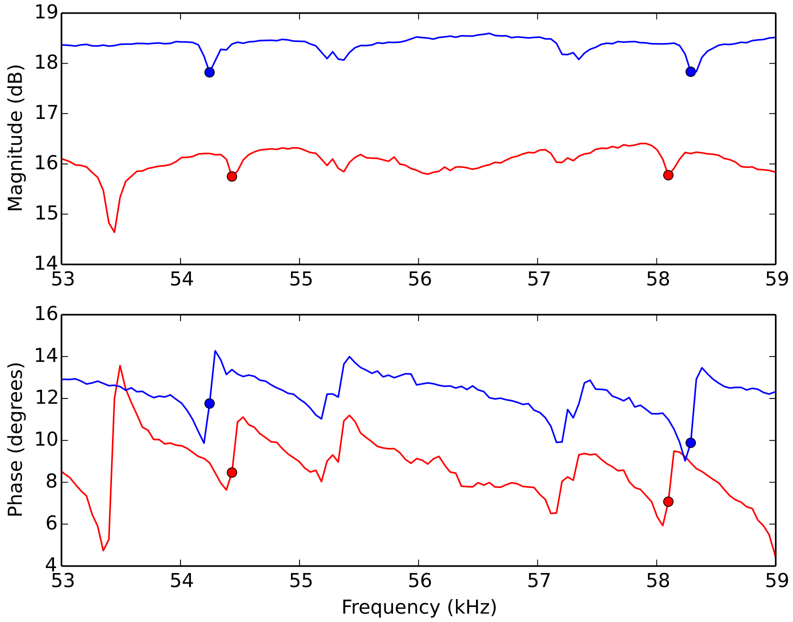

Figure 4.14: Determination of dynamic PDH resonance frequency. Two cavity transfer function measurements were performed using an SR785 signal analyzer in swept-sine configuration, with frequencies from 33 kHz to 80 kHz. The supplied power from the signal analyzer was 5 mV, corresponding to a modulation depth of 0.07. Between the two measurements, the RF reference frequency was increased by 200 Hz, from 24.515730 MHz to 24.515930 MHz. The dynamic resonance between the modulation frequency and the cavity free spectral range shifted between the cavity transfer function taken before the modulation frequency shift (blue trace) and the cavity transfer function taken after the modulation frequency shift (red trace). This 200 Hz shift was used to determine that the modulation peak on the left is a sideband of the second FSR at 75.028 kHz, while the sideband on the right is a sideband of the first FSR at 37.511 kHz.

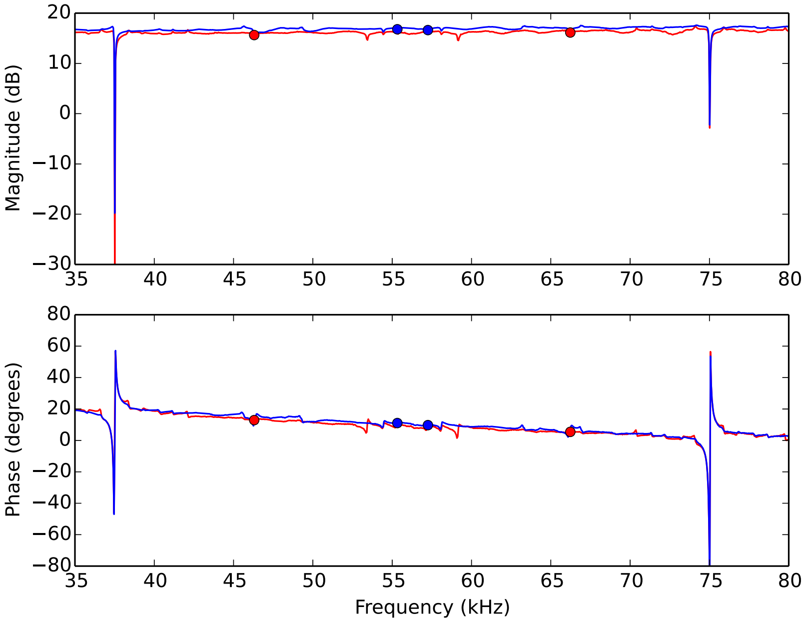

Figure 4.15: Determination of modal spacing. Two cavity transfer function measurements were performed using an SR785 signal analyzer in swept-sine configuration, with frequencies from 33 kHz to 80 kHz. The supplied power from the signal analyzer was 5 mV, corresponding to a modulation depth of 0.07. Between the first measurement (blue trace) and second measurement (red trace), the cavity was deliberately misaligned to allow better coupling of higher order modes to the cavity. The red dots correspond to the Hermite-Gauss (1,0)/(0,1) modes, while the blue dots correspond to the Laguerre-Gauss (1,0) modes; they were distinguished via estimations of cavity modal spacing from pre-installation mirror curvature measurements and observations of pitch and yaw dependence of resonance strength.

aligned to increase the coupling of higher-order modes. One measurement of the higher-order modes is shown in Figure 4.15 The primary higher-order mode resonances that appeared were the Hermite-Gauss (0,1) modes and the Laguerre-Gauss (1,0) modes, at frequencies given in table 4.3.

Using equation 4.36, the cavity G-factor is found to be

$$G = 0.736 \pm 0.003. \tag{4.42}$$

Mode	Frequency (Hz)	Spacing (Hz)
HG10	46377.9 ± 0.4	8866.3 ± 0.4
LG10	55331 ± 1.0	8909 ± 2
LG10’	57252.9 ± 0.3	8885.2 ± 0.3
HG10’	66178 ± 2.0	8845 ± 1
Mean		8881 ± 26

Table 4.3: Resonant frequencies for cavity modes.

4.3.4 Discussion

The ALS system allows for transfer functions of cavity response to be taken at arbitrary frequencies using integrated aLIGO hardware. No additional optical components are required, and the measurements can be performed with a commercial signal analyzer. The measurements of cavity parameters compare favorably to previous work; the length of the cavity is measured to parts per million accuracy. This also marks the first in-situ measurement of the cavity G-factor of the LIGO interferometer. Cavity scans based on the ALS laser can monitor and characterize the aLIGO arm cavity characteristics in a robust, non-invasive, and automated fashion.

The accuracy of this method can be improved upon in future iterations of the aLIGO arm cavities. The dynamic PDH sideband resonance can be exploited to determine the free spectral range, and thus the length, with increased accuracy [140]. The frequency of the PDH sideband is set by an adjustable RF frequency standard. By adjusting this frequency, the modulation features

$$\nu'_m = (N+1)\nu_{\text{FSR}} - \nu_{\text{PDH}} \tag{4.43}$$

$$\nu_m = \nu_{\text{PDH}} - N\nu_{\text{FSR}} \tag{4.44}$$

can be adjusted until they overlap, determining the free spectral range to within the accuracy of the frequency standard adjustment (1 Hz). At this point of equality, the free spectral range frequency is given by

$$\nu_{\mathrm{FSR}} = \frac{2}{2N+1}\nu_{\mathrm{PDH}} \tag{4.45}$$

where the integer N is determined from estimation of integer numbers of free spectral ranges from the nominal measurement of the transfer function peak. This measurement will be possible after the replacement of the end test masses following the O1 run.

4.4 G-Factor Measurement in a Dynamic Cavity

4.4.1 Introduction

An important application of cavity characterization is the quantification of changes in the arm cavities. Although changes in length are not expected to be a major contribution to changes in the cavity properties, changes in the mirror radius of curvature will occur during interferometer operation. At full power, the arm cavity power build-up will reach 800 kW. Assuming a test mass absorption of 0.5 ppm, 0.4 W of power will be deposited into the mirrors, distorting the test mass substrate [46]. This results in signal degradation in the cavity.

To compensate for this, the Thermal Compensation System (TCS) was introduced. The TCS consists of two subsystems - ring heaters that use resistive heating to heat the outside of the optics, and CO2 lasers with masks to heat the annular ring between the projected heating of the main laser and the outer heating of the ring heater [171].

This work concerns the changes in cavity characteristics induced by the ring heater. The ring heater is designed to control the radius of curvature of the test mass high-reflectivity surfaces. It consists of two semicircular fused silica rods wound with nichrome wire and attached to the suspensions such that they form an annulus around the test mass at a distance of 40 mm from the test mass surface [171], as shown in Figure 4.16. Modeling has shown that heating the exterior of the mirror in

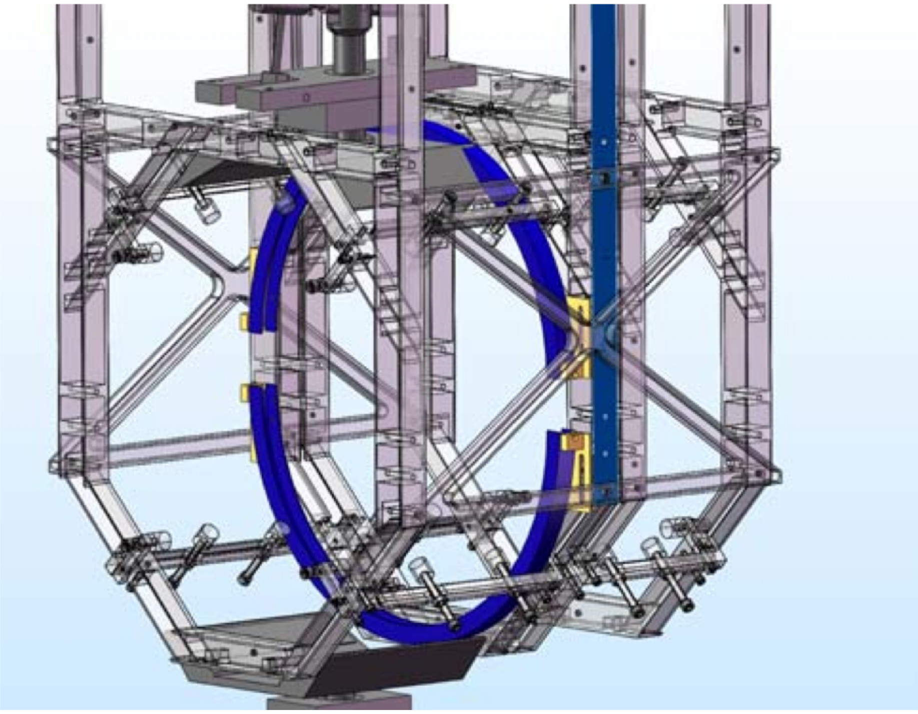

Figure 4.16: Ring heater location in the quadruple pendulum suspension cage. The ring heater (in blue) surrounds the test mass at a distance of 40 mm. Heating the mirror in an axisymmetric pattern results in an approximately spherical change in radius of curvature. Image from [84].

an axisymmetric pattern results in an approximately spherical change of the mirror's radius of curvature. While the ring heater is in operation, the radius of curvature of the mirror will change with a timescale of order hours. Understanding the rate of heating and calibrating the heat supplied is essential to reducing thermal distortions in the interferometer.

Although the main motivation for cavity characterization is to monitor changes in cavity properties, no prior method attempted measurement of changes in cavity parameters in real time. The ring heater characterization proposal pointed out the potential of measurements of shifts in the LG10 and LG20 modes for characterizing the arm cavity's response to the ring heater, but it was uncertain if such a measurement could be performed [48]. The cavity scan method was used to measure dynamic cavity changes during TCS testing during the OAT from August 21, 2012 through September 14, 2012.

4.4.2 Method

To characterize the response of the test mass optics to heating, each mass was heated separately by its respective ring heater for a period of twelve hours. While the ring heater was in operation, cavity scan transfer functions as described in section 4.2 were run in immediate succession, resulting in data points separated by approximately 160 seconds over the operation interval. The position of the HG10 or LG10 mode was measured as a proxy for cavity g-factor, starting from nominal positions determined using equation 4.22,

$$\nu_{HG10} = 46.379 \text{ kHz} \tag{4.46}$$

$$\nu_{LG10} = 55.246 \text{ kHz.} \tag{4.47}$$

Parameter	Cold	Hot
Frequency of LG10	55299 ± 12 Hz	51203 ± 8 Hz
Modal spacing	8893 ± 12 Hz	6845 ± 8 Hz
G-factor	0.735 ± 0.001	0.840 ± 0.001

Table 4.4: Parameters for hot/cold cavity scan shown in Figure 4.17.

The position of the LG10 mode was measured using a peakfinding algorithm. At resonance, the phase undergoes a sign change; this will result in a peak in the derivative of the phase. This phase change is used to quantify the position of the resonance, and measure the LG10 peak. Using equation 4.36, the G-factor is calculated from the change in the modal spacing. The change in radius of curvature can be inferred by assuming that the radius of curvature for the unheated test mass is known and constant. By rearranging the definition of g-factor given in equation 4.24, the radius of curvature for a given optic R_1 is

$$R_1 = \frac{L(R_2 - L)}{R_2(1 - G^2) - L}. \tag{4.48}$$

For these estimates, it was assumed that R_{ETM} and R_{ITM} were initially equal, such that $G = g_{\mathrm{ITM}} = g_{\mathrm{ETM}}$. For the measured $G = 0.7367$, this corresponds to an assumed $R_{\mathrm{approx}} = 2300$ m.

4.4.3 Results

To test if the predicted modal shift was observed, the ETM ring heater was engaged with a requested power of 630 mA, corresponding to 13.8 W output power from the ring heater, and the frequency of the LG10 mode was measured. The results are shown in Figure 4.17.

To test the performance over time and the radius of curvature change, the ETM was operated at 315 mA, 3.47 W for a period of 12 hours. The results of this measurement are shown in Figure 4.18.

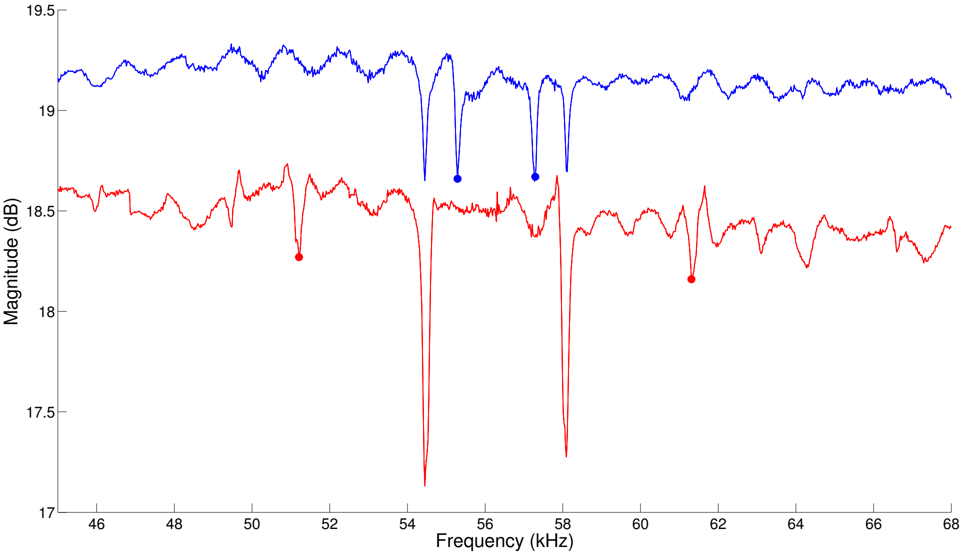

Figure 4.17: Change in modal spacing with cavity heating. Two measurements were performed using an SR785 signal analyzer in swept-sine configuration, with frequencies from 33 kHz to 80 kHz; frequencies from 45 to 68 Hz are shown. The supplied power from the signal analyzer was 10 mV, corresponding to a modulation depth of 0.1. The first measurement (blue trace) was performed in an unheated cavity. After the first measurement, the ETM ring heater was engaged with a power of 13.8 W. The second measurement (red trace) was performed after approximately two hours of heating, showing a shift in the resonant frequency of the Laguerre-Gauss (1,0) cavity modes; the initial positions of the modes are denoted by the blue points, while the final positions are denoted by the red points.

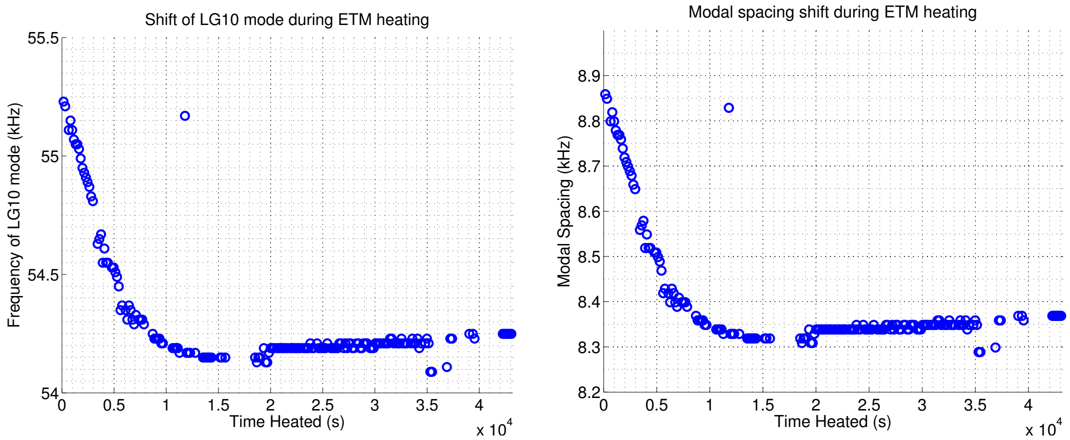

(a) Shift in Laguerre-Gauss (1,0) mode.

(b) Shift in modal spacing.

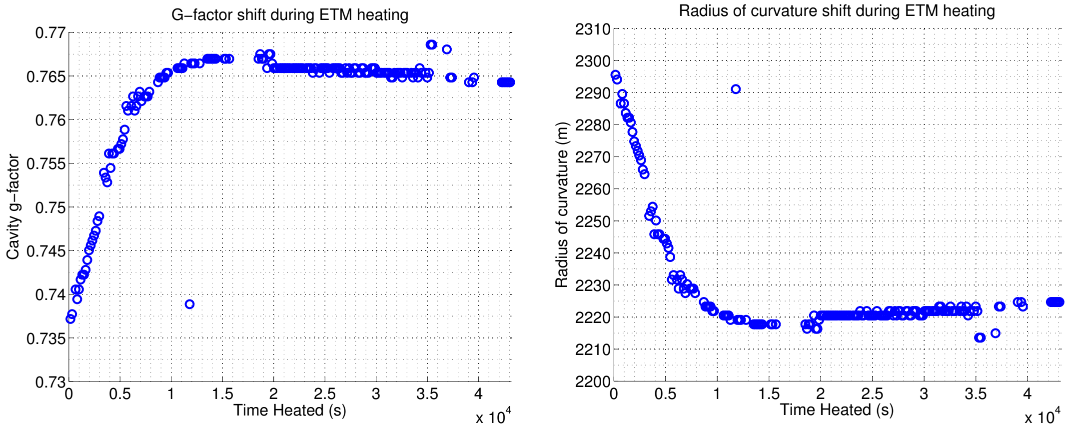

(c) Shift in cavity g-factor.

(d) Shift in radius of curvature.

Figure 4.18: Results of ETM heating cavity scan. Continuous cavity scans were run while the ETM ring heater was operated at a power of 13.8 W for a period of 12 hours to determine the time constant and magnitude of thermal deformation. This measurement was performed using an SR785 signal analyzer in swept-sine configuration, with frequencies from 33 kHz to 80 kHz. The supplied power from the signal analyzer was 10 mV, corresponding to a modulation depth of 0.1. The location of the LG10 mode was determined from the point of phase change at the resonance. The outlier at $\sim 1.2 \times 10^4$ s and the gap in data between $\sim 1.6 \times 10^4$ s and $\sim 1.8 \times 10^4$ s were due to loss of cavity lock during the overnight measurement.

4.4.4 Discussion

No previous measurement of Laser Interferometer Gravitational-Wave Observatory (LIGO) arm cavity properties had been carried out during a controlled cavity change. Therefore, modal separation measurements to quantify changes in the arm cavities during operation had not been possible. The characterization of the ring heater performance using the ALS cavity scan method was the first such measurement conducted during a controlled change. The ALS cavity scan method achieves the goal of directly measuring changes in cavity properties. The constraining requirement for this method is the necessity for the laser to remain in a stable lock to the cavity. The outliers and gaps observed in the cavity scanning data in Figures 4.18 4.19 are due to a loss of cavity lock during the scanning process.

The cavity scan method was used to quantify the performance of the ring heater. During the heating tests, data from the cavity scans was used to diagnose an issue with the fabrication of the gain stage for the ETM ring heater controller. Comparisons of the rates and degree of radius of curvature change from full scan data to finite-element modeling (Figure 4.19) showed that the measured change was ∼29% larger than the model, and was used to motivate improvements to the finite element modeling process for the test masses [47].

A major advantage of the ALS cavity scan is that it uses an integral part of the aLIGO ISC system, the locking of the auxiliary green laser to the arm cavity, to measure cavity properties. With the addition of a signal analyzer and GPIB controller, the ALS system can be used to measure real-time changes in the arm cavity. This system can be used to characterize, calibrate, and diagnose the changes induced by the TCS ring heater, improving the control of the thermal lens and therefore instrument stability. This cavity scan method requires no additional dedicated equipment or maintenance, and is a powerful diagnostic tool for characterizing the arm cavities.

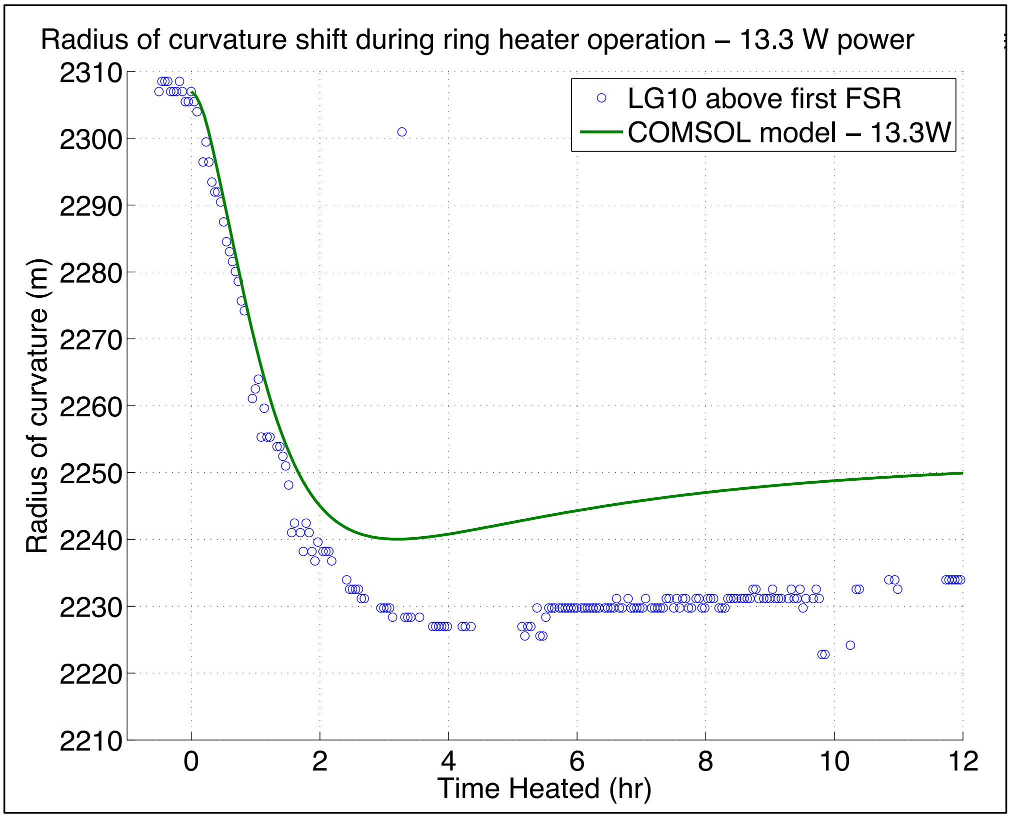

Figure 4.19: Comparison of observed change in ETM radius of curvature to COMSOL model [47]. The data presented in Figure 4.18 was used to verify the results of finite-element modeling for independent calibration of the degree and timescale of the thermal deformation of core optic substrates by the ring heaters.

Optic	Measured Transmission
H1 ETMX	32.73%
H1 ETMY	31.6%
L1 ETMX	51%
L1 ETMY	38.3%

Table 4.5: Measured end test mass transmission at 532 nm.

4.5 Implementation of Differential Wavefront Sensing

4.5.1 Introduction

The cavity scan was performed on an arm cavity that was temporary by design. The optical substrates and coatings had been used for testing fabrication and coating methods, and were damaged in the process. Between the HIFO-Y and HIFO-XY tests, the final aLIGO optics were installed in the arm cavities, including substrates with the correct radius of curvature and distinct ITM and ETM coatings. Due to the lower design value of ETM 532-nm reflectivity, the finesse was expected to decrease to ∼100. Although the lower finesse would make the arm more sensitive to changes in alignment, the stability observed during OAT and HIFO-Y was such that the arm cavity would have sufficient stability without dynamic auto-alignment [153]. However, during HIFO-XY at LHO, the green arm lock was unstable, and sensitive to the environmental impact of high winds at the site to a degree that was inconsistent with the observations made of the cavity during previous integration tests.

The source of the locking issues was the ETM optical coatings. Although the specifications for the coatings called for transmissions at 532 nm between 2-4%, the real values of the transmission are between 31.6% and 51% [63][31][122][121].

Assuming an ITM transmission of 99%, the measured transmissions imply finesse values between 8 and 14. The lower finesse, combined with the altered cavity geometry, results in a sensitivity of beam position to motion in the cavity three times greater than that observed during OAT and HIFO-Y [154]. The end test masses could not be replaced before the target date for the end of aLIGO installation, so to complete aLIGO integration and proceed to data-taking, the arm cavity needed additional alignment controls.

A standard method for measuring the alignment state of a Fabry-Perot optical cavity is differential wavefront sensing. Differential wavefront sensing takes advantage of the differing propagation characteristics of higher-order modes in the cavity to determine the cavity alignment state [27]. When Gaussian beams propagate, the beam radius evolves as

$$\frac{\pi w_0^2}{\lambda R} = \frac{\lambda}{\pi w^2}(z - z_0), \tag{4.49}$$

and the wavefront curvature evolves as

$$1 - \frac{w_0^2}{w^2} = \frac{1}{R}(z - z_0), \tag{4.50}$$

where z_0 is the waist location and w_0 is the beam size at the waist. When a field is injected into the cavity, there is a directly reflected beam from the first mirror, E_{IR}. This interacts with the part of the resonant beam leaking back through the input mirror, E_{RC}. If the cavity is perfectly aligned, E_{IR} and E_{RC} overlap. If the cavity mirrors are misaligned, E_{RC} will be contaminated with higher-order modes, and the combination field will no longer overlap. Differential wavefront sensing measures the angle and lateral displacement between the wavefronts of E_{IR} and E_{RC}, then uses this signal to align the cavity and cancel the misalignment. For an alignment axis defined by the laser light incident on the interferometer, the misalignment angle between the alignment axis and the resonant axis at the beam waist is given by

$$\Theta_W = \arctan\left(\frac{\gamma z_R}{\Delta x}\right), \tag{4.51}$$

where γ is the angle between the ideal cavity axis and the misaligned axis, and Δx is the lateral displacement of the misaligned beam at the waist position. The higher-order modes will propagate with different Gouy phases (Equation 4.17), resulting in a displacement angle Θ^d between the higher order modes and the fundamental Gaussian mode. For the Hermite-Gauss (1,0)/(0,1) modes, this displacement angle is given by

$$\Theta^d = \frac{\gamma z_R}{\Delta x} + 2 \arctan\left(\frac{z - z_0}{z_R}\right). \tag{4.52}$$

Measuring Θ^d gives a linear combination of information about the angular and lateral displacement of the beam in the cavity. The near field, $z - z_0 << z_R$, is sensitive to angular misalignment, while the far field, $z - z_0 >> z_R$, is sensitive to lateral displacement. In practice, two detectors are spaced by 90° in Gouy phase, allowing separation of variables. The detectors are based on quadrant photodiodes; the horizontal differential measurement gives Θ^d for yaw, while the vertical differential measurement gives Θ^d for pitch. These signals are then converted to the basis of hard and soft optomechanical eigenmodes for cavity control [60].

Differential wavefront sensing had been used for interferometer sensing and control purposes in iLIGO [60], and the original ALS designs included differential wavefront sensing. However, during OAT, the wavefront sensors were found to be of little value for alignment and control. Therefore, they were removed from the aLIGO designs for ease of use and reduction of maintenance [153].

To control the aLIGO arm cavities, the differential wavefront sensing system had to be redesigned for implementation in the ALS system. Due to its removal after OAT, no new wavefront sensor (WFS) hardware had been produced, and the legacy hardware from iLIGO had to be updated for use in aLIGO. The optical path had to be redesigned to account for the change in table geometry between the inital design and the design after the removal of the WFS beam paths. The system then had to be tested to determine if the additional alignment control from differential wavefront sensing was sufficient to proceed with the aLIGO installation schedule, or if new optics would need to be coated and installed prior to aLIGO operation, delaying the beginning of data-taking by months.

4.5.2 Electronic Design of ALS WFS

The legacy WFS is based on a YAG-444A-4 quadrant photodetector. The response from each quadrant passes through a resonant circuit to selectively filter response at the modulation frequency of the laser of interest, which is amplified by a gain stage before transmission to the control system. Fortunately, the installed photodetector is sensitive to 532-nm light, as well as the 1064-nm light used in iLIGO systems. Assuming that the photodiodes and gain stages were not damaged at any point during or prior to storage, the only component requiring alteration was the resonant circuit.

The modulation frequency of the ALS laser is 24.5 MHz, and iLIGO WFS were tuned to frequencies of 24.4, 26.7, 33.2, 61.2, and 68.6 MHz. The iLIGO WFS tuned to 24.4 MHz can be used without alteration; however, there were an insufficent number of 24.4 MHz units available, and other units had to be tuned to the new frequency. This modification was not straightforward due to mechanical elements of the WFS design. The tunable inductors were hand-wound on ferrite cores. The elements used are no longer commercially available, and the pinouts are not compatible with modern RF inductors. Therefore, modeling and testing was undertaken to determine how to best adapt the old circuits to the new frequency.

Due to the constraints set by the inductors, the 26.7 MHz WFS were adapted to the ALS frequency. Using analog circuit simulation, the response of the resonant circuit was modeled to determine a viable point of modification. As built, the 26.7 MHz WFS had a 6.8 pF capacitor installed that was not electrically connected. Modeling showed that installing a shunt to connect this capacitor and reversing the tunings of the variable inductors in the circuit, as shown in Figure 4.20, was sufficient to bring the resonant frequency down to 24.5 MHz. The predicted resonant response is shown in Figure 4.21.

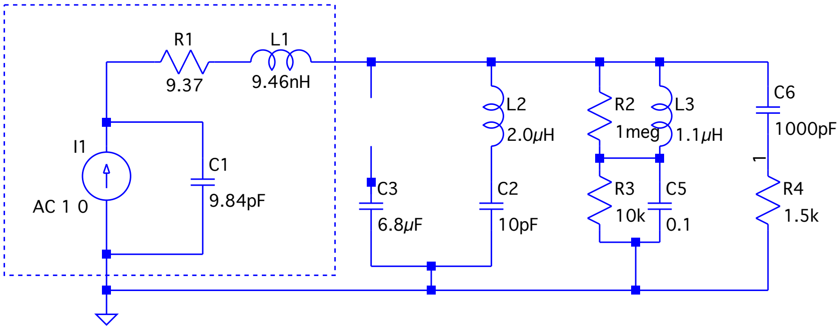

(a) Initial (26.7 MHz)

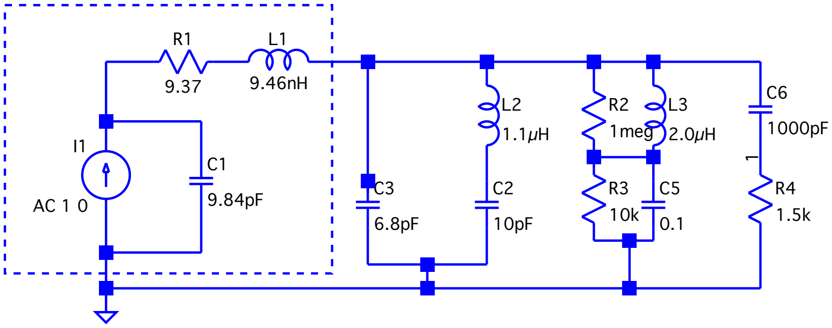

(b) Modified (24.5 MHz)

Figure 4.20: Schematics for initial and modified WFS resonant circuits. The components enclosed by the dashed box represent the YAG-444A-4 photodetector response. In the initial circuit, capacitor C3 is installed but not electrically connected. The shunt adds this additional capacitance in parallel with the trap formed by L2 and C2. The inductors L2 and L3 are identical variable inductors; nominal tunings are shown.

The measured response of the resonant circuit is shown in Figure 4.22. The reduced gain is due to insufficient biasing of the photodetector; the highest bench supply available was −60 V, and as designed and installed, the photodetector is biased with −100 V, increasing the peak photodetector power. The resonant peak appears as predicted by the model, with the resonant frequency of 24.4 MHz sufficient to filter the response of the photodetector to select signals at the ALS laser frequency. Wavefront sensors with this shunt modification are used in the aLIGO ALS system at both LHO and LLO.

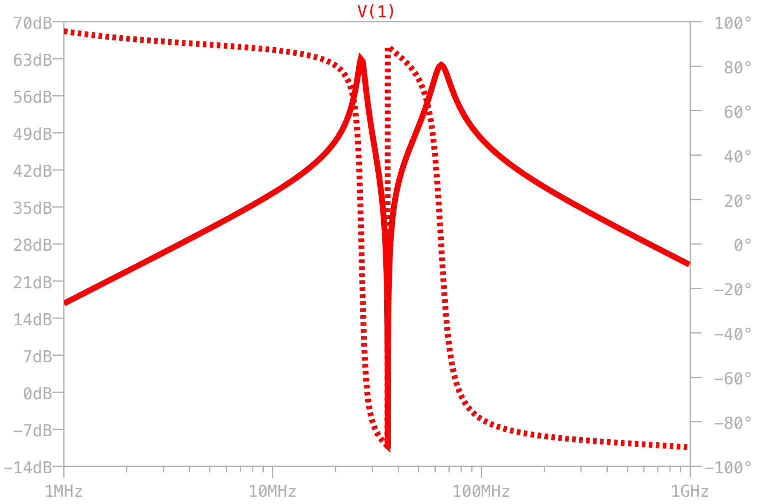

(a) Initial (26.7 MHz)

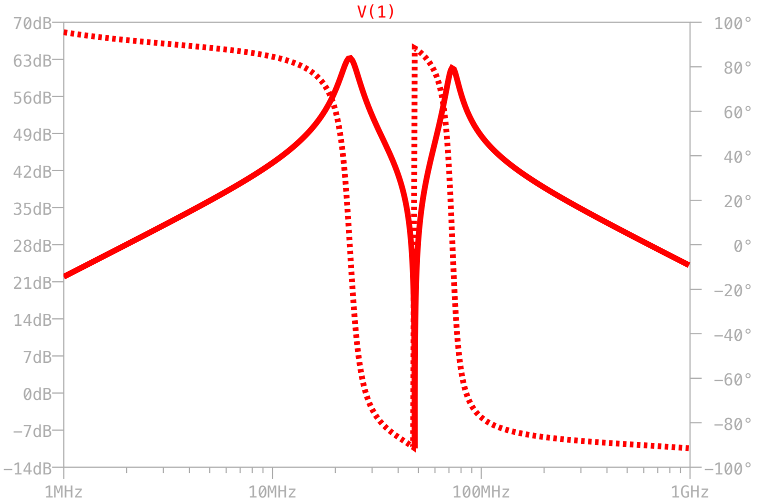

(b) Modified (24.5 MHz)

Figure 4.21: Modeled response for initial and modified WFS resonant circuits. The solid line is the amplitude response and the dashed line is the phase response. The modifications made to the circuit shifts the first resonant peak from 26.7 MHz to 24.5 MHz, with the added effect of broadening the frequency peak. This frequency response was modeled using SPICE.

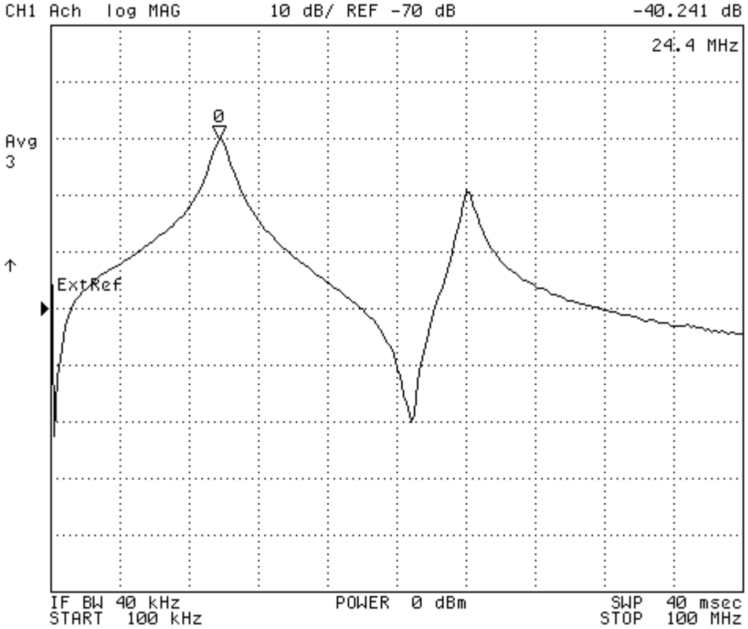

Figure 4.22: Measured response for modified WFS resonant circuit. Note the broadened resonant peak at 24.4 MHz, appropriate for filtering at 24.5 MHz. The lower gain is attributed to test procedures; the photodiode input was not perfectly coupled to the RF-modulated laser used for signal injection, and the photodiode itself was biased at −60V instead of −100V due to availability of test equipment. This measurement was made during the process of tuning the inductors, using an HP 4395A RF signal analyzer.

Component	distance (m)
BS to first lens (R = 250mm)	0.1
First lens to second lens (R = -75 mm)	0.151
Second lens to WFS (ideal)	0.351
Second lens to WFS (range)	0.13 - 0.41

Table 4.6: Calculated parameters for WFS near field.

4.5.3 Optical Design of ALS WFS

In order to use the WFS for cavity control, the retroreflected electromagnetic field $E_{IR} + E_{RC}$ must be projected onto two wavefront sensors. The nominal Gouy phase separation requirement is $90^\circ \pm 10^\circ$, and the ideal beam diameter for differential sensing by the quadrant photodetector is between 2.5 and 4 mm. As the beam path was added after the table was in operation, the design was physically constrained to the open space on the ISC end station tables. A pickoff was available from a Length Sensing and Control (LSC) photodiode path, but the limited space available presented difficulties in choosing a precise distance for placement of wavefront sensors.

When a Gaussian beam passes through a converging lens, it is focused to a new waist at approximately the focal length of the lens. The Gouy phase changes by 180° as it passes through this waist. In theory, it is possible to set a Gouy phase difference of 90° between the wavefront sensors using one lens, placing one at the waist and one near the maximum of Gouy phase. However, reliability and maintenance concerns make a one-parameter solution unattractive for operational use.

Each of the near-field and far-field paths use a Gouy phase telescope to simultaneously adjust the Gouy phase and the beam size on the wavefront sensors. Both solutions use two lenses to expand the beam size while keeping the Gouy phase constant. This allows for a tunable solution, easily altered to account for changes in beam or table geometry.

Note that the Gouy phase characteristics for the near field remain good even when the placement of the near field wavefront sensor is nearly touching the second

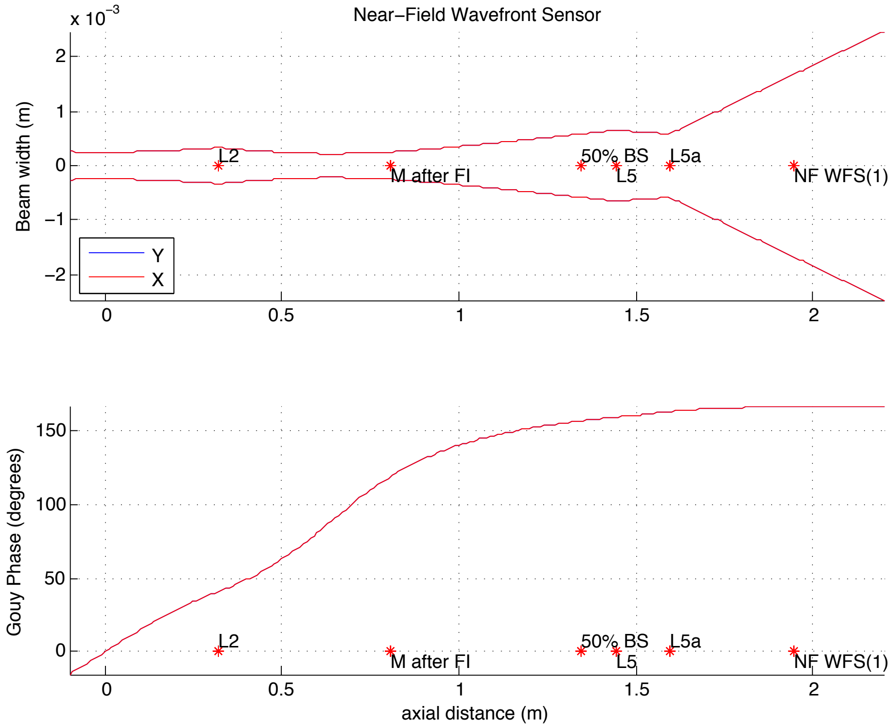

Figure 4.23: Modeled beam properties for near field WFS path. L2 and Mirror after Faraday Isolator are elements of the RFPD path. The first lens (L5) has radius of curvature R = 250mm. The second lens (L5a) has radius of curvature R = -75mm. This solution sets the Gouy phase at 160 degrees through the Gouy phase telescope for the near field, and expand the beam after the second lens to meet the spot size requirements.

lens. The primary consideration in the layout of the near field wavefront sensor path is achieving an appropriate spot size at the wavefront sensor. The Gouy phase characteristics are a stricter constraint on the placement of the far field wavefront sensor. The distance between the second lens and the far field wavefront sensor must be at least 0.42 m. Fortunately, there is a fairly large range of acceptable distances and it is not strictly necessary to have 2.5 m of beam path after the beamsplitter.

The wavefront sensing path layouts differ between the X-arm ALS table (ISCTEX) and the Y-arm ALS table (ISCTEY) due to the differing physical constraints of the two tables. The near field paths are more optically similar, but their layouts clearly

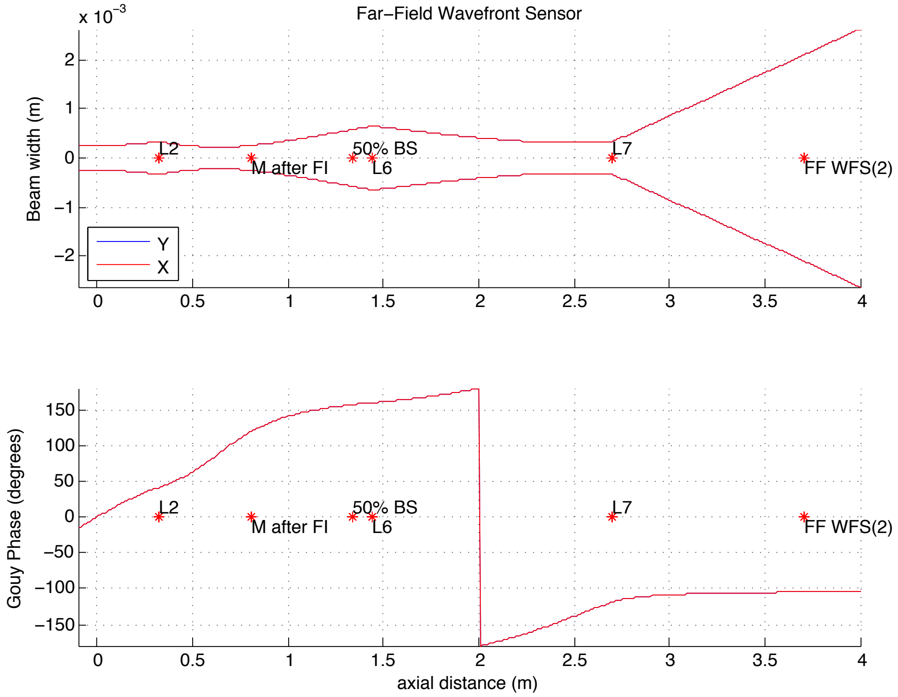

Figure 4.24: Modeled beam properties for far field WFS path. L2 and Mirror after Faraday Isolator are elements of the RFPD path. The first lens (L6) has radius of curvature R = 250mm. The second lens (L7) has radius of curvature R = -100mm. This solution sets the Gouy phase at -110 degrees, and expands the beam after the second lens to meet the spot size requirements.

Components	distance (m)
BS to first lens (R = 250mm)	0.1
First lens to second lens (R = -100 mm)	1.355
Second lens to WFS (ideal)	1.004
Second lens to WFS (range)	0.422 - 1.092

Table 4.7: Calculated parameters for WFS far field.

Distance	d_X (m)	d_Y (m)
BS to L5	0.14	0.14
L5 to L5a	0.14	0.14
L5a to WFSA	0.34	0.25

Table 4.8: Installed parameters for WFS near field.

differ between the two tables. On ISCTEX, there is space to place the near field wavefront sensor next to the ALS periscope. On ISCTEY, the open space between the periscopes is not accessible due to the location of the IR transmission periscope, requiring the use of a shorter path with a single folding mirror for the near field path.

The far field path is similar between the two tables. The optical components are identical, with some difference in their placement on the table. On ISCTEX, the first folding mirror was placed directly above the Hartmann sensor already in place. On ISCTEY, the layout was more conservative to accommodate the later installation of the Hartmann Wavefront Sensor path. This constraint on path length resulted in a shorter overall beam path on ISCTEY, still within the tolerances for the design.

The nominal ISCTEY solution was later tested [92]. Due to variances in retroreflected beam quality, modifications had to be made to the lens positions on the ISCTEY paths. The design principles allowed for a quick and effective modification.

Distance	d_X (m)	d_Y (m)
BS to L6	0.15	0.14
L6 to L7	1.46	1.28
L2 to WFSB	0.9525	0.457

Table 4.9: Installed parameters for WFS far field.

Distance	Near Field (m)	Far Field (m)
BS to L1	0.10	0.65
L1 to L2	0.14	1.65
L2 to WFS	0.13	0.81

Table 4.10: Modified parameters for WFS far field.

4.5.4 Discussion

The ALS WFS are currently in use for control of the arm cavities in aLIGO, and are an integral part of arm cavity alignment. The optical paths as laid out allow for control of the cavity with 532-nm light, despite the issues with finesse; the improvements made by the implementation of differential wavefront sensing were such that the flawed ETM coatings were able to be used in the aLIGO instrument. Without the availability of WFS, the arm cavity stability would be insufficient for the operation of aLIGO; its implementation was vital to the success of the first operational run.

4.6 Summary of Contributions

During the ISC commissioning process at LHO, the author developed a method to characterize the properties of the Fabry-Perot resonant arm cavity using the ALS optics and control electronics. Using this method, the length of the arm cavity was measured to an accuracy of less than 1 mm over 4 km and the first in-situ measurement of the LIGO cavity G-factor was made. This new method was extended to measure the change in mirror radius of curvature from a controlled thermal deformation, providing an external check on the performance of the aLIGO Thermal Compensation System.

The author also implemented a differential wavefront sensing subsystem used for initial arm cavity control in the aLIGO locking process to compensate for the effect of high 532-nm transmission in the ETM optical coatings. The scope of this project included modifying legacy wavefront sensing hardware for use in aLIGO and determining a tunable beam path solution within the physical constraints of the optical table.

CHAPTER V

Multimessenger Pulsar Astronomy with LIGO

5.1 Gravitational Wave Emission from Rotating Neutron Stars

Rotating non-axisymmetric neutron stars in the Milky Way galaxy are a promising source for continuous gravitational waves in the frequency range of ground-based gravitational wave detectors. In the accepted model of neutron star production, a neutron star is one possible end stage of the evolution of stars with masses $\geq 8M_\odot$ [76]. When a main sequence star is in equilibrium, the outward pressure produced by fusion of hydrogen to helium in the stellar core equals the inward force of gravity. The supergiant stage of stellar evolution is triggered by the exhaustion of hydrogen fuel in the core of a massive main-sequence star. The star then fuses progressively heavier elements, continuing until iron is the primary fusion product [76]. The fusion of iron is endothermic and requires additional energy input; fusion stops in the core, and the core of the dying star is supported by electron degeneracy pressure unless it reaches the Chandrasekhar mass limit,

$$M_{Ch} \simeq \frac{3.1}{\mu_e^2}\left[\frac{hc}{G}\right]^{3/2} \simeq 5.83\mu_e^{-2}M_\odot, \tag{5.1}$$

where μ_e is the average number of nucleons per electron [102]. At this point, it is energetically favorable for the protons and electrons in the core of the star to undergo inverse beta decay to form neutrons. The star can no longer support itself against its own gravity, a core-collapse supernova occurs, and the remaining core material becomes a neutron star [76].

The resultant neutron star is a sphere with a typical mass of 1.2 - 1.5 $M_\odot$ and a typical radius of approximately 10 km. The non-uniform density inside a neutron star reaches $\rho_{NS} = 6.7 \times 10^{14}$ g cm^3, more than twice the density of nuclear matter, $\rho_s = 2.7 \times 10^{14}$ g cm^3 [110]. At this extreme density, it is energetically advantageous for protons and electrons to associate and form neutrons. From observations of *glitches*, sudden changes in the rate of neutron star rotation, it is thought that neutron stars have at least two layers. The conventional model of a neutron star is that the core is a superconducting superfluid of 95% neutrons in equilibrium with 5% electrons and protons supporting the star through neutron degeneracy pressure, while the crust is a solid crystalline lattice of heavy ions approximately 1 km thick [110]. More exotic states of matter could be found at the extreme density of neutron star cores, including pion or kaon condensates [110], solid strange quark cores, and crystalline quark cores [28] [76].

Neutron stars are appealing gravitational wave source candidates because of their high moment of inertia and rotational velocity. Assuming that the density profile of the neutron star is sufficiently uniform to allow approximation using the moment of inertia of a sphere,

$$I_{sph} = \frac{2}{5} M R^2, \tag{5.2}$$

for a neutron star with a mass of 1.4 $M_\odot$ and a radius of 10 km, the moment of inertia is

$$I_{NS} \sim 10^{38} \left(\frac{M}{1.4 M_\odot} \right) \left(\frac{R}{10^4} \right)^2 \text{ kg m}^2. \tag{5.3}$$

The core collapse process causes the significant rotational velocity observed in neutron stars; supergiant stars have radii on the order of 10^6 km, and during the collapse to a neutron star of radius 10 km, conservation of angular momentum causes the stars to be born spinning at a rapid rate [76]. Neutron stars in binary systems can also be spun up due to accretion from their binary partner. These recycled pulsars have been observed with spin frequencies as high as 716 Hz [85], corresponding to a surface velocity of approximately $0.15c$. Therefore, neutron stars are both compact and relativistic, satisfying the requirements set forth in Chapter II for promising gravitational wave emitters.

What is less clear is if neutron stars have significant quadrupole moments. Recalling equation 2.55,

$$h_0 = \frac{4\pi^2 G I_{zz} f^2}{c^4 r}\epsilon = (1.1 \times 10^{-24}) \left(\frac{I_{zz}}{I_0}\right) \left(\frac{f_{GW}}{1\text{ kHz}}\right)^2 \left(\frac{1\text{ kpc}}{d}\right) \left(\frac{\epsilon}{10^{-6}}\right), \tag{5.4}$$

the emitted strain due to gravitational waves is proportional to the ellipticity of the neutron star,

$$\epsilon \equiv \frac{I_{xx} - I_{yy}}{I_{zz}}. \tag{5.5}$$

Little is known about the maximum sustainable ellipticity of neutron stars. The upper limit on non-axisymmetry is set by the breaking strain of the crust u_{break} [28]. Detailed models of crustal strains suggest the relation between breaking strain and ellipticity is

$$\epsilon < 2 \times 10^{-5} \left(\frac{u_{\text{break}}}{0.1}\right). \tag{5.6}$$

Molecular dynamics simulations have shown that the breaking strain of the crust may be as great as 0.1, a remarkable number considering terrestrial materials have breaking strains between 10^{-4} - 10^{-2} [28]. For a conventional neutron star, this maximum ellipticity corresponds to a deformation of 20 cm over the 10 km body. Neutron stars with exotic cores may support higher ellipicities; for the same breaking strain, a solid strange quark star may support ellipticities of up to 6×10^{-4} [129], and a crystalline color superconducting quark phase may support ellipticities of up to 10^{-2} [83]. Gravitational wave observations may therefore distinguish between models of neutron star core composition; detection of gravitational waves at unexpectedly high strengths may provide evidence for alternative neutron star cores.

The mechanism of non-axisymmetry production is equally ill-understood, and will likely depend on the material properties of the neutron star crust and the formation history of individual neutron stars. Distortion of the neutron star due to its internal magnetic field is a probable source of non-axisymmetry; however, this is a very low-level effect in normal neutron stars, with projected ellipticities of order

$$\epsilon \simeq 10^{-12} \left(\frac{B}{10^{12}\ \mathrm{G}} \right). \tag{5.7}$$

For normal neutron stars, this sets a lower bound on ellipticity related to its magnetic field [28]. This effect may be more pronounced if the core of the neutron star is a type II superconductor, in which case,

$$\epsilon \simeq 10^{-2} \left(\frac{B}{10^{12}\ \mathrm{G}} \right) \left(\frac{B_{\mathrm{crit}}}{10^{15}\ \mathrm{G}} \right), \tag{5.8}$$

where B_{crit} is the critical magnetic field [28]. Accretion provides another mechanism for non-axisymmetry production; the accretion of material along magnetic field lines is a promising formation route for magnetically-supported neutron star mountains [116].

Oscillatory modes in the internal fluid of the neutron star are another possible mechanism for the generation of non-axisymmetry. The most promising modes are the r-modes, one of the inertial modes of a rotating star restored by the Coriolis force [29]. The r-modes are of particular interest for gravitational wave detection because they are unstable due to the emission of gravitational radiation. Gravitational waves due to r-modes will be emitted at a frequency of approximately $\frac{4}{3}f_{rot}$ [90], with an amplitude of [130]

$$h(t) = 4.4 \times 10^{-24}\alpha \left(\frac{\Omega}{\sqrt{\pi G\bar{\rho}}}\right)^3 \left(\frac{20\ \mathrm{Mpc}}{D}\right), \tag{5.9}$$

where Ω is the angular velocity of the system and α is the amplitude of the r-modes. The frequency assumes the interior of the neutron star is a slowly rotating, barotropic, Newtonian perfect fluid, and deviations from this model will cause drift in the precise r-mode frequency [90].

In the absence of internal non-axisymmetry, spinning neutron stars can have quadrupole moments if the spin axis and the axis of symmetry are misaligned, causing the star's axis of rotation to precess or "wobble". For a precessing neutron star with wobble angle θ_W, gravitational wave signals can be emitted at twice the rotation frequency and at the sum of the rotation and precession frequencies, $f = f_{\mathrm{rot}} + f_{\mathrm{pre}}$, with magnitude

$$h_0 \sim 10^{-27} \left(\frac{\theta_W}{0.1\ \mathrm{rad}}\right) \left(\frac{1\ \mathrm{kpc}}{d}\right) \left(\frac{f_{\mathrm{rot}}}{500\ \mathrm{Hz}}\right)^2. \tag{5.10}$$

However, damping rates suggest that it is unlikely that gravitational waves due to neutron star precession will be observed [137].

5.2 Searches for Continuous Gravitational Waves

5.2.1 Signal Model

For all the production mechanisms discussed above, the gravitational-wave emission from a rotating neutron star is well-modeled by a sinusoid with a slowly time-varying frequency. The signal detected by the interferometer can be written as

$$h(t) = F_+(t, \phi) h_0 \frac{1 + \cos^2(\iota)}{2} \cos(\Phi(t)) + F_\times(t, \phi) h_0 \cos(\iota) \sin(\Phi(t)), \tag{5.11}$$

where ι is the inclination angle between the star's spin direction and the propagation direction of the wave, F_+ and $F_\times$ are the detector antenna response pattern to the plus and cross polarizations, and $\Phi(t)$ is the phase of the signal [144]. To zero order, a continuous gravitational wave signal can be extracted from detector data by taking the Fourier transform of the output and observing an improbably strong signal at the emission frequency [147]. However, periodic continuous wave signals do not remain at the same frequency. The emission of radiation, both gravitational and electromagnetic, carries energy away from the neutron star. The loss of energy causes the spin frequency of the neutron star to decrease. Electromagnetic observations show this *spindown* effect, proving that neutron star energy emission is primarily due to rotations rather than oscillations; energy emission due to oscillations would decrease in amplitude, but not in frequency [76].

If spindown is not accounted for, the gravitational wave signal will be smeared across frequency bins, causing signal degradation. To account for the change in frequency, the phase of the signal is typically represented as a Taylor series,

$$\Phi(t) = \Phi_0 + 2\pi \left[f_s(T - T_0) + \frac{1}{2}\dot{f}_s(T - T_0)^2 + \frac{1}{6}\ddot{f}_s(T - T_0)^3 + ... \right], \tag{5.12}$$

truncated at the term of interest, where T_0 is a reference time selected by the experimenter [28]. For an observation with a given signal integration time T_{obs}, the frequency resolution Δf is

$$\Delta f = \frac{1}{T_{obs}}. \tag{5.13}$$

For an observation of length one day, the frequency resolution is 1.157×10^{-5} Hz. Assuming a fairly typical spindown value of $\dot{f} = -10^{-9} Hz/s$, over the course of the observation the frequency will change by 8.64×10^{-5} Hz. Therefore, continuous gravitational wave signals must be described by phase evolution models rather than single-frequency sinusoids.

In real instruments, periodic noise sources can also cause spectral lines in the data output. Fortunately, continuous wave signals can be distinguished from spectral lines through observation of frequency and amplitude modulation due to the Earth's motion or coincident detection in multiple interferometers. The motion of the Earth must be taken into account when searching for continuous gravitational waves, as an astronomical signal will be Doppler-shifted by the Earth's motion. For a given signal frequency f_0, the effect of the Doppler shift on the signal frequency is given by

$$f = f_0 \left(1 + \frac{\vec{v} \cdot \hat{r}}{c}\right). \tag{5.14}$$

The Doppler shift of the frequency will smear the signal across adjacent frequency bins. An efficient method for preventing signal degradation due to the Doppler shift is transforming the signal into the domain of barycentric time, T [56]. The barycentric time is defined as

$$T = t + \Delta_{\text{Roemer}} + \Delta_{\text{Shapiro}} + \Delta_{\text{Einstein}}, \tag{5.15}$$

where the Roemer delay Δ_{Roemer} accounts for the light travel time between the Earth and the solar system barycenter (SSB),

$$\Delta_{\text{Roemer}} = -\frac{\vec{r} \cdot \hat{n}}{c} + \frac{(\vec{r} \cdot \hat{n})^2 - |\vec{r}|^2}{2cD}, \tag{5.16}$$

the Shapiro delay Δ_{Shapiro} accounts for the curvature of spacetime near the sun, and the Einstein delay Δ_{Einstein} accounts for the gravitational redshift. Here, $\vec{r}$ is the position vector between the detector and the SSB, $\hat{n}$ is the unit vector between the SSB and the source, and D is the distance to the source. By representing the arrival time of the signal at the fixed solar system barycenter, the effect of the Doppler shift from detector motion is removed. The barycentering process requires the specification of a sky position. Each point on the sky has a unique barycentering solution; therefore the barycentering of gravitational wave data imposes a pointing upon a given gravitational wave search. The angular resolution of a continuous wave search is defined by the area on the sky for which a single barycentering solution can be applied, to some experimenter-defined acceptable level of signal degradation or *mismatch*. The angular resolution of a pointing is inversely proportional to the frequency of the signal and the integration time of the search,

$$\Delta\Theta \propto \frac{1}{fT_{obs}}. \tag{5.17}$$

Consequently, a continuous gravitational wave signal can be localized with increasing precision as the integration time of the search is increased [148]. This feature of continuous gravitational wave searches allows for localization of signals and allows for searches for gravitational waves from known objects of interest.

5.2.2 Detecting Gravitational Waves

The detection of gravitational waves is best understood as a statistical process [87]. The output of the detector, $x(t)$, is taken as a sample from an underlying probability distribution. In the absence of a gravitational wave, the samples are incidences of the detector noise $n(t)$. The action of a gravitational wave on the detector changes this probability distribution by imposing a signal $s(t)$ on the output. In the frequentist interpretation, the process of gravitational wave detection can be characterized as a hypothesis test [87], seeking to distinguish between the null hypothesis $\mathcal{H}_0$ and the test hypothesis $\mathcal{H}_1$,

$$\mathcal{H}_0 : \qquad x(t) = n(t) \tag{5.18}$$

$$\mathcal{H}_1 : \quad x(t) = n(t) + s(t) \tag{5.19}$$

To distinguish between the two hypotheses, a detection statistic $\Lambda(x)$ is defined such that for a threshold Λ^*, the null hypothesis $\mathcal{H}_0$ is accepted for $\Lambda(x) < \Lambda^*$ and the alternative hypothesis $\mathcal{H}_1$ is accepted otherwise. The false alarm probability is the probability that the detection threshold is met or exceeded when the null hypothesis is true,

$$f_A(\Lambda^*) = \int\limits_{\Lambda^*}^{\infty} P(\Lambda|\mathcal{H}_0) d\Lambda, \tag{5.20}$$

while the false dismissal probability is the probability that the detection threshold is not met when the alternative hypothesis is true,

$$f_D(\Lambda^*) = \int\limits_{-\infty}^{\Lambda^*} P(\Lambda|\mathcal{H}_1) d\Lambda. \tag{5.21}$$

The detection probability is then

$$\eta(\Lambda^*) = \int\limits_{\Lambda^*}^{\infty} P(\Lambda|\mathcal{H}_1) d\Lambda. \tag{5.22}$$

The form of the detection statistic Λ is chosen to be an optimal test statistic. The Neyman-Pearson design criterion states that an optimal test maximizes the detection probability η for a given false alarm rate f_A [137][87]. The optimal test for distinguishing between the two hypotheses presented in equation 5.18 is the *likelihood ratio*, the ratio between the probability that the signal is present in the data, $P(x(t)|\mathcal{H}_1)$, and the probability the the signal is not present in the data, $P(x(t)|\mathcal{H}_0)$.

$$\Lambda(x) \equiv \frac{P(x(t)|\mathcal{H}_1)}{P(x(t)|\mathcal{H}_0)} \geq \lambda_0, \tag{5.23}$$

where the detection criteria λ_0 is a false alarm probabilty chosen by the experimenter. The probability of a given signal in Gaussian noise is

$$p_n[x(t)] \propto e^{-(x|x)/2}, \tag{5.24}$$

where for two functions of frequency $a(f)$ and $b(f)$, $(a|b)$ the noise-weighted inner product is given by

$$(a|b) \equiv 4\Re \int_0^\infty \frac{\tilde{a}(f)\tilde{b}^*(f)}{S(f)} df, \tag{5.25}$$

with $S(f)$ the one-sided power spectral density [56]. The probability of the null hypothesis is the probability that the observed signal is drawn from noise alone, $p_n[x(t)]$. The probability of the alternate hypothesis is the probability that the signal is composed of a noise and a signal component, or, that the noise drawn from the Gaussian probability distribution is equal to $x(t) - h(t)$ giving probability $p_n[x(t) - h(t)]$. Inserting the proportionality relation given in equation 5.24 into the likelihood ratio in equation 5.23, then taking the logarithm, gives the log-likelihood

$$\ln \Lambda = (x|h) - \frac{1}{2}(h|h). \tag{5.26}$$

The $(x|h)$ term is also known as the matched filter, a noise-weighted correlation of the observed signal $x(t)$ to an assumed gravitational wave signal $h(t)$. The matched filter is an optimal test statistic for the detection of gravitational waves in interferometer noise.

If all parameters of the gravitational wave signal $h(t)$ are known, the log-likelihood has a single value that is compared to the detection threshhold λ_0. However, in real observations, the signal parameters are not completely known, and the log-likelihood is used as a maximum likelihood estimator, marginalized over the unknown parameters to determine the maximum likelihood.

For the case of a rotating neutron star, the $\mathcal{F}$-statistic, derived by Jaranowski, Krolak, and Schutz [88], is an analytic maximization of the log-likelihood over the unknown parameters $\mathcal{A} \equiv \{A_+, A_x, \psi, \phi_0\}$, where

$$A_+ = \frac{1}{2}h_0(1+\cos^2\iota) \tag{5.27}$$

$$A_\times = h_0\cos\iota, \tag{5.28}$$

accounting for uncertainties in signal amplitude h_0, neutron star inclination angle ι, gravitational wave polarization angle ψ, and inital phase ϕ_0. The $\mathcal{F}$-statistic is defined by dividing the signal $h(t;\lambda)$, where $\lambda \equiv \{f^{(x)}, \hat{n}\}$, into four basis waveforms

$$h_1(t;\lambda) = a(t,\hat{n})\cos\phi(t;\lambda) \tag{5.29}$$

$$h_2(t;\lambda) = b(t,\hat{n})\cos\phi(t;\lambda) \tag{5.30}$$

$$h_3(t;\lambda) = a(t,\hat{n})\sin\phi(t;\lambda) \tag{5.31}$$

$$h_4(t;\lambda) = b(t,\hat{n})\sin\phi(t;\lambda) \tag{5.32}$$

where $a(t,\hat{n})$ and $b(t,\hat{n})$ are the amplitude modulation functions defined in [136], and dividing $\mathcal{A}$ into four amplitude vectors

$$\begin{aligned}
\mathcal{A}^1 &= A_+ \cos\phi_0 \cos 2\Psi - A_\times \sin\phi_0 \sin 2\Psi && (5.33)\\
\mathcal{A}^2 &= A_+ \cos\phi_0 \sin 2\Psi + A_\times \sin\phi_0 \cos 2\Psi && (5.34)\\
\mathcal{A}^3 &= -A_+ \sin\phi_0 \cos 2\Psi - A_\times \cos\phi_0 \sin 2\Psi && (5.35)\\
\mathcal{A}^4 &= -A_+ \sin\phi_0 \sin 2\Psi + A_\times \cos\phi_0 \cos 2\Psi && (5.36)
\end{aligned}$$

such that $h(t;\mathcal{A},\lambda)$ is expressed, with implicit summation,

$$h(t;\mathcal{A},\lambda) = \mathcal{A}^\mu h_\mu(t;\lambda). \tag{5.37}$$

In this basis, the log-likelihood function can be rewritten as

$$\ln\Lambda(x;\mathcal{A},\lambda) = \mathcal{A}^\mu x_\mu - \frac{1}{2}\mathcal{A}^\mu \mathcal{A}^\nu M_{\mu\nu} \tag{5.38}$$

where $x_\mu \equiv (x|h_\mu)$ and $M_{\mu\nu} \equiv (h_\mu|h_\nu)$. The maximum likelihood estimators for each of $\mathcal{A}^\mu$ are determined from

$$\frac{\partial \ln\Lambda}{\partial \mathcal{A}^\mu} = 0, \tag{5.39}$$

giving maximum likelihood estimators of

$$A^\mu_{\mathrm{ML}} = M^{\mu\nu} x_\nu \tag{5.40}$$

Substituting these back into the matched filter gives the $\mathcal{F}$-statistic,

$$2\mathcal{F}(x;\lambda) = x_\mu M^{\mu\nu} x_\nu. \tag{5.41}$$

For a perfectly matched signal $h(t;\lambda)$, the expectation value of the $\mathcal{F}$-statistic is

$$E(2\mathcal{F}) = 4 + \rho^2, \tag{5.42}$$

where ρ is the signal-to-noise ratio (SNR), $\rho = \sqrt{(h|h)}$ [137][87]. The $\mathcal{F}$-statistic is a χ^2 distribution with four degrees of freedom and a non-centrality parameter ρ^2 determined by the SNR of the gravitational wave signal. In the case of data with only noise, the probability distribution reduces to a central χ^2 distribution with four degrees of freedom, with probability density function

$$P(2\mathcal{F};0) = \frac{1}{2}\mathcal{F}e^{-\mathcal{F}}, \tag{5.43}$$

giving a false alarm rate for a given threshhold $2\mathcal{F}^*$ of

$$f_A(2\mathcal{F}^*) = (1+\mathcal{F}^*)e^{-\mathcal{F}^*}. \tag{5.44}$$

The frequentist upper limit with confidence C set by the values of the $\mathcal{F}$-statistic is the signal amplitude h_0^C such that a fraction C of trials is greater than the measured $\mathcal{F}$-statistic $\mathcal{F}_0$, defined as

$$C = \int\limits_{2\mathcal{F}_0}^{\infty} P(2\mathcal{F}|h_0^c)d2\mathcal{F}. \tag{5.45}$$

The upper limits of confidence are calculated by Monte Carlo integration. As frequentist upper limits, they do not express a confidence that the true strain is contained in the interval $[0, h_0^C]$, but rather state the rate which a signal would be contained in the interval in an infinite number of experiments [137].

5.2.3 Continuous Wave Search Modalities

After deriving a detection statistic for continuous gravitational waves, the next step is to apply the statistic to the analysis of detector data. For continuous gravitational waves, the analysis will be computationally limited. For a coherent search, the SNR of a putative signal will increase as the square root of coherence time, $T_{\mathrm{coh}}^{1/2}$. The requirement of templating to avoid unacceptable mismatch between the signal and its matched filter causes computation time to scale as a high power of T_{coh}. Increased knowledge about the object's location and spin characteristics reduces the computational requirements of templating and allows for deeper searches. Optimization based on knowledge of source characteristics splits continuous gravitational wave searches into three types: targeted searches for well-characterized sources, directed searches for partially characterized sources, and all-sky searches for unknown sources.

5.2.3.1 Targeted Searches

Of the $\sim$2500 pulsars already discovered, 578 have spin frequencies of 5 Hz or greater [112][113]. Gravitational wave emission from these pulsars will lie in the aLIGO frequency band, above the seismic wall at 10 Hz [6]. For these known pulsars, electromagnetic observations provide information about the pulsar's sky position and ephemeris. This knowledge of position and frequency greatly reduces the parameter space a gravitational wave search needs to cover, allowing long coherence times to be used to set strong upper limits on pulsar emissions.

Targeted searches seek to detect or set upper limits on the gravitational wave emission from known neutron stars. One important figure of merit is the spindown limit defined in equation 2.56,

$$
\begin{aligned}
h_{spindown} &= \frac{1}{d}\sqrt{\frac{-5G}{4c^3} I_{zz} \frac{\dot{f}_{GW}}{f_{GW}}} && (5.46)\\
&= (2.5 \times 10^{-25}) \left(\frac{1\ \mathrm{kpc}}{d}\right) \sqrt{\left(\frac{1\ \mathrm{kHz}}{f_{GW}}\right)\left(\frac{-\dot{f}_{GW}}{10^{-10}\ \mathrm{Hz/s}}\right)\left(\frac{I_{zz}}{I_0}\right)}. && (5.47)
\end{aligned}
$$

This spindown limit is defined as the gravitational wave strain that would be caused by the observed energy loss from the pulsar. “Beating the spindown limit” by measuring a gravitational wave strain upper limit below the spindown limit gives information about the maximum fraction of energy loss due to gravitational waves. As this equation relies on conservation of energy, it assumes a negative value for the frequency derivative. Positive values of frequency derivative can occur due to accretion from binary partners or accelerations in globular cluster cores, and have been observed in 35 pulsars [112][113].

Of the 195 pulsars investigated in the initial detector era data, the spindown limit has been beaten for only the Crab and Vela pulsars. As stated in Chapter 2, the gravitational wave emission from the Crab pulsar is limited to $\lesssim 1\%$ of the observed energy loss, while the gravitational wave emission from the Vela pulsar is limited to $\lesssim 10\%$ of the observed energy loss [6]. This is a non-trivial statement, as the dissipation of rotational energy in radio pulsars is as much as 10^5 times greater than the observed radio luminosity [102]. This allows statements to be made about the physical properties of the pulsars, limiting the magnetic field of the Crab to $B \lesssim 10^{16}$ G and constraining models of neutron star structure.

5.2.3.2 Directed Searches

Directed searches include searches for objects with known locations but no observed pulsations, such as the Cassiopeia A supernova remnant, and searches for unknown objects at interesting sky locations, such as the direction of the Galactic center. Although the sky position and Doppler modulation of the search target is known, the unknown frequency and spindown values increase the parameter space from a targeted search.

Directed searches for non-pulsing supernova remnants have covered nine objects, including Cassiopeia A (Cas A). Cas A is the youngest known neutron star with a birth date of 1681 ± 19 CE, located at a distance of $3.4^{+0.3}_{-0.1}$ kpc [10]. Cas A has been searched for gravitational waves at frequencies ranging from 91-573 Hz, with spindown derivatives given by an assumed age of 300 yr, setting a strain upper limit of 6×10^{-25}. The lowest strain upper limit set for a supernova remnant in a directed search is 4.2×10^{-25}, for G291.0-0.1 [7].

Directed searches have also been performed for sky positions with assumed overdensities of potential gravitational wave emitters. One such position is the direction of the Galactic center. Although very few neutron stars have been observed in the Galactic center, the high star formation rate and large number of stars with initial mass 100 $M_\odot$ or higher suggest a high rate of neutron star formation. A semi-coherent directed search from 78-496 Hz in frequency and from -7.8×10^{-8} - 0 Hz/s in first spindown derivative has been performed on the galactic center, setting upper limits as low as 3.35×10^{-25} at 150 Hz [1]. A similar search has been performed on the Orion spur, a grouping of stars connecting the Perseus and Sagittarius arms of the Galaxy that contains many star-forming regions. For a search from 50-1500 Hz, -5×10^{-9} - 0 Hz/s, upper limits were set as low as 6.3×10^{-25} near 169 Hz [9].

The search for Cassiopeia A and other non-pulsating supernova remnants was performed using a fully coherent $\mathcal{F}$-statistic method. For a search over frequency and the first two spindown derivatives, the computational time scales as T_{coh}^7 [169]. The Galactic center and Orion spur searches used semicoherent methods. Although the SNR improves as $T^{1/4}$ for the semicoherent methods, they have better sensitivity for a given computing time, assuming a long signal stretch with consistent sensitivity is available. It is expected that semicoherent methods will supplant coherent methods for directed searches in the future. However, during the early days of aLIGO sensitivity will be constantly improving, and coherent methods will be preferred for analyzing short, sensitive data segments [107]. The search for Fermi unassociated sources discussed in Chapter VI uses a fully coherent directed search method.

5.2.3.3 All-Sky Searches

All-sky gravitational wave searches look for unknown spinning neutron stars in the Galaxy. There is good reason to believe that there are electromagnetically quiet neutron stars nearby. Population synthesis models estimate that there are $O(10^6$-$10^7)$ neutron stars within 5 kpc, with less than 0.0001% of these observed so far [106]. Given the observation of a neutron star spinning at 716 Hz [85], these searches need to cover frequencies from the seismic floor of 10 Hz up to 2 kHz, with a spindown range -10^{-8} - 10^{-9} Hz/s to account for models of frequency evolution ranging from spindown due to frequency loss to spinup in a long-period binary system. With the added uncertainty of unknown sky position, the computational cost for a coherent search scales, in principle, as T_{coh}^7. For this reason, semi-coherent methods are preferred for all-sky searches. In a semi-coherent search, small data stretches of a few hours to a day in length are searched coherently, then added together. Although the SNR experiences some degradation due to imperfect tracking of phase, the computational cost decreases significantly, to $\sim T_{\mathrm{search}} \times T_{\mathrm{segment}}^5$ [43].

All-sky searches for gravitational waves have been performed by two classes of pipelines: relatively quick and self-contained pipelines including PowerFlux and Frequency Hough, and the deeper Einstein@Home search powered by a volunteer distributed computing network. The best upper limits set by the quick pipelines so far have been from the Hough pipeline, with a limit of 8.9×10^{-25} in a frequency band from 146.5-146.75 Hz [4], and from the PowerFlux pipeline, with a limit of 3.6×10^{-25}

in a frequency band of 153.5-153.75 Hz for a circularly polarized signal [12]. The best limit set by Einstein@Home is 7.6×10^{-25} in a band around 152.5 Hz [2], but at a computational cost more than two orders of magnitude higher than for the Hough search [4]. The plan for future all-sky searches is to maintain multiple quick pipelines for rapid analysis of data, with verification of results from alternate pipelines and Einstein@Home [106].

5.3 Electromagnetic Emission from Neutron Stars

The goal of gravitational wave multimessenger astronomy is to use data from gravitational wave detectors and electromagnetic telescopes to explore high-energy phenomena in the universe. To discuss neutron star detection from a multimessenger perspective, the electromagnetic emission from neutron stars must be considered along with the gravitational wave emission. During the neutron star collapse process, conservation of magnetic flux concentrates the stellar magnetic field of 100 G to approximately 10^{12} G. This powerful magnetic field contains a high-energy plasma magnetosphere, co-rotating with the neutron star to a radius of $r_C = c/\omega_{\mathrm{rot}}$. At this light cylinder radius where the plasma would co-rotate at the speed of light, the magnetic field lines open. At the boundary between the closed and open regions, there is a strong electric field with available potential of $10^{14} - 10^{15}$ V [110], producing two distinct emission regions: the polar cap and the outer gap (Figure 5.1).

The polar cap lies directly above the magnetic axis, and is thought to be the primary source of radio emission from neutron stars [50]. Although pulsars were first observed in radio, the emission mechanism for radio waves is not well understood. The emission is coherent, implying possible origins in electron bunching or resonances in the magnetospheric plasma [110].

The outer gap lies between the last closed and first open field line, and is associated with gamma-ray radiation from pulsars. There is no evidence of coherence in

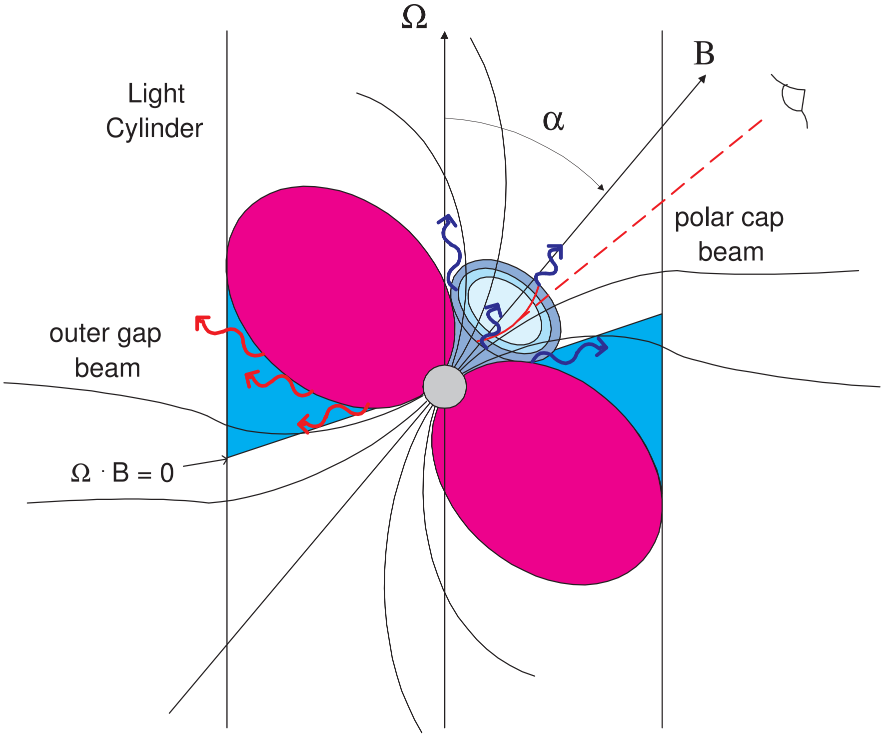

Figure 5.1: Polar cap and outer gap model of pulsar emission. The pulsar magnetic field (B) contains a high energy plasma magnetosphere (magenta). At the light cylinder radius, where the velocity of corotation with the neutron star equals the speed of light, the magnetic field lines open. The blue outer gap region is the primary source of gamma-ray emission, while the gray polar cap region is the primary source of radio emission. Image credit A.K. Harding (NASA/GSFC), courtesy of the Compton Gamma Ray Observatory Science Support Center [80].

gamma-ray emission, suggesting that radio and gamma emissions come from different mechanisms. Gamma radiation from the outer gap is primarily due to curvature radiation. Electrons and positrons from the pair-production plasma are constrained to closely follow a particular field line on a path with curvature ρ at relativistic velocities. The radiation from this process is similar to synchrotron radiation with curvature $c/2\pi\rho$, peaking at a critical frequency of

$$\nu_c = \frac{3c}{4\pi\rho\gamma^3}, \tag{5.48}$$

where γ is the relativistic factor $(1 - \frac{v}{c})^{-1}$. As a consequence of the method of production, gamma radiation is produced in a cone around the outer gap, crossing the field of view of an observer in "sheets" and resulting in the double pulse profile characteristic of gamma ray pulsars.

The localized emission from both gamma and radio sources has consequences for observations of pulsars in the galaxy. The finite size of the radio pulsar emission beam is a primary contributor to the low fraction of pulsars observed, with an observable fraction estimated at 10-20% depending on the precise physics and geometry of the beaming process [103]. The different emission processes and locations result in radio and gamma ray emission at different angles from the axis of rotation. Consequently, pulsars that are invisible to radio telescopes can be observed in gamma-rays, and some radio pulsars have eluded detection by gamma-ray telescopes. Objects that emit in a given frequency band are said to be "loud" in that band, while objects that do not emit are said to be "quiet".

5.4 The Fermi Large Area Telescope and its Catalog

5.4.1 The Fermi Large Area Telescope

The Fermi satellite is a gamma-ray space telescope that was launched in 2008. Two separate instruments are located on the satellite; the Gamma-Ray Burst Monitor for detection of gamma-ray transients, and the Fermi Large Area Telescope (LAT) for full-sky surveys [36]. The mission of the LAT is to continue the exploration of the gamma-ray sky begun by earlier satellites, including studying particle acceleration mechanisms in celestial sources, characterizing the properties of gamma-ray bursts, and probing possible signals of dark matter interactions in the galaxy [36].

Because gamma-rays can be neither reflected nor refracted, the LAT is a pair-production telescope, measuring the properties of electron and positron tracks resulting from the pair conversion of gamma rays in a thin, high-impedance foil. Thirty-six silicon strip trackers are placed around sixteen layers of tungsten foil to detect the particle shower tracks. A CsI calorimeter measures the energy of the shower to determine the incident photon energy, and an anti-coincidence detector excludes noise from cosmic rays. The instrument is sensitive to gamma rays with energies ranging from 20 MeV to over 300 GeV, with a per-photon angular resolution of

$$\theta = 0.8^\circ \left(\frac{E}{1\ \mathrm{GeV}} \right)^{-0.8}, \tag{5.49}$$

reaching a limit of 0.2° at 20 GeV [36]. The telescope operates in a full-sky scanning mode, covering the full sky every three hours, with a duty fraction of $\sim 76\%$ [23].

5.4.2 Catalog Construction

The raw data gathered by the Fermi satellite is released to the public through the Fermi Science Support Center (FSSC) [164]. The collaboration also releases catalogs of detected sources, the most recent of which is the Third Fermi Large Area Telescope

Source Catalog (3FGL), incorporating results from four years of Fermi data [23].

Determination of a point source in the Fermi catalog is performed using maximum likelihood methods. For each of 1728 25-deg^2 tiles, the photon data is fit to possible source locations. These sources are localized by maximizing the likelihood of source position given the observed photon distribution. The uncertainty ellipse on a source is required to have a semimajor axis of less than $0.25°$. By comparing the localization of bright gamma ray sources with their known positions from other wavelengths, the absolute precision on these measurements was determined to be $\sim 0.005°$ [23].

5.4.3 Pulsar Discovery

Of the 3033 sources in the 3FGL catalog, 2038 have an associated astronomical object. The remaining 992 are localized emitters of gamma rays with no association. These unknown sources are of significant interest for pulsar discovery. Unidentified galactic sources of gamma radiation are estimated to be $\sim 47\%$ pulsars and $\sim 44\%$ supernova remnants [23].

Pulsar discoveries have been made through blind searches of photon arrival data. Searches for pulsars in gamma-ray data have similar constraints to searches for continuous gravitational waves. The low luminosity of gamma ray pulsars necessitates long observation times, and correspondingly long discrete Fourier transforms to extract the pulse frequency. Non-negligible spindown derivatives must be taken into account, requiring many discrete Fourier transforms at every parameter point. As with continuous gravitational wave searches, the number of searches required to account for spindown values grows with frequency, and consequently gamma-ray pulsars detections have been biased towards slow-rotating pulsars. Furthermore, gamma-ray sources are poorly localized, and large regions of the sky must be considered to detect pulsars.

The Fermi collaboration developed a method based on the Fourier transform of the differences of photon arrival times to search for gamma-ray pulsations in radio-quiet pulsars [35]. Each photon arrival time is corrected based on an assumed pair of frequency and spindown, such that

$$t'_i = t_i + \frac{1}{2}\frac{\dot{f}}{f_0}t_i^2. \tag{5.50}$$

The differences in arrival times are then searched for candidate pairs of frequency and spindown using a data-folding algorithm. Using this method, the Fermi collaboration discovered twenty-six new pulsars in gamma-ray data, with frequencies ranging from 2.4 to 20.8 Hz [17] [66].

The Einstein@Home team adapted the semi-coherent framework used for the Einstein@Home all-sky gravitational wave pipeline to search for Fermi gamma-ray pulsars. The E@H method incoherently sums the results of several year of coherent searches of data stretches of several days, analogously to the semi-coherent methods used for all-sky gravitational wave searches. For each data stretch, the coherent power is constructed from the Fourier transform of the time differences of photon arrival. These coherent powers are incoherently combined to produce a test statistic. Incorporating previous experience with optimization of continuous gravitational wave search code, this method improves upon the time-differencing method in its optimal gridding of parameter space, hierarchical search procedure, and incorporation of spindown in a way that allows for highly efficient heterodyning methods [133]. This method has found fifteen additional gamma-ray pulsars [133][134], including the binary millisecond pulsar J1311-3430, the fastest-spinning pulsar discovered in a gamma-ray blind search with a spin frequency of 390 Hz [65], and the obscured young radio-quiet pulsar J1906+0722, the most significant unidentified source in both the 2FGL and 3FGL catalogs [54].

Another successful approach to pulsar discovery in Fermi data has been searching for radio pulsations from unassociated sources. For pulsars identified in blind searches, radio observations can determine source distance, gamma-ray luminosity, and pulsar geometry, including the angle between the spin and magnetic axes α and the inclination angle ι. For unassociated sources, a radio detection provides a refined source location and ephemeris, reducing the computational cost of searching gamma-ray data for pulsations. Fermi source localization is sufficiently precise to allow the partner radio telescopes in the Fermi Pulsar Search Consortium to search an unassociated source location for radio pulsations with a single pointing [143]. Thirty-eight pulsars have been discovered in radio searches of gamma-ray telescopes. Although these pulsars could have been discovered in radio data alone, they are radio-faint, and the pointing information from Fermi accelerated their discovery by decades [143]. Radio and gamma-ray observations are complementary; information from one wavelength makes detection of a new source in the other wavelength easier.

5.5 The Potential of Gravitational Waves for Pulsar Discovery

As with any population of pulsars, the discovered population of gamma-loud pulsars is biased. Blind searches are less sensitive to fast-spinning pulsars and pulsars in binaries; high frequency and spindown derivative requires large numbers of searches to cover the parameter space, and the modulation of signals by binary orbits degrades the signal quality. Radio observations have been useful for gamma-loud pulsar discovery, but pulsars are not expected to be universally observable in both gamma rays and radio waves because of pulsar emission geometry.

Continuous gravitational wave observations can be complementary to gamma-ray observations for pulsar discovery. Gamma-ray data can assist with known difficulties in blind continuous gravitational wave searches. An unassociated gamma-ray source can provide a sky location and a level of confidence that the emission originates from a pulsar. Using Fermi unassociated sources as targets for a directed search, similar to the Cas A search discussed in section 5.2.3.2, can help mitigate the low expected strain and high computational cost of a blind search and drive multiwavelength pulsar discovery incorporating gravitational wave data.

Gravitational wave data can also provide information for detection of pulsations in gamma-ray data. Gamma-ray pulsar discovery is limited by low photon numbers, signal dependence on pulsar magnetic field axis and inclination angle, high increase of computational cost with increasing frequency and spindown derivatives, and confounding signals from other gamma-ray sources. Although gravitational wave amplitudes will be small, the signals will be continuous. Inclination angle effects the amplitude of the signal, as shown in equation 5.11, but there is no inclination angle for which gravitational wave signals vanish. Additionally, gravitational wave searches are not affected by confounding gamma-ray emission from pulsar wind nebulae and dust clouds, which will not have associated gravitational wave emission. Continuous gravitational wave methods have been developed and refined to account for the increasing template count required for high-frequency, high-spindown searches. The success of the methods developed by the Einstein@Home team suggests that the techniques used for continuous gravitational wave searches have application in blind gamma-ray searches; gravitational wave observations may contribute as well.

CHAPTER VI

A Pilot Search for Gravitational Waves from Fermi Unassociated Sources

6.1 Motivation

This chapter describes a pilot search for continuous gravitational waves from unassociated sources detected by the Fermi gamma-ray satellite, developed to investigate the scientific potential of joint Fermi and LIGO observations of radio-quiet pulsar candidates. This study uses a fully coherent directed search strategy in data from the sixth science run of Initial LIGO, anticipating the conditions of the first aLIGO science run (O1). The mature fully-coherent F-statistic methods used for this search were previously used in directed searches for Cassiopeia A [10] [169], non-pulsing supernova remnants [7], and unknown objects in the globular cluster NGC6544 [52].

As discussed in the previous chapter, discovering gamma-loud pulsars involves intensive computation and collaboration with radio and X-ray astronomers. Even bright sources can evade classification for years because of confusion between the pulsar and another nearby source [54]. Therefore, a LIGO search designed for pulsar discovery has potential applications for Fermi classification and gravitational wave science. No known radio-quiet pulsar is spindown-accessible in S6 data, and previous LIGO observations have not been able to set limits on the physical properties of this interesting class of pulsars. The discovery of a pulsar emitting in gamma rays and gravitational waves could make major contributions to our understanding of the neutron star equation of state.

This chapter contains preliminary observational results that have not been reviewed by the LIGO-Virgo Scientific Collaboration.

6.2 Search Design

6.2.1 Analysis Method

As discussed in the previous chapter, matched filtering is the optimal method for continuous gravitational wave searches. This investigation uses the multi-interferometer $\mathcal{F}$-statistic [58], a generalization of the $\mathcal{F}$-statistic presented in section 5.2.2 to a network of interferometers. Under the assumption that interferometer noise is uncorrelated, the multi-interferometer $\mathcal{F}$-statistic modifies the definition of the noise-weighted inner product (Equation 5.25) to the sum of the noise-weighted inner products of the individual interferometers,

$$(a|b) \equiv 2 \sum_{\alpha} \Re \int_{0}^{\infty} \frac{\tilde{a}_{\alpha}(f)\tilde{b}^{*}_{\alpha}(f)}{S_{\alpha}(f)} df, \tag{6.1}$$

where α is an interferometer number index. This implementation is computationally fast and nearly optimal; a Bayesian modification has been shown to be more optimal by the Neyman-Pearson criterion discussed in the previous chapter [138], but has not reached widespread implementation.

This search uses a standard implementation of the multi-interferometer F-statistic in the publicly available LALSuite [105] package, `lalapps_ComputeFStatistic_v2`. This code has been reviewed by the LIGO collaboration and used in the supernova remnant and globular cluster searches. The input to this routine is a Short Fourier Transform (SFT). SFTs are produced by splitting the time-domain interferometer output into stretches of length $T_{SFT} = 1800$ s, applying a band-pass filter from 40-2035 Hz, and Tukey windowing in the time domain before performing a Fourier transform of the data. This search also incorporates barycentric resampling, where the time-domain data is transformed to the SSB prior to the Fourier transform. Incorporating barycentric resampling speeds up the search, as a single Fast Fourier Transform (FFT) can be used to calculate the detection statistic for arbitrary frequency and coherence times [131].

In practical implementation, a matched filter can never be truly matched, as an infinitely fine grid of frequency and frequency derivative parameters $\lambda_f \equiv \{f^{(x)}\}$ would require infinite computation time. Defining a template grid requires the specification of some acceptable degree of mismatch, fractional loss in SNR due to an offset from true parameters $\Delta\lambda$,

$$m(\Delta\lambda) = \frac{2\mathcal{F}(0) - 2\mathcal{F}(\Delta\lambda)}{2\mathcal{F}(0)}. \tag{6.2}$$

Searches targeting young objects ($\tau < 1$ kyr) require the consideration of at least three frequency parameters, $\{f, \dot{f}, \ddot{f}\}$. This search uses the spin-square templating routine incorporated into `lalapps_ComputeFStatistic_v2`, which places templates on a body-centered cubic lattice [169]. For a given coherence time $T_{\rm coh}$ and maximum allowable mismatch M, the template spacings are given by

$$df = \frac{2\sqrt{3M}}{\pi T_{\rm coh}} \qquad d\dot{f} = \frac{12\sqrt{5M}}{\pi T_{\rm coh}^2} \qquad d\ddot{f} = \frac{20\sqrt{7M}}{\pi T_{\rm coh}^3}. \tag{6.3}$$

Consequently, the computational cost of a fully coherent search over three frequency parameters $N_{\rm comp}$ can scale as high as the seventh power of coherence time $T_{\rm coh}^7$, while the sensitivity of the search scales as $T_{\rm coh}^{1/2}$. Fully coherent searches for continuous gravitational waves are computationally limited, requiring optimization of coherence time $T_{\rm coh}$ given the search parameters $\{f, \dot{f}, \ddot{f}\}$.

6.2.2 Parameter Selection

The frequency parameters of a pulsar, or the ephemeris, are determined by physical processes. A pulsar is born spinning, and the emission of energy in electromagnetic and gravitational waves causes the spin frequency to decrease. The energy loss is parameterized by the braking index n,

$$n = \frac{f\ddot{f}}{\dot{f}^2}, \tag{6.4}$$

which is derived from the differentiation of an assumed power law relation between frequency and spindown (first frequency derivative),

$$\dot{f} = -Kf^n, \tag{6.5}$$

where K is assumed to be constant.

Although predictions have been made for the braking index that would be observed for energy loss due to dipole radiation ($n = 3$) and gravitational wave emission (n=5), the braking index is an observationally determined parameter. Observations of braking indices range from 0.9 to 2.8 [79], suggesting that the spindown of pulsars is not due to a single energy loss mechanism. For this investigation, a conservative range of $2 \leq n \leq 7$ was chosen. Although braking indices above 2.8 have not been observed in electromagnetic radiation, widening the considered range maintains search sensitivity to unusual objects, such as gravitars, neutron stars primarily emitting in gravitational waves.

The age of a pulsar can be estimated from its ephemeris by integrating the spindown power law of equation 6.5. Assuming the spin frequency at birth was much greater than the current spin frequency, the spindown age τ is

$$\tau \simeq \frac{1}{n-1}\left(\frac{f}{-\dot{f}}\right). \tag{6.6}$$

The spindown age is distinct from the chronological age of a pulsar. Due to the assumption that the initial spin frequency is much larger than the current spin frequency, the spindown age greatly underestimates the age of pulsars that have undergone accretion processes. The minimum spindown age considered in this search is $\tau = 300$ years, selected for historical reasons. The search is sensitive to Galactic neutron stars, and it is unlikely that a nearby Galactic supernova went unrecorded in the modern era.

The spindown age sets an upper limit on the potential gravitational wave strain from a given neutron star, found by simple substitution of the spindown age in Equation 6.6 into the spindown limit (equation 2.56),

$$h_{\mathrm{age}} = \frac{1}{d}\sqrt{\frac{5GI_{zz}}{4(n-1)\tau}}. \tag{6.7}$$

The strain sensitivity of a gravitational wave search must improve upon this age-based limit to make meaningful statements about a candidate source.

The search ranges for the first and second frequency derivatives can be derived from the definitions of braking index and spindown age. Starting with the definition of spindown age (Equation 6.6), the first frequency derivative for some assumed frequency f will be

$$\dot{f} = -\frac{1}{n-1}\frac{f}{\tau}. \tag{6.8}$$

Rearranging the definition of braking index (Equation 6.5), the second frequency derivative at the assumed frequency is

$$\ddot{f} = \frac{n\dot{f}^2}{f} = \frac{n}{(n-1)^2}\frac{f}{\tau^2}. \tag{6.9}$$

For our assumed braking index range of $2 \leq n \leq 7$, this defines the parameter spaces for $\dot{f}$ as

$$-\frac{f}{\tau} \leq \dot{f} \leq -\frac{f}{6\tau} \tag{6.10}$$

and for $\ddot{f}$ as

$$\frac{7}{36}\frac{f}{\tau^2} \leq \ddot{f} \leq \frac{2f}{\tau^2}. \tag{6.11}$$

The computational cost of a search depends on the number of templates, set by this $\{f, \dot{f}, \ddot{f}\}$ parameter space. The coherence time used for the search is set with the goal of fitting this template bank into the computing time available. As this search aims to cover a large number of candidate sources, the coherence time is further restricted to allow the consideration of multiple potential sources.

The coherence time cannot be arbitarily decreased; the search must improve on the results of the Einstein@Home all-sky search. Due to the immense computing power of the Einstein@Home distributed computing network, the sensitivity for its all-sky search is comparable to that of a directed search with a short coherence time. Although this directed search incorporates more ephemeris parameter space than Einstein@Home, including the second frequency derivative and assuming a lower bound on spindown age of $\tau = 300$ years rather than the $\tau = 700$ years assumed by Einstein@Home [2], the coherence time must be such that the sensitivity surpasses the age-based spindown limit while still being comparable to the sensitivity of the Einstein@Home results, while keeping the search within computational constraints.

To predict the sensitivity for a given coherence time, the noise power spectral density, harmonically averaged over H1 and L1 for the duration of S6, was scaled by T_{coh},

$$\tilde{h}(f) = \Theta \frac{\bar{S}_{\mathrm{S6}}(f)}{\sqrt{T_{\mathrm{coh}}}}, \tag{6.12}$$

where Θ is a sensitivity factor incorporating the trials factor, approximately 35 for a

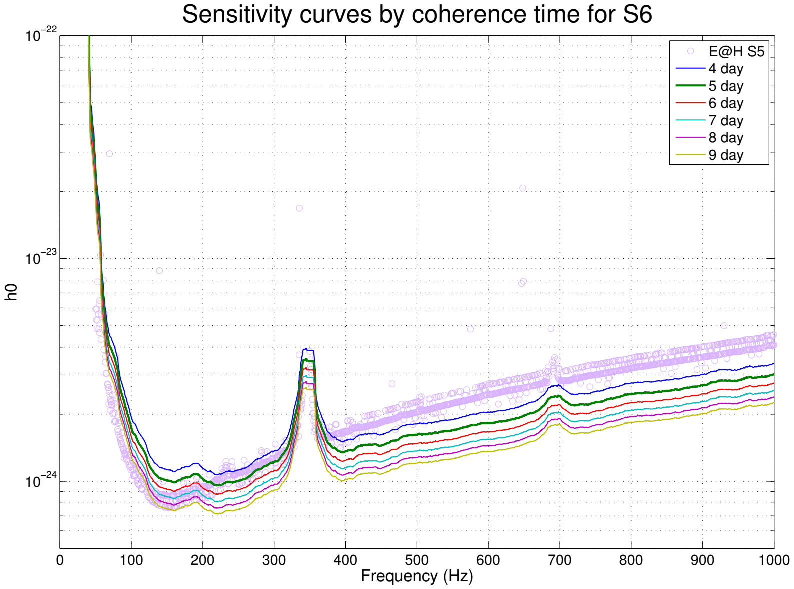

Figure 6.1: Comparison of search sensitivity with variation of coherence time. The S6 sensitivity curve was scaled as in equation 6.12, using coherence times ranging from 4 to 9 days, and comparing to the results from the Einstein@Home S5 all-sky search (lavender circles) [2]. A coherence time of 5 days (bold green curve) was chosen to compromise between limiting computation time while having competitive sensitivity with Einstein@Home at low frequencies.

directed search [169]. Figure 6.1 shows the S6 sensitivity curve scaled by coherence times ranging from four to nine days and superimposed upon the results from the Einstein@Home S5 all-sky search [2]. Due to improved interferometer noise at high frequencies, all coherence times have better sensitivity at frequencies greater than 400 Hz. In the most sensitive frequencies between 100 and 300 Hz, a four-day coherence time does not reach the S5 Einstein@Home limits. A five-day coherence time compares favorably to the Einstein@Home results in the 200-300 Hz region, and careful selection of sensitive data gives better overall sensitivity in the 100-200 Hz region. To allow for a lightweight search covering a large number of sources, a five-day coherence time was chosen for this search. As the computation time scales as T_{coh}^7, moving to a six-day coherence time would increase the computation cost by a factor of 3.5, while moving to a nine-day coherence time would increase the cost by a factor of more than 60. The five-day coherence time allows for scientifically interesting levels of sensitivity while investigating the maximum number of sources for a given computing cost.

During the course of observations, the noise spectral density of the interferometer output decreases as improvements are made to the interferometer, noise sources are mitigated, and control schemes are refined. The livetime of each interferometer varies over time because of seasonal variances in environmental and anthropogenic noise. Choosing a particularly sensitive stretch of data for analysis maximizes the sensitivity of a fully coherent search. A noise sensitivity figure of merit can be defined as

$$F_{sens} = \sum_{n,f,t} \frac{1}{S_n(f,t)}, \tag{6.13}$$

where $S_n(f,t)$ is the noise power spectral density for SFT n, and the sum is taken over all SFTs in a time stretch of interest; the greater the detector uptime, the larger the number of SFTs [10].

The LIGO S6 science run took place between July 7 2009 21:00:00 UTC (GPS 931035615) and October 21 2010 00:00:00 UTC (GPS 971654415). As previous S6

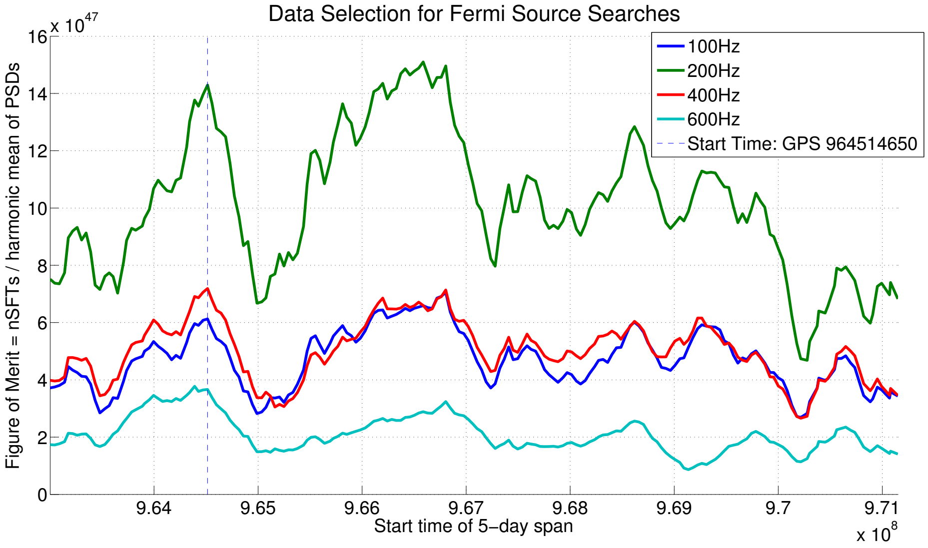

Figure 6.2: The modified figure of merit from equation 6.14 for five-day spans with start times spaced every 6 hours between July 12 2010 20:21:44 UTC (GPS 963001319) and October 20 2010 03:37:22 UTC (GPS 971581057). The peak in sensitivity figure of merit was used to select the data stretch from July 30 2010 08:43:55 UTC (GPS 964514650) to August 4 2010 08:43:55 UTC (GPS 964946650).

coherent directed searches found their most sensitive stretches in the last four months of S6 [7][52], the data for this search was selected from the period between July 12 2010 20:21:44 UTC (GPS 963001319) and October 20 2010 03:37:22 UTC (GPS 971581057). For five-day segments with start times every six hours through this span, a modified equivalent figure of merit,

$$F_{sens}(f_{\text{test}}, \Delta t) = \frac{N_{\text{SFTs}}}{\bar{S}(f_{\text{test}}, \Delta t)}, \tag{6.14}$$

was calculated at four test frequencies, $f_{\text{test}} = \{100, 200, 400, 600\}$ Hz. The resulting time-based figures of merit, shown in Figure 6.2, were used to select a data stretch from July 30 2010 08:43:55 UTC (GPS 964514650) to August 4 2010 08:43:55 UTC (GPS 964946650).

6.3 Source Selection

In the initial version of the Fermi 3FGL catalog, publicly available through the Fermi Science Support Center as `gll_psc_v14.fit` [164], there are 1009 unassociated sources. Due to the computational restrictions on gravitational wave searches, a subset of sources was selected for analysis.

Gravitational wave strain h is inversely proportional to distance d, and minimizing source distance improves the detection probability. Measuring the distance to a gamma-ray pulsar is a non-trivial process. Accurate distance measurements through parallax are possible for nearby sources, within 500 pc. Most distances are measured by the radio dispersion measure, by X-ray flux determination, or by an estimate based on gamma-ray luminosity distance,

$$L_\gamma = f_\Omega (4\pi D^2) G_\gamma, \tag{6.15}$$

where G_γ is the measured Fermi flux and f_Ω is a source-specific flux correction factor [74]. As the ability to make a distance estimate varies with source conditions, the Fermi 3FGL catalog does not include distance estimates for its unassociated sources.

The galactic latitude b of a source was instead used as a proxy for distance. From the perspective of Earth at $R_\odot \sim 8$ kpc from the galactic center, sources on the galactic plane have no inherent distance information. As the density of galactic sources falls off exponentially with distance from the galactic plane z, galactic sources at higher latitudes are more likely to be nearby. For population synthesis models based on the Fermi catalog, high-latitude sources are assumed to be characteristic of low-luminosity, high-space-density sources at small distances [23]. The disadvantage to this strategy is that high galactic latitude objects are often extragalactic sources, such as active galactic nuclei. However, the potential value of a nearby undiscovered pulsar for continuous gravitational wave searches justifies the relative risk of spending

Constant	Value	Units
A	44(7)	kpc^{-2}
B	0.2(2)	
C	1.4(6)	
D	0.39(2)	
E	0.33(3)	kpc

Table 6.1: Constant values for equations 6.16 and 6.17 in the Parkes Multibeam model [104].

computational resources pursuing an extragalactic source.

A numerical model of Galactic pulsar distribution was used to define the galactic latitude threshold, based on the model of galactic pulsar distribution developed as part of the Parkes Multibeam survey [104]. The Parkes model used a Monte Carlo method, drawing from flat priors in distance from galactic center R, height above the galactic plane z, logarithm of luminosity $\log L$, and logarithm of pulse period $\log P$, with the goal of modeling the current pulsar population. The pulsar density with respect to galactic radius was modeled as a power law with exponential cutoff,

$$\rho(R) = A \left(\frac{R}{R_\odot} \right)^B \exp\left(-C \left[\frac{R - R_\odot}{R_\odot} \right] \right) \tag{6.16}$$

while the height above the galactic plane was modeled by an exponential function,

$$N = D \exp\left(-\frac{|z|}{E} \right). \tag{6.17}$$

The constants in equations 6.16 and 6.17 depend on the assumed model of electron distribution. The Parkes modelers studied a “smooth” azimuthally symmetric distribution and a “clumpy” distribution that attempted to account for the effect of the galactic arms. The “clumpy” model resulted in a distribution of scale height inconsistent with pulsar observations; therefore, for this model, the constants from the “smooth” model (Table 6.1) were used.

The numerical model of average source distance was parameterized in terms of the sun-centered coordinates of galactic longitude l, galactic latitude b, and source distance d. In terms of (l, b, d) coordinates, the distance from the center of the galaxy is

$$R = \sqrt{(d \cos b \sin l)^2 + (d \cos b \cos l - R_\odot)^2}, \tag{6.18}$$

and the height above the galactic plane is

$$z = d \sin b. \tag{6.19}$$

After substituting equations 6.18 and 6.19 into equations 6.16 and 6.17, the expressions were multiplied together and numerically integrated to determine the percentage of sources with galactic latitudes above a threshold at $|b| > b_{cut}$ (Figure 6.3), and the mean distance to a source (Figure 6.4). The percentage of the model pulsar distribution above a galactic latitude threshold drops sharply as the latitude threshold increases, while the mean distance approaches the scale height parameter E. For the purposes of this investigation, sources with galactic latitudes $|b| > 15°$ were considered. At this latitude, the mean source distance is 650 pc, with 0.5% of model pulsars included.

The Fermi 3FGL catalog includes information about the properties of the gamma-ray spectrum for each source, which are used to select pulsar-like objects from the high-latitude sources for further investigation. The first property considered is the *variability index*. As the variability measured is defined over long-term observations rather than short-term period pulsations, a pulsar is (ironically) a steady source. The 3FGL catalog defines a variability index threshold exceeding 72.44 as having less than a 1% chance of being a steady source, where the variability index is a chi-squared distribution with 47 degrees of freedom [23]. Selected sources were required to have a variability index below this ceiling.

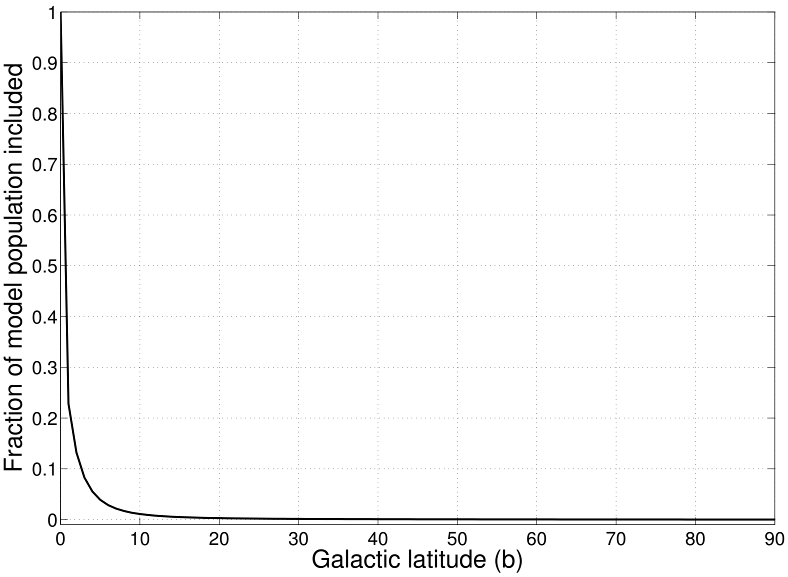

Figure 6.3: Percent of sources included with galactic latitude $b > |b_{cut}|$.

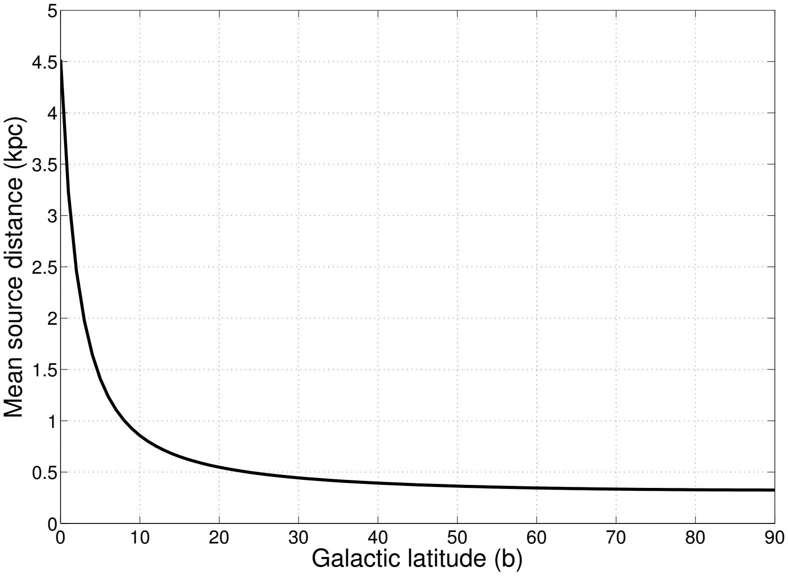

Figure 6.4: Mean distance to a pulsar with galactic latitude $b > |b_{cut}|$.

The other property of interest is the spectral curvature. The Fermi catalog uses three models for spectral curvature: log-parabola, power law with exponential cutoff, and power law. The log-parabola spectrum,

$$\frac{dN}{dE} = K \left(\frac{E}{E_0} \right)^{-\alpha-\beta \log(E/E_0)} \tag{6.20}$$

is characteristic of active galactic nuclei, while the power law with exponential cutoff,

$$\frac{dN}{dE} = K \left(\frac{E}{E_0} \right) \exp \left[\left(\frac{E_0}{E_c} \right)^b - \left(\frac{E}{E_c} \right)^b \right] \tag{6.21}$$

is characteristic of pulsars. A gamma-ray spectrum is considered significantly curved if the curvature test statistic $TS_{\text{curve}} > 16$ [23], where the test statistic is the ratio of the log-likelihood of the observations fitting a curved spectrum to the log-likelihood of a fit to a power law.

All objects with significant log-parabola spectra are excluded from the search. As most objects with distinct power law with exponential cutoff spectra have already been identified as pulsars, the selected set consists of objects with power-law spectra. To prioritize among these sources, a cut is placed on the significance of the curvature,

$$\sigma_{\text{curve}} = \sqrt{TS_{\text{curve}} R_{\text{syst}}}, \tag{6.22}$$

where R_{syst} is a 3FGL-defined quantity accounting for the systematic uncertainties in the effective area of the LAT instrument [23]. The threshold for switching spectra in the 3FGL catalog is $\sigma_{\text{curve}} > 4$; for this search, a cut was placed at $\sigma_{\text{curve}} > 2$. A final cut was made to remove sources that were associated with a data quality flag. In the 3FGL catalog, 73 sources met this list of criteria; the sky positions of the promising sources are shown in Figure 6.5.

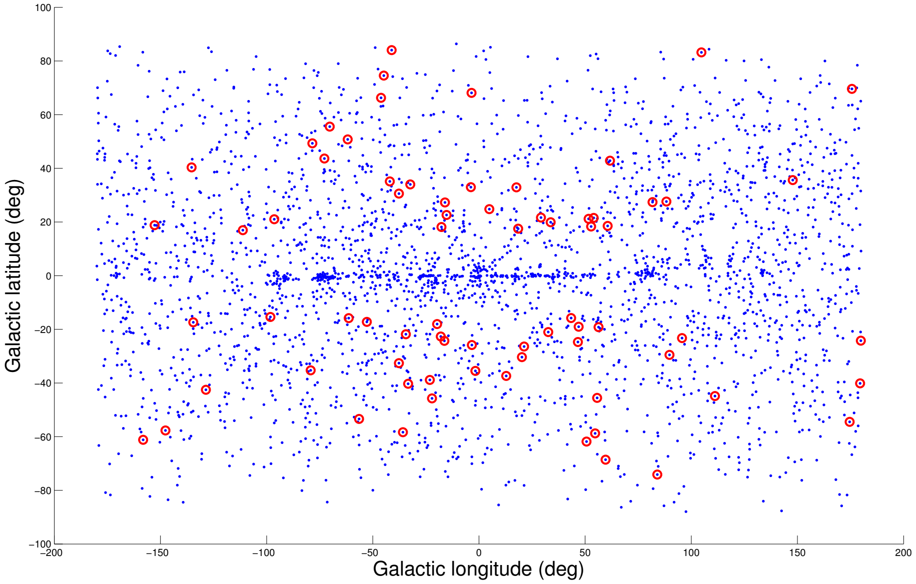

Figure 6.5: Sky positions of promising Fermi 3FGL sources, superimposed on the sky positions of all 3FGL sources. The 73 sources circled in red satisfy the requirements set on data quality, galactic latitude, source variability, and energy spectrum curvature.

6.4 The Effect of Position Uncertainty

Unlike the supernova remnant and globular cluster searches, the Fermi unassociated sources targeted by this search have significant spatial uncertainty. The localization procedure used for the Fermi 3FGL catalog produces a point of highest likelihood with surrounding 68% and 95% uncertainty ellipses, parameterized by semimajor axis, semiminor axis, and angle between declination $\delta = 0$ and semimajor axis [23]. As discussed in section 5.2, each point on the sky has a unique Doppler modulation pattern due to the motion of the Earth with a unique barycentering solution. An offset between the true source position and the position used for barycentering results in a loss of signal due to mismatch.

The validity region for a gravitational wave search is defined as the maximum angular separation between sources such that the two sources could be searched with one barycentering solution, with a defined maximum signal loss due to mismatch M.

As an illustration, this value can be estimated with the Rayleigh criterion Θ_R, which defines the separation at which two sources are spatially resolvable at wavelength λ by an aperture of width w,

$$\sin\Theta_R = 1.22\frac{\lambda}{w}. \tag{6.23}$$

Applying the small angle approximation for sine and changing from wavelength to frequency, the Rayleigh angle can be expressed as

$$\Theta_R \simeq 1.22\frac{c}{wf}. \tag{6.24}$$

Therefore, the angular extent of the validity region is inversely proportional to frequency. As shown in Figure 6.6, for a gravitational-wave search the width of the aperture is the distance between the location of the earth at the beginning and end of the search. For the five-day coherence time used in this investigation, this distance is $w = 1.287 \times 10^{10}$ m, giving an approximate validity region size of

$$\Theta_R \simeq 0.08 f^{-1}\ \text{rad}. \tag{6.25}$$

Although this method derives the correct scaling of validity region with frequency, the calculation for the scaling constant given in Equation 6.25 assumes a strict ephemeris $\{f, \dot{f}, \ddot{f}\}$. Allowing the ephemeris to vary introduces a degeneracy between the frequency parameters of the signal and the sky position. The relatively short five-day coherence time used for these searches allows us to take advantage of this degeneracy, as shown in Figure 6.7, to cover a larger sky area with each search.

A study of signal loss with distance from a source was performed to verify the inverse proportionality of validity region size with frequency and refine the value for the scaling constant. A series of *software injections*, computer-generated gravitational wave signals embedded in iLIGO archival data, were used to test the f^{-1} scaling

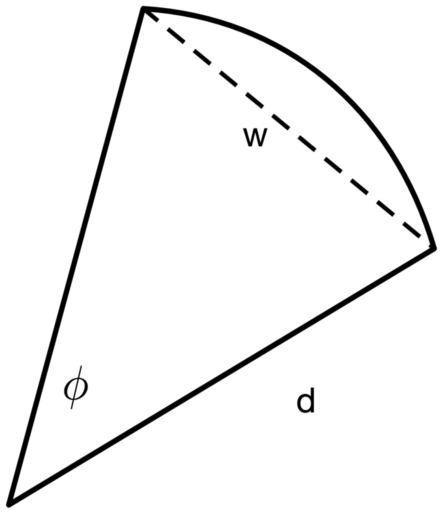

Figure 6.6: Geometry for Rayleigh criterion estimate of template validity angle.

hypothesis and determine the scaling constant for this investigation. Signals were generated at frequencies ranging from 100 to 1000 Hz with strain strength $h = 0.5$. The data was searched for the injected signal at varying distances from the injection point, and the ratio between the recovered signal at the search point and the recovered signal at the injection point was used to determine the mismatch.

Three conditions were considered. In the first investigation, the cosine of the inclination angle $\cos\iota$ was randomized between injections. As a follow-up, extremes of $\cos\iota$ were considered, with $\cos\iota = 0$ for one set of injections and $\cos\iota = 1$ for a complementary set. The polarization ψ and initial phase ϕ_0 were allowed to vary freely for all cases. In the interest of setting a conservative scaling constant, the validity region size was set at the point where the mismatch increased sharply, as observed for the fixed-variable curves in Figure 6.7.

For this investigation, the scaling relation used to determine the validity region size is empirically found to be

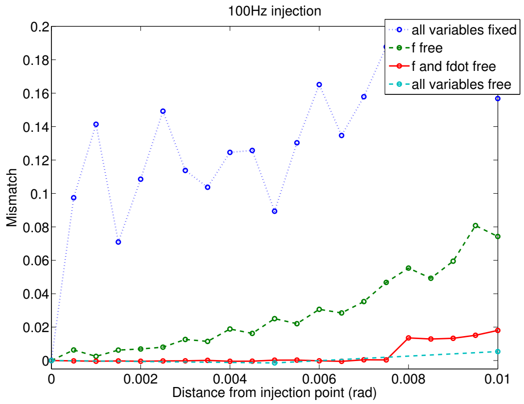

(a) 100 Hz

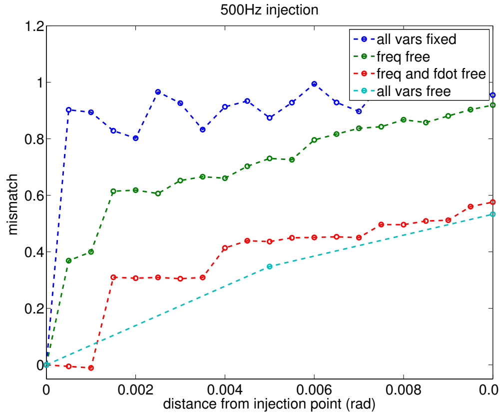

(b) 500 Hz

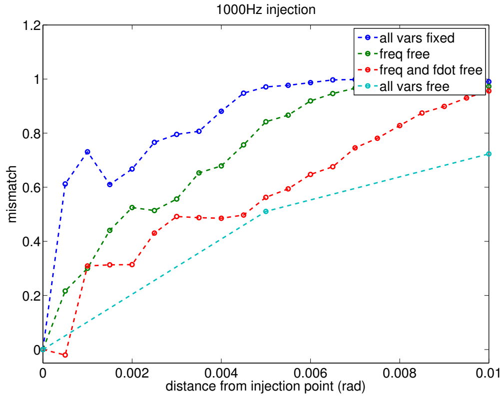

(c) 1000 Hz

Figure 6.7: Mismatch increase with search offset for 100, 500, and 1000 Hz. For a set frequency and spindown, the mismatch increases quickly with radius (blue curve). Allowing the frequency and spindown to vary increases the tolerance to mismatch; the cyan curve is the mismatch allowing full variance of frequency, spindown, and spindown derivative, and is the curve used to set the mismatch scaling.

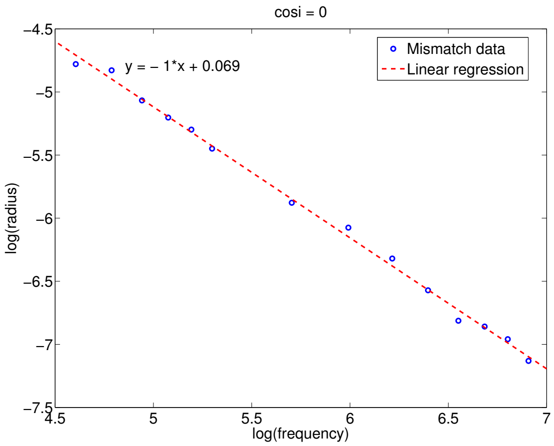

(a) $\cos\iota = 0$

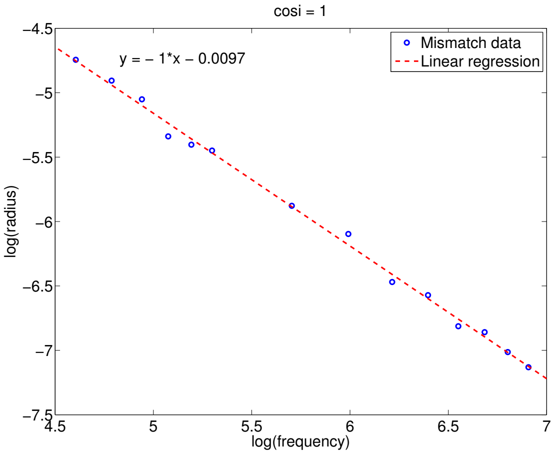

(b) $\cos\iota = 1$

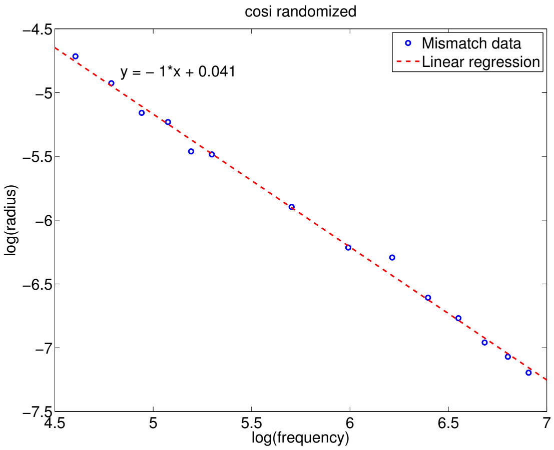

(c) $\cos\iota$ random

Figure 6.8: Verification of inverse proportionality between mismatch and frequency. For each test case, the mismatch radius was determined for frequencies from 100 to 1000 Hz, then plotted on a log scale. A linear fit was used to verify the f^{-1} scaling.

$$\theta(f) = 0.83f^{-1}. \tag{6.26}$$

The need to use multiple searches to cover the uncertainty region places this investigation in an intermediate regime between previous directed searches and all-sky searches. When multiple sky positions are needed to cover the uncertainty region, the computational complexity of the search is increased by a factor of the number of sky positions. The inverse dependence of validity region size on frequency causes the complexity to grow with frequency, where the computational costs are already increasing because of the expanding frequency derivative parameter space.

To determine the sky position tiling required for each source, the 95% uncertainty region from the 3FGL catalog (the solid red ellipse in Figure 6.9) is increased in size by 20% to define a tiling boundary (the dashed green ellipse in Figure 6.9). The first template is placed at the center of the uncertainty region, (α_0, δ_0). A circle with radius $\theta(f)$ is defined, and templates are placed every $\frac{\pi}{2}$ radians, with the first template placed on the semimajor axis. The template is searched if it lies within the tiling boundary; otherwise, it is discarded. The process is repeated on circles with radius $N\theta(f)$ with template placement every $\frac{\pi}{2N}$ radians until all proposed templates lie outside the tiling boundary. For a source with a small uncertainty region, as shown in Figure 6.9(a), the number of templates required is small, even at 1000 Hz. For a source with a larger uncertainty region, as shown in Figure 6.9(b), the number of templates increases roughly as the square of the frequency, as shown in Figure 6.11.

6.5 Source Prioritization

6.5.1 Determining Computational Cost

At this time, gravitational wave search methods are too computationally intensive to permit a deep directed search for 73 sources. The additional requirement of sky

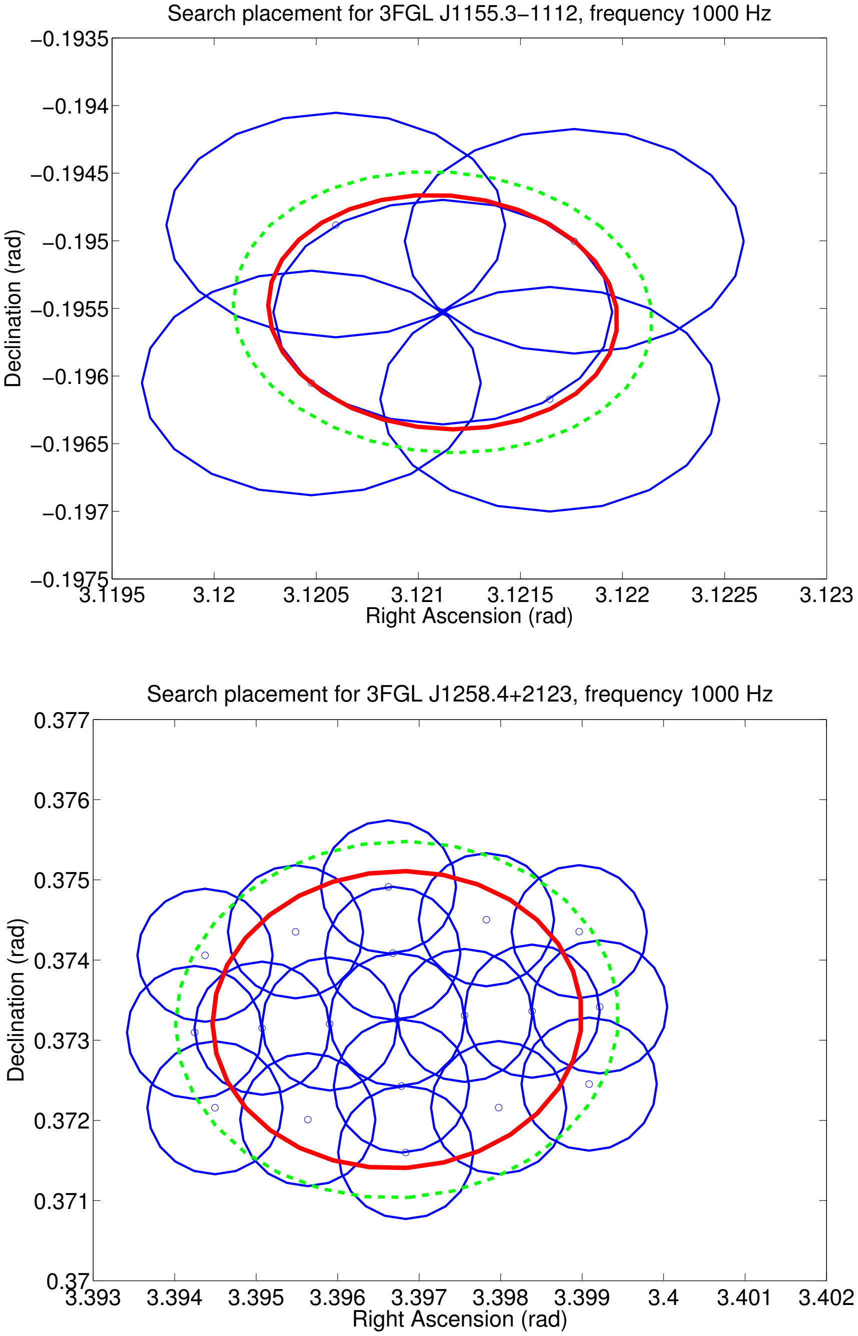

Figure 6.9: Sky tiling at 1000 Hz for a well-localized source 3FGL J1155.3-1112 and a less-certain source 3FGL J1258.4+2123. The Fermi uncertainty ellipses are in solid red, and the tiling boundary used for template placement is in dashed green. Each template center is marked by a small circle, with the validity region for each template shown as a solid blue circle.

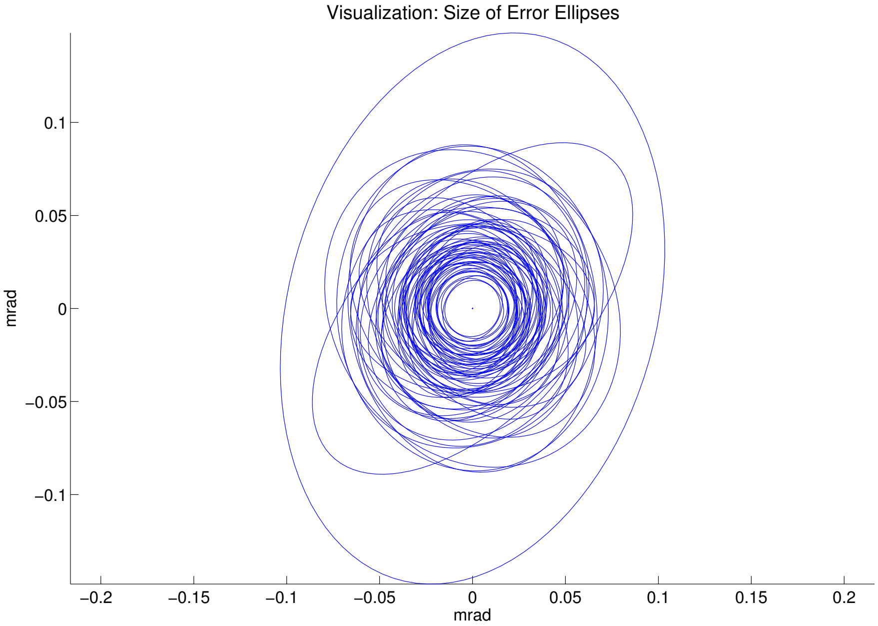

Figure 6.10: 95% uncertainty ellipses for selected 3FGL sources, shifted to have a common central point. Sources with better sky localization are preferred for searches to avoid excessive computational cost.

templating to cover the uncertainty regions shown in Figure 6.10 increases the cost for each source with frequency. There will necessarily be a limit on the number of sky positions that can be considered before a fully coherent search becomes computationally intractable. For a search that aims to cover the maximum number of potential sources fully coherently, a limit on sky positions per search will be required.

Sources with larger uncertainty regions will have higher computational costs due to the additional sky templates required to cover the uncertainty region. The increase in computational cost can be quantifed in terms of the number of templates, or combinations of $\{f, \dot{f}, \ddot{f}, \alpha, \delta\}$ used as matched filters. Using the template spacings $\{df, d\dot{f}, d\ddot{f}\}$ given in equation 6.3 and the ranges of frequency derivatives given in equations 6.10 and 6.11, the number of templates N_t is a function of frequency f, spindown age τ, mismatch M, and coherence time T_{coh},

$$N_t(f, \tau, M, T_{\text{coh}}) = \frac{65 f^3 \pi^3 T_{\text{coh}}^6}{20736 \tau^3 \sqrt{105 M^3}}. \tag{6.27}$$

This function does not take the effect of sky tiling into account. To incorporate the effect of tiling, a tiling function $N_{\text{sky}}(f)$ was computed for each source under investigation. This was computed by dividing the frequency range 50-1000 Hz into 0.1 Hz bands and performing an analytic sky position placement, as shown in Figure 6.9, for each band. The resulting curves are shown in Figure 6.11 for two representative sources. The number of templates required to search each 0.1 Hz band is then multiplied by the number of sky positions required to cover the error ellipse, and the result from all bands are summed to determine the total number of templates. As the template counts considered in this work are on the order of $10^{11} - 10^{13}$, the template count is converted to CPU-months for clarity, using an assumed conversion of 3.6×10^{-12} CPU-months per template taken from the globular cluster resampling search [52].

6.5.2 Approaches to Source Prioritization

A scheme for selecting a subset of potential sources for analysis is required to maximize the scientific potential, given available computing power. For this analysis, two possible methods of set selection were considered. The computational cost of the search is driven by the number of sources searched, the size of the uncertainty region for each source, and the frequency range covered by the search.

One possible prioritization is the maximization of frequency range. As discussed in Chapter V, fast-spinning pulsars are difficult to detect in gamma rays. A gravitational wave search with a maximum frequency f_{max} will be sensitive to stars with spin frequency less than $\frac{f_{\text{max}}}{2}$; searching to the maximum frequency allowed by the age-based strain limit maintains sensitivity to fast-spinning stars. The sensitivity gains made between the S5 and S6 science runs were greater at high frequencies, and greater

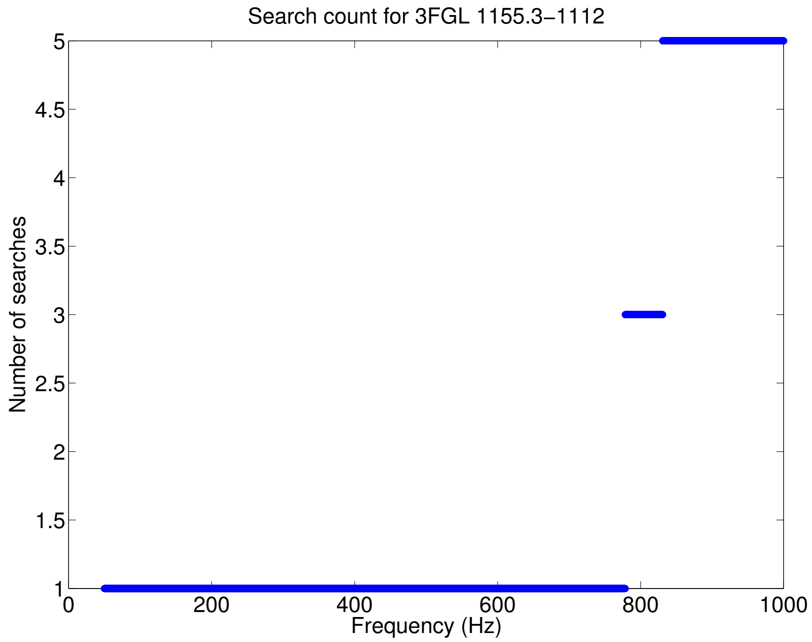

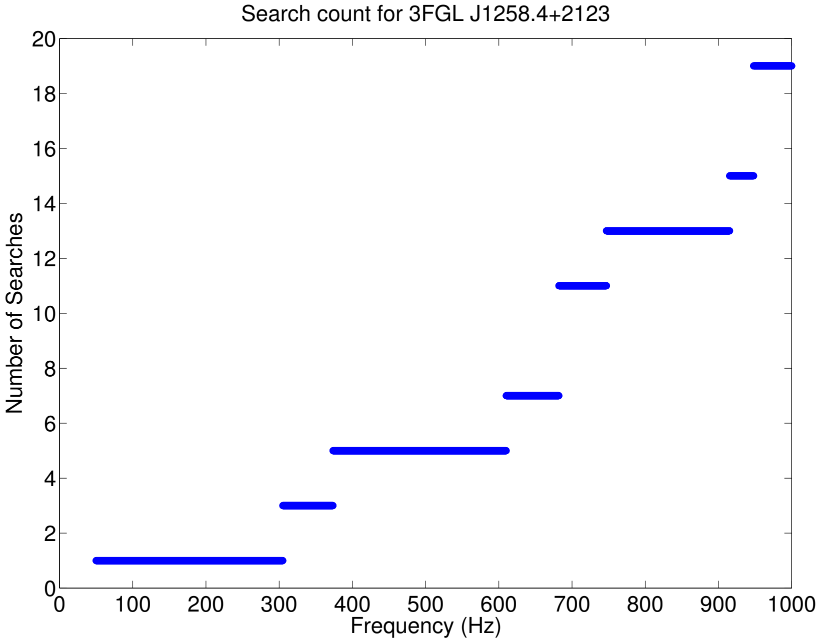

Figure 6.11: Sky template counts with frequency for a well-localized source 3FGL J1155.3-1112, and a less-certain source 3FGL J1258.4+2123.

improvement will be made over the Einstein@Home S5 all-sky results, as shown in Figure 6.1 [2]. However, the increase in computational cost with frequency means only sources with small uncertainty regions will be cost-effective to search. The area covered by one template at 1000 Hz is 0.8 milliradians. None of the selected sources have uncertainty regions smaller than a single template at 1000 Hz, and the estimated computational cost to search the two sources with the smallest uncertainty regions is over 600 CPU-months, with more than 500 CPU-months used to search frequencies between 770-1000 Hz [1].

Reducing the frequency range searched to restrict the number of sky positions considered allows more sources to be considered for a given computational time. Covering a broad selection of sources will increase discovery potential, and investigations of the optimal allocation of computing resources for directed searches have shown that the highest detection probability lies in the most sensitive region of the interferometer [118]. Choosing to prioritize number of source searched at the expense of frequency has the risk of neglecting higher-frequency sources, and will not be competitive with the Einstein@Home all-sky results pending for S6. However, the lightweight nature of the search will be of greatest benefit in aLIGO data, where short data stretches with increased sensitivity can be used to search for gravitational waves quickly and before an Einstein@Home search can be completed.

The computational cost increase introduced by tiling provides natural endpoints for frequency searches. If the frequency range is set by maximum frequency searchable with a single sky pointing, ten sources can be searched in 100 CPU-months; if three templates are allowed, eight sources can be searched in less than 350 CPU-months to a frequency of at least 600 Hz. Reducing the frequency range allows more sources to be searched in the most sensitive frequencies of the LIGO instrument.

---

[1] See Appendix B for computational estimates by source and frequency.

	3FGL J1155.3-1112	3FGL J1258.4+2123
Right Ascension (deg)	178.8270	194.6183
Declination (deg)	-11.2029	21.3860
Galactic longitude (deg)	281.5305	318.9062
Galactic latitude (deg)	49.3222	84.0382
Variability index	34.7216	43.3125
Curvature significance	2.7273	2.8974
Semimajor axis (mrad)	0.8884	2.2672
Semiminor axis (mrad)	0.8325	1.8518
Angle of ellipse from $\delta = 0$ (deg)	39.1400	-86.3300

Table 6.2: Parameters of the pilot search sources.

6.6 Description of Pilot Search

As no previous directed search for continuous gravitational waves considered an object with uncertainty large enough to require multiple sky pointings, two sources were chosen from the Fermi 3FGL catalog for proof of method, testing the effect of sky position, and developing post-processing techniques. For each of these sources, a frequency range from 50-340 Hz was divided into 0.1 Hz frequency bands. The highest frequency searched was chosen to lie below the violin mode resonance of the suspension wires of LIGO core optics. Optimization studies suggest that the highest detection probability for a directed search lies below this frequency [118], and the additional frequency restriction allows investigation of two sources in less than 3 CPU-months. This descoped version of the search allowed for rapid iteration and improvement of investigation techniques in advance of the first aLIGO science run.

For a search below the violin mode, the frequency range searched is

$$50 \text{ Hz} \leq f \leq 340 \text{ Hz}, \tag{6.28}$$

the spindown range searched is

$$8.8083 \times 10^{-10} \leq -\dot{f} \leq 3.5938 \times 10^{-8} \text{ Hz s}^{-1} \tag{6.29}$$

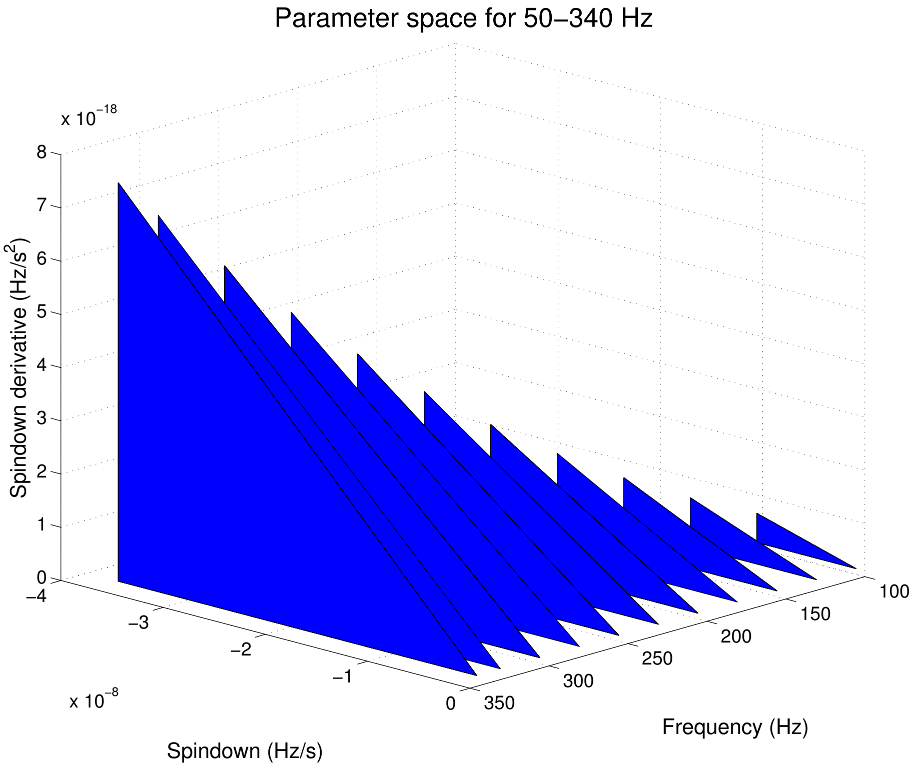

Figure 6.12: Visualization of frequency parameter space covered by pilot search.

and the spindown derivative range searched is

$$1.0862 \times 10^{-19} \leq \ddot{f} \leq 2.5830 \times 10^{-15} \text{ Hz s}^{-2}. \tag{6.30}$$

The range of spindown and spindown derivatives searched varies with frequency; this parameter space is shown in Figure 6.12.

6.7 Post-Processing

6.7.1 Outlier Investigation

The output of the search is a list of the highest $2\mathcal{F}$ values for each 0.1 Hz frequency band. The $\mathcal{F}$-statistic is a function of both the noise state of the interferometer and any potential gravitational wave signal, as shown by the derivation in section 5.2.2. A gravitational wave signal incident on the interferometer would cause an elevated value of $2\mathcal{F}$, or outlier. Statistical fluctuations and noise features in the interferometer, however, also cause elevated $2\mathcal{F}$ values. Assumed properties of physical signals are used to distinguish transient noise sources and statistical fluctuations from genuine signals.

Two vetos are applied to the results to account for the effects of instrumental artifacts. The F-scan veto, as applied in searches for supernova remnants [10][7], discards bands with significant deviations from Gaussian noise. The $\mathcal{F}$-statistic consistency veto exploits the fact that a real signal would be observed in both interferometers, with a combined $\mathcal{F}$-statistic larger than either of the values in a single interferometer. Candidate signals that do not satisfy this condition are vetoed.

The threshold of significance for $2\mathcal{F}$ was determined by generating 1000 signals in a 1 Hz band between 200 - 201 Hz, with random signal parameters $\{f, \dot{f}, \ddot{f}, \cos\iota, \Psi, \phi_0\}$ and strain set by the 95% strain upper limit determined by the method discussed below. The $2\mathcal{F}$ value corresponding to 80% recovery is selected as the threshold for outlier significance.

Significant outliers are searched for in two additional data stretches, following the approach developed for the globular cluster search [52]. For continuous wave sources, a search in a data stretch at a later time should recover the outlier. For outlier testing, a second period of data from September 15 2010 20:37:16 UTC (GPS 968618251) to September 20 2010 UTC (GPS 969050251) was chosen. The candidate outlier, $\{f_c, \dot{f}_c, \ddot{f}_c\}$, will come from a single template. Given the assumption that template can have up to 20% mismatch, simply moving the single outlier frequency is not sufficient. The outlier template is used to form an initial parameter space of the outlier template plus or minus two bins of size given by Equation 6.3. The third frequency derivative is assumed to be negligible, so $\ddot{f}$ is assumed to be constant. The frequency and frequency derivative ranges are evolved in time to the second time period and searched. To determine the $2\mathcal{F}$ value required to consider an outlier recovery significant, the 1000 injections used to set the initial significance threshold were evolved forward and searched, and the 80% recovery value used to set the threshold for outlier recovery.

The second condition considered is that the returned $2\mathcal{F}$ for a real source should increase with coherence time. Each significant outlier, plus or minus two bins, is searched for in a 20-day stretch of data, from July 30 2010 08:43:55 UTC (GPS 964514650) to August 19 2010 08:43:55 UTC (GPS 966242650). The significance threshold was again set by performing the same set of 1000 injections in 20 days of data and using the 80% recovery value to set the threshold for recovery.

6.7.2 Upper Limit Estimation

In the case where no statistically significant outlier remains, the result of a gravitational wave search is reported as a frequentist strain upper limit $h_0^{95\%}$, the h_0 level at which 95% of all possible signals would have been detected. Previous searches determined $h_{95\%}$ from measured $2\mathcal{F}$ values from a two-step process [10][7][52]. First, the upper limit value is estimated using a computationally cheap combination of analytic and Monte Carlo methods. This strain is used to set a range of strain values for a large number of fake signals with randomly chosen signal parameters $\{\cos\iota, \Psi\}$. The signal at the detector, equation 5.11, is a function of the strain amplitude h_0 as well as the polarization Ψ and the inclination angle $\cos\iota$. These signals are injected into archival data, and the $\mathcal{F}$-statistic is computed for the known signal. A signal is said to be recovered if a $2\mathcal{F}$ value larger than the maximum seen in the search is returned; the recovery rate is then used to determine $h_0^{95\%}$. Although this is a necessary element of post-processing, it is a computationally intensive process, taking $20\% - 30\%$ of the computational cost of the initial search [7]. Refinements to the process to reduce the computational cost were made to improve the potential for searching large numbers of sources at low cost.

The recovery curve is well described by a sigmoid, with zero recovery for low strain signals, and 100% recovery for high strain signals. For this investigation, the recovery efficiency R was fitted to a logistic function,

$$R(h_0) = \frac{1}{1 + e^{-a(h_0 - b)}}. \tag{6.31}$$

Due to the physical motivation of the definition of this curve, a set of injections at a test strain strength h_{test} probes the true value of $R(h_{\mathrm{test}})$. In the frequentist interpretation, this efficiency $R(h_{\mathrm{test}})$ is the probability that a random selection from the set of all possible signal parameters $\{\cos\iota, \Psi\}$ is recoverable at h_{test}. Therefore, the number of recovered injections K from a set of N injections are drawn from a binomial distribution with probability mass function

$$f(K; N, R(h_{\mathrm{test}})) = \binom{N}{K} R(h_{\mathrm{test}})^K (1 - R(h_{\mathrm{test}}))^{(N-K)}. \tag{6.32}$$

For this work, the upper limit value was estimated for each of the 0.1-Hz search bands, then averaged over 1-Hz bands to determine an estimated strain limit for each band, $h^{95\%}_{\mathrm{est}}$. For each 1-Hz upper limit band, a set of 100 injections with randomly chosen $\cos\iota$, Ψ, and sky location within the 3FGL uncertainty ellipse were made at each of eight strains. Initially, they were placed evenly above and below the estimate, $h_{\mathrm{inj}} = h^{95\%}_{\mathrm{est}} \times \{0.8, 0.85, 0.9, 0.95, 1.05, 1.1, 1.15, 1.2\}$. As this set of strain injections typically caused large uncertainties in the strain upper limit estimation, the strain injections were shifted to $h_{\mathrm{inj}} = h^{95\%}_{\mathrm{est}} \times \{0.6, 0.7, 0.8, 0.85, 0.9, 0.95, 1.05, 1.1\}$.

The recovery rates for this set of injections were used as an ansatz for the recovery rate curve, $R'(h_{\mathrm{inj}})$. To determine the 95% upper limit value, 1000 sets of 100 injections at each of h_{inj} were simulated as binomial tests with rate assumptions according to $R'(h_{\mathrm{inj}})$. A logistic curve was fit to each of these sets of injections, and inverted to

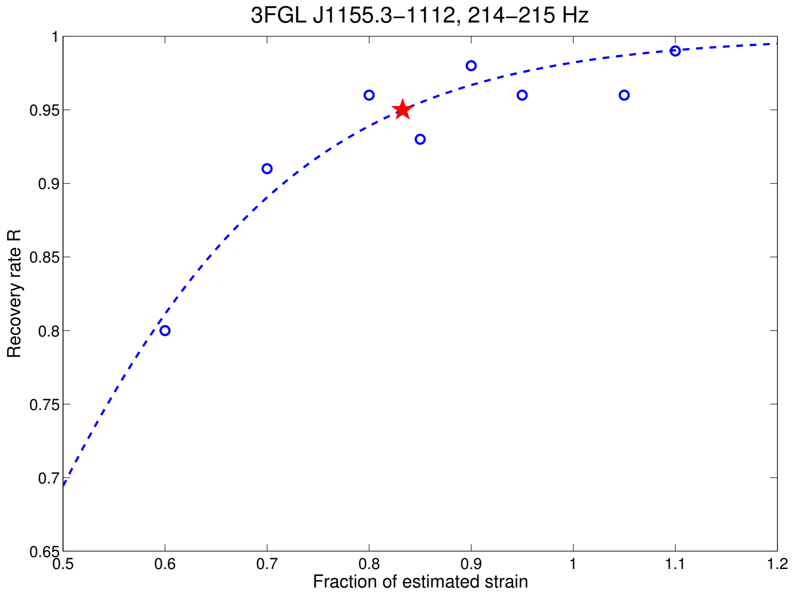

Figure 6.13: Sample logistic distribution with fit for 3FGL J1155.3-1112. The blue points are the recovery rates from a set of 100 injections at each point. The blue line is the best fit to the logistic function (Equation 6.31), and the red star is the scale factor to be used to find the 95% upper limit.

find the strain at $R^{-1}(0.95)$.

The reported strain value is the mean of the set of strains from 1000 simulated tests. This result was considered to be valid if the standard deviation of the strain set was less than 10% of the mean. If the standard deviation was larger than 10% of the mean, additional injections were performed. In some cases, the semi-analytic method overestimated the strain, and a lower set of injections at $h_{\mathrm{est}}^{95\%} \times \{0.4, 0.45, 0.5\}$ were performed. In others, the semi-analytic method underestimated the strain, and a higher set of injections at $h_{\mathrm{est}}^{95\%} \times \{1.2, 1.4, 1.6\}$ were performed. The fitting process was performed in the basis of percent of estimated strain, and the output is a modification factor used to scale the curve. The distribution of these scale factors for source 3FGL J1155.3-1112 is shown in Figure 6.14.

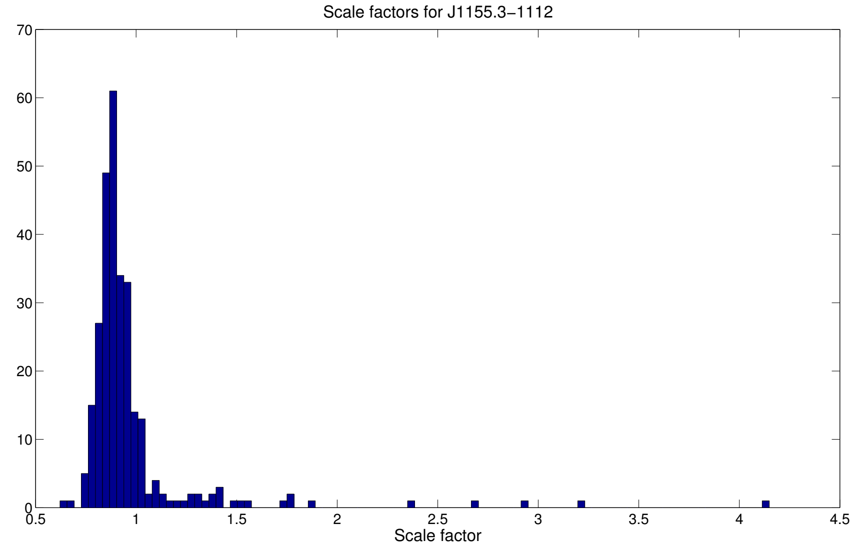

Figure 6.14: Distribution of scale factors for upper limits from 3FGL J1155.3-1112.

Source	Minimum $h_0^{95\%}$	Frequency Band	Minimum ϵ	Frequency Band
3FGL J1155.3-1112	3.1×10^{-25}	168.0-169.0	1.983×10^{-5}	320.0 - 321.0
3FGL J1258.4+2123	5.3×10^{-25}	165.0-166.0	2.105×10^{-5}	328.0 - 329.0

Table 6.3: Lowest upper limits for pilot search sources.

6.8 Results

Two sources were considered for this pilot search. 3FGL J1155.3-1112 has the smallest uncertainty region of the selected sources, and is searchable to 778.5 Hz with one sky position. This source is among the most promising 3FGL sources, and the test search probes the high-sensitivity region below the violin mode where a detection is most likely. 3FGL J1258.4+2123 was selected from the source list because the size of its uncertainty region is such that additional pointings are needed between 305.5 Hz and the violin mode at 340 Hz, providing a convenient test case for handling multiple sky positions. This source also has a very high galactic latitude at $b = 84.0382°$. Recalling the results of the source density modelling shown in Figure 6.4, the mean distance for a galactic neutron star at that latitude is 330 pc. Given the inverse scaling of strain with distance, such a nearby neutron star would be of great interest for gravitational wave searches.

6.8.1 3FGL J1155.3-1112

No credible outliers were seen for a gravitational wave search between 50-340 Hz. Out of a set of 25 outliers, ten survived the vetoing process. One of these, at 320.4 Hz, was due to an instrumental noise artifact in H1. Five were associated with instrumental noise artifacts in L1, including the documented 16-Hz comb and 2-Hz lines. Two, at 108.8 Hz and 192.4 Hz, were due to pulsar hardware injections. During the course of the S6 run, ten simulated pulsar signals were injected into the LIGO instruments for calibration purposes [7]. Simulated pulsar 3 had a simulated position of 115329.4-332612 [7] with a strain strength of 1.63×10^{-23}; it is unsurprising that it was observed in a search for the relatively nearby J1155.3-1112. Pulsar hardware injection 8 was not near the searched position; however, it has a high simulated strain strength of 1.59×10^{-23} and therefore is often detected in directed searches for isolated pulsars at distant sky positions. The outliers at 311.7585 Hz and 312.0714 Hz are

Frequency (Hz)	$\dot{f}$	$\ddot{f}$	$2\mathcal{F}_{\max}$	Source
96.0077	-9.1989×10^{-10}	1.1082×10^{-16}	126.6	L1-only line (16 Hz comb)
108.8576	-8.6965×10^{-10}	5.7584×10^{17}	891.6	Pulsar hardware injection 3
186.0147	-9.9440×10^{-10}	2.9156×10^{-17}	75.0	L1-only line (2 Hz line)
192.4910	-1.3307×10^{-8}	1.8213×10^{-16}	526.4	Pulsar hardware injection 8
194.1218	-1.5485×10^{-8}	3.7310×10^{-17}	72.3	L1-only line (2 Hz line)
244.0196	-2.7301×10^{-9}	2.3541×10^{-16}	84.1	L1-only line (2 Hz line)
298.0234	-1.8455×10^{-10}	2.5352×10^{-16}	60.7	L1-only line (2 Hz line)
311.7585	-2.2859×10^{-8}	3.8722×10^{-16}	62.0	Inconsistent with isolated NS
312.0714	-2.1924×10^{-8}	4.3757×10^{-17}	62.2	Inconsistent with isolated NS
320.4127	-4.1867×10^{-9}	4.1915×10^{-16}	75.5	H1-only line

Table 6.4: Outliers passing vetoes for 3FGL J1155.3-1112.

not associated with any known instrumental artifact or hardware injection. Although they are not definitively eliminated by this analysis, their behavior is inconsistent with that of an isolated neutron star; the maximum outlier $\mathcal{F}$-statistic value does not increase with observation time.

As no credible gravitational wave signal was observed, the result of the search is a set of frequentist strain upper limits on the gravitational wave output from a potential pulsar. Given the strain upper limits, limits on the ellipticity and r-mode amplitude of a potential pulsar can be set. Assuming a neutron star moment of intertia of $I_{zz} = 10^{45}$ g cm^2, the strain upper limit can be converted to a limit on ellipticity [169] [10] [7],

$$\epsilon = 3.9 \times 10^{-4} \left(\frac{h_0}{1.2 \times 10^{-24}}\right) \left(\frac{\tau}{300\text{ yr}}\right)^{1/2} \left(\frac{100\text{ Hz}}{f}\right)^2 . \tag{6.33}$$

For the plot in Figure 6.16, τ was assumed to be 300 years. A similar conversion can be used to set limits on the r-mode amplitude α [7],

$$\alpha = 0.28 \left(\frac{h_0}{10^{-24}}\right) \left(\frac{100\text{ Hz}}{f}\right) \left(\frac{d}{1\text{ kpc}}\right) , \tag{6.34}$$

where for the plot in Figure 6.17, a source distance of 1 kpc was assumed.

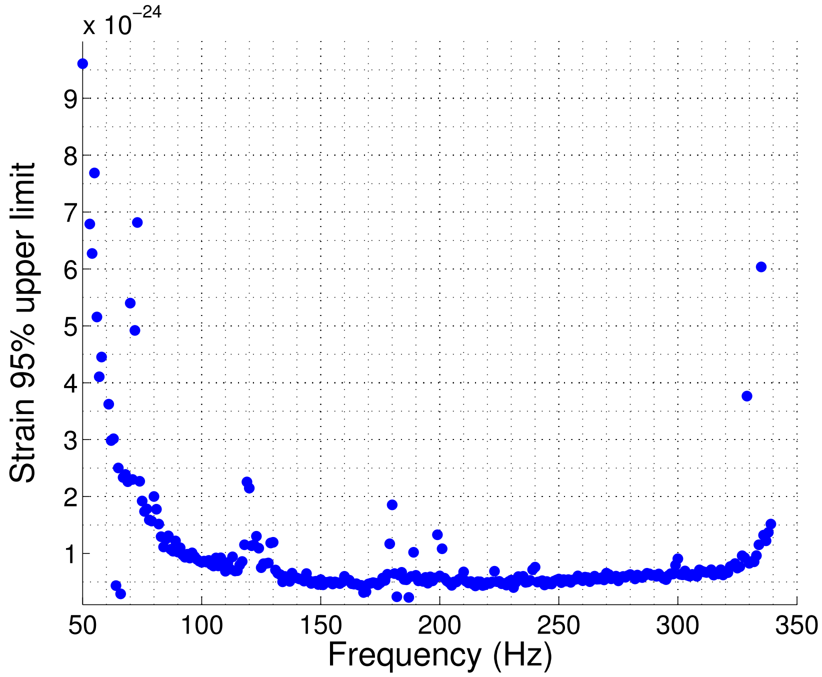

Figure 6.15: Strain upper limits for 3FGL J1155.3-1112.

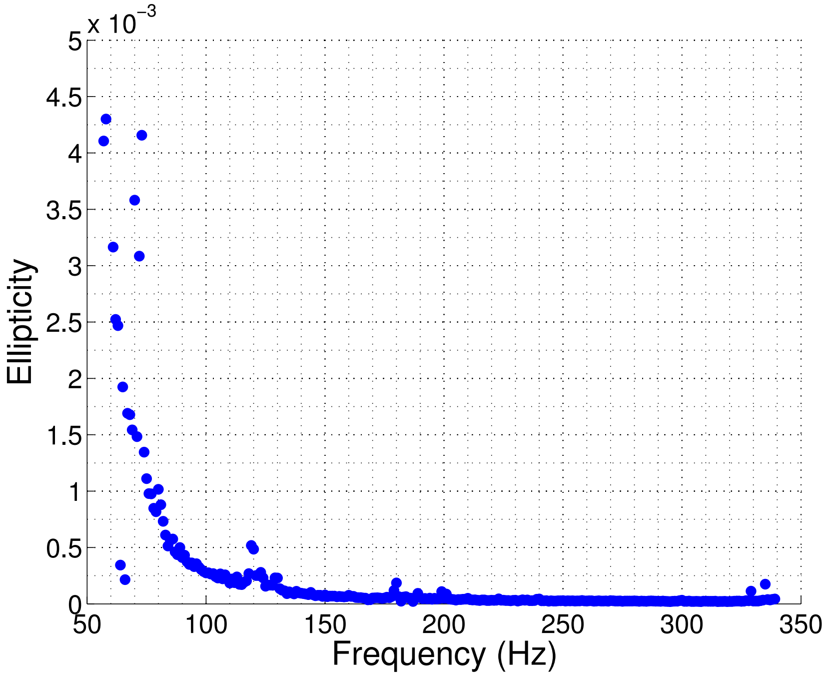

Figure 6.16: Ellipticity upper limits for 3FGL J1155.3-1112.

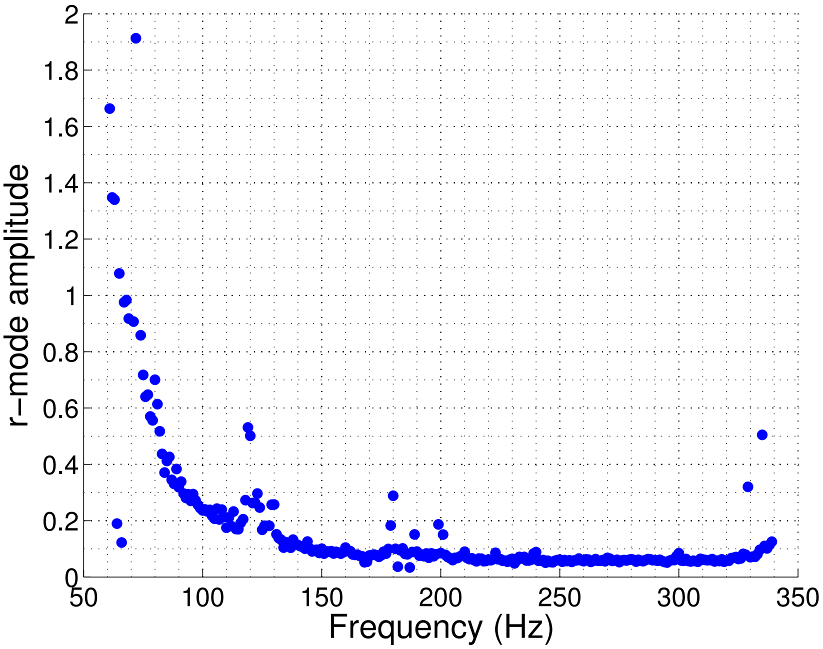

Figure 6.17: r-mode amplitude upper limits for 3FGL J1155.3-1112.

Frequency (Hz)	$\dot{f}$	$\ddot{f}$	$2\mathcal{F}_{\max}$	Source
108.8570	-8.6965×10^{-10}	-5.3821×10^{-17}	349.9736	Pulsar hardware injection 3
145.6009	-1.1852×10^{-9}	6.5957×10^{-17}	69.3249	L1-only signal
192.4900	-1.3214×10^{-8}	1.5680×10^{-16}	859.0861	Pulsar hardware injection 8
194.1319	-5.8483×10^{-9}	-3.4920×10^{-17}	65.3313	Non-stationary noise in L1
308.0229	-3.2731×10^{-9}	1.9722×10^{-16}	95.3340	L1-only line (2 Hz line)

Table 6.5: Outliers passing vetoes for 3FGL J1258.4+2123

6.8.2 3FGL J1258.4+2123

No credible outliers were seen for a search between 50-340 Hz at the location of 3FGL J1258.4+2123. Of twenty outliers, five survived the vetoing process. Two of these were the same pulsar hardware injections detected in the search for 3FGL J1155.3-1112. One, at 308.0229 Hz, was associated with a 2-Hz line in L1, while another at 194.1319 Hz was associated with a non-stationary noise floor in L1. The outlier at 145.6009 Hz was not associated with a run-averaged instrumental artifact; however, for an increased integration time, an increase in $\mathcal{F}$-statistic was only seen in L1 data, which is inconsistent with the expectation of true gravitational signal.

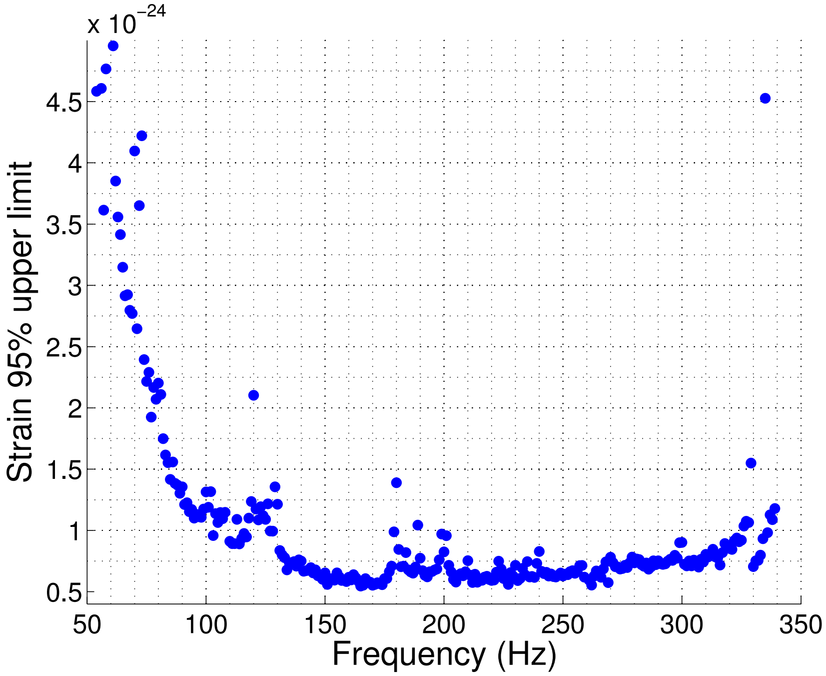

Figure 6.18: Strain upper limits for 3FGL J1258.4+2123.

As for 3FGL J1155.3-1112, the result of this search is a set of strain upper limits, shown in Figure 6.18. These results were converted into limits on detectable ellipticity (Figure 6.19) and r-mode amplitude (Figure 6.20). The upper limits set for 3FGL J1155.3-1112 are stronger with the exception of the frequency span from 300-340 Hz, where tiling was required to cover the 3FGL J1258.4+2123 uncertainty region. As shown in Figure 6.9, the search tiles cover the uncertainty region with significant overlap. Therefore, large portions of the search region are covered by multiple templates, increasing the probability of a significant injection recovery.

6.9 Discussion and Future Work

6.9.1 Significance of Work

This search is the first to consider bright gamma-ray emitters of unknown classification, testing a mode of directed gravitational wave search that can constrain parameter spaces for cases where gamma ray pulsations are difficult to distinguish

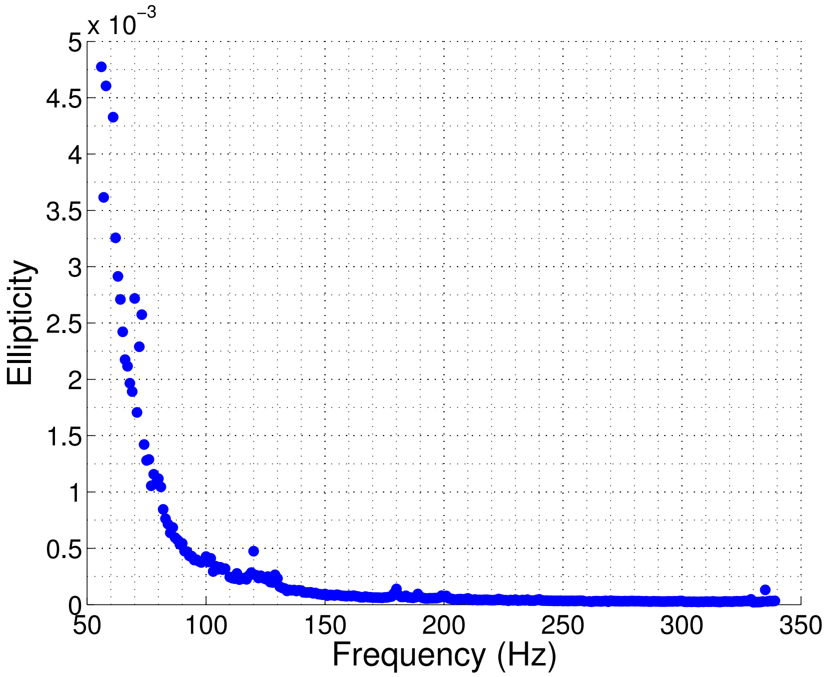

Figure 6.19: Ellipticity upper limits for 3FGL J1258.4+2123.

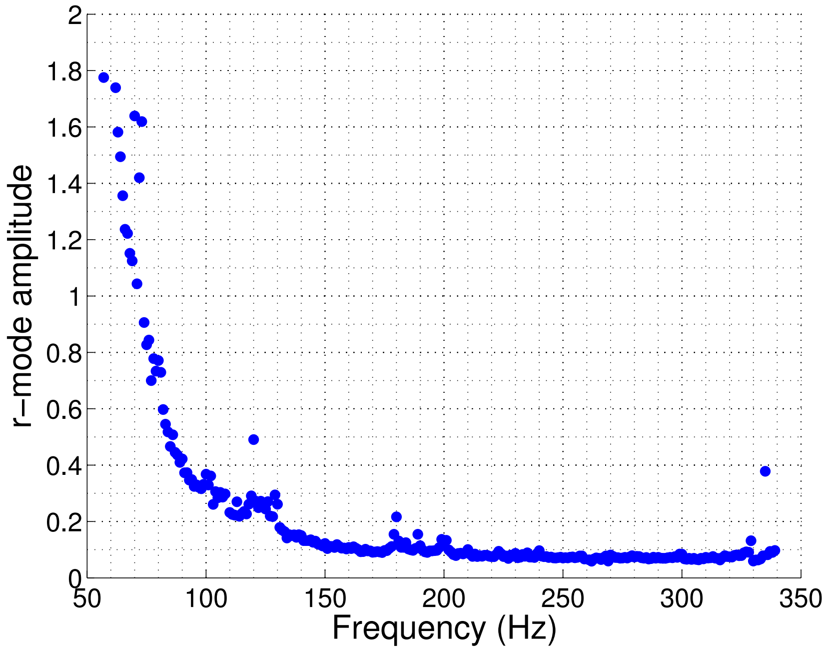

Figure 6.20: r-mode amplitude upper limits for 3FGL J1258.4+2123.

and no radio signal is detected. Searches of this type expand the range of potential contributions of gravitational wave observations to the study of individual neutron stars, and have the potential to discover gamma-loud pulsars through gravitational wave pulsations. The spatial tiling detailed in section 6.4 is unique among fully-coherent directed searches. This advance was required to extend fully-coherent directed gravitational wave searches to the poorly localized unassociated gamma ray sources.

The strain upper limits achieved in this search, as low as $3.1 \pm 0.3 \times 10^{-25}$ for the frequency band between 168-169 Hz, improve upon those achieved for other searches involving multiple sky positions. The closest comparable search is the Spotlight search for continuous gravitational waves from the Orion spur, which adapted the semi-coherent PowerFlux all-sky search pipeline [12] to cover a sky area with radius 0.06 radians [9]. Making a direct comparison between the Spotlight results and these results is difficult, as the PowerFlux pipeline reports its upper limits in terms of the best-case upper limits for circular polarizations and worst-case upper limits for linear polarizations, rather than marginalizing over all possible polarizations as in this work. The strongest upper limit set for linear polarizations in the Spotlight search was 6.3×10^{-25} [9]; the strongest upper limit set by this search improves upon that limit by a factor of 2. The strain upper limits set here are also stronger than all currently published all-sky results, surpassing the strongest limit set by Einstein@Home at 7.5×10^{-25} [2] and the best-case result from the PowerFlux search at 3.6×10^{-25} [12].

This search is also the first to consider a sky uncertainty region while incorporating the second derivative of frequency. The Orion spur search and the Einstein@Home search consider only the first derivative of frequency; this search covers both the first and second derivative of frequency. Although the first frequency derivative is sufficient to search for sources with spin characteristics similar to known neutron stars, accounting for the effect of $\ddot{f}$ allows this search to consider sources with higher braking indices [1].

The strongest limits set on the ellipticity of a potential neutron star reach physically interesting levels. The most recent estimates of the maximum possible ellipticities for elastically supported quadrupoles set the maximum ellipticity at order 10^{-6} for canonical neutron stars, order 10^{-3} for baryon-quark hybrid stars, and order 10^{-1} for quark stars [89]. The lowest ellipticity upper limit obtained, $\epsilon = 1.983 \times 10^{-5}$ for the 319-320 Hz band, approaches the range of ellipticities expected for normal neutron stars. The sensitivity achieved in this pilot search suggests that a gravitational wave search would be sensitive to alternative models of neutron stars in Fermi 3FGL unassociated sources.

The lack of distance information makes it difficult to make statements about the r-mode amplitude observed, as was done for the supernova remnant searches [10][7]; the values of α reported are made with the assumption that the source of interest is 1 kpc away, and do not reach physically interesting levels. However, for a full search, the values of α are in a regime such that limits could be placed on r-mode emission; a full search will probe a factor of 2 higher in frequency, and a source at the assumed mean distance of 650 pc derived above will gain a factor of 2 enhancement. For such a source, a limit on r-mode amplitude near the theoretically calculated order 10^{-3} [42] could be achieved.

6.9.2 Expected Sensitivity Improvements in the Advanced LIGO Era

The first aLIGO observation run (O1) began on September 18 2015 15:00:00 UTC (GPS 1126623617); at the beginning of this first observational period, the sensitivity of the detector network was more than three times peak iLIGO sensitivity. Any future searches for Fermi 3FGL unassociated sources will be performed in aLIGO data, and the sensitivity improvements from the instruments will improve the sensitivity of the search at fixed computing cost.

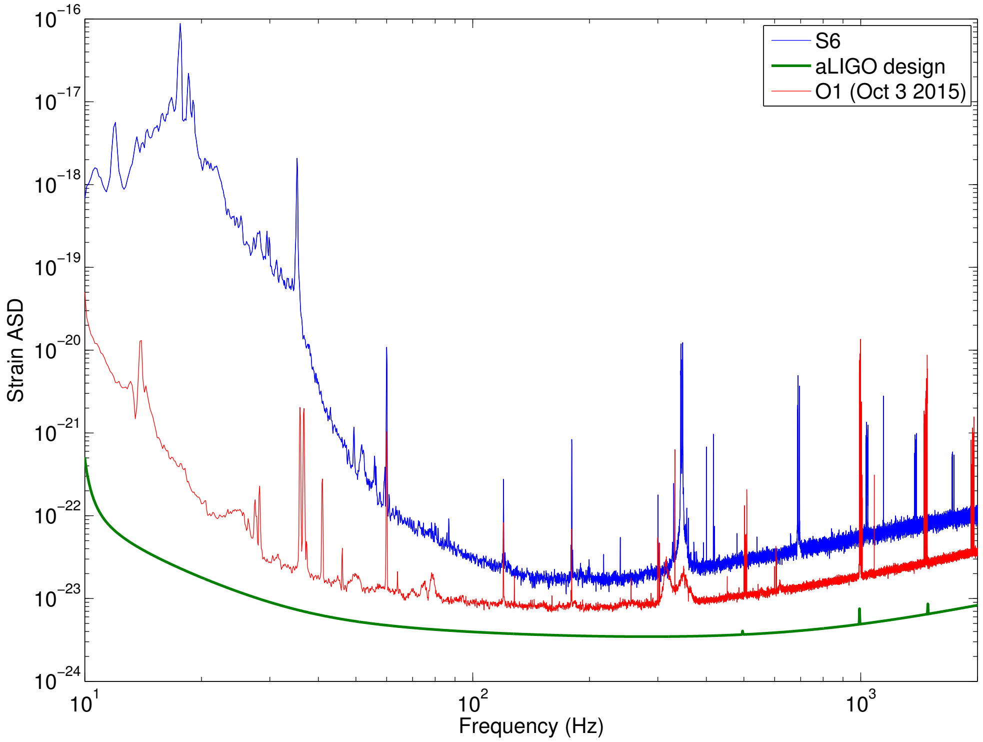

Figure 6.21: Comparison of calibrated S6, calibrated O1, and aLIGO design sensitivities. The analysis in this chapter was performed using data from the S6 instrument state (blue curve); the red O1 curve is the current instrument state, taken from H1 data on October 3 2015. The green curve is the aLIGO design senstivity, expected to be operational in 2017. S6 calibrated and aLIGO design curves from LIGO Lab 2015 [101], O1 calibrated curve from LIGO Lab 2015 [95].

Recalling the figure of merit used to select a data stretch for optimal sensitivity, Equation 6.13, the sensitivity of a fully coherent continuous wave search is inversely proportional to the power spectral density of interferometer noise. At the most sensitive frequencies, O1 data is already a factor of two more sensitive than iLIGO data. Improvements and upgrades through the aLIGO operation cycle will likely end in a factor of 10 improvement over iLIGO data.

Making the naive assumption that this improvement will translate directly into pulsar results, strains as low as 3×10^{-26} could be observed at the final aLIGO design sensitivity, corresponding to sensitivity to neutron stars with ellipticities of order 10^{-6}. At this scale, detection of gravitational waves from canonical neutron stars seems plausible. Of particular interest to directed pulsar searches is the reduction of the noise floor at low frequencies. Upgrades to the seismic isolation and suspension systems allow analysis of data at frequencies as low as 10 Hz. The potential sensitivity to pulsars with spin frequencies as low as 5 Hz includes a greater number of potential undiscovered galactic pulsars.

6.9.3 Extension to Binary Systems

Although this search considered only isolated neutron stars, the inclusion of sources in binary systems would be a powerful extension to the analysis. The modulation of pulsar signal due to its orbit around a binary companion is known to confound the detection of gamma-ray pulsars; to date, only one binary pulsar system, PSR J1311-3430, has been discovered through blind search of gamma-ray pulsations [65]. Members of the Einstein@Home group who made this discovery have suggested that such pulsar binaries are a more promising source for a blind gravitational wave search.

At this time, no templated gravitational wave analysis method exists to search for a binary system with unknown parameters over an uncertainty region. However, there exists a method that is potentially adaptable to this problem. The TwoSpect pipeline, developed for all-sky searches for binary pulsar system, uses a double Fourier transform technique to search over both the frequency of the pulsar and its modulation due to orbit of a binary partner [5]. The pipeline was adapted to be used in a targeted search for gravitational waves from the X-ray binary Scorpius X-1 [115], and has the best sensitivity of any technique that allows uncertainty in its parameters [170]. However, preliminary analysis showed that in its current form, a templated TwoSpect search for a source with unknown parameters and set sky position is computationally unfeasible. Work is ongoing to improve the sensitivity and efficiency of the TwoSpect code [77]. With these improvements, future adaptation to directed searches for unknown binary systems may become possible.

6.9.4 Summary of Work

This pilot search is an application of the fully-coherent resampled $\mathcal{F}$-statistic algorithm to a new and potentially interesting source of candidate gravitational wave emitters. As previous coherent searches for continuous waves only considered single sky locations, this search required the adaptation of the algorithm to cover small sky regions. This tiled resampled coherent $\mathcal{F}$-statistic is more sensitive than the loosely-coherent Spotlight search over small sky regions, and allows for consideration of potential sources with significant uncertainty regions, such as the Fermi 3FGL unassociated point sources. The selection of candidate 3FGL sources, design of the search, and adaptation of the algorithm are original to this work.

CHAPTER VII

Conclusions

7.1 Scientific Impact

Advanced LIGO began taking data on September 18 2015 at 15:00:00 UTC, ushering in a new era of interferometric gravitational wave experiments. At the beginning of its first operating run, the two-detector aLIGO network was sensitive to binary neutron star collisions beyond 70 Mpc, covering a spatial volume over 20 times that of the initial LIGO instruments. This achievement took years of research, development, installation, and commissioning. The incremental interferometer commissioning tests discussed in Chapter IV were essential to the success of interferometer locking; the integration issues discovered during the tests, such as the optical coating issues circumvented by the WFS system, would have negatively impacted interferometer stability.

In the Advanced LIGO era, a new emphasis has been placed on joint gravitational and electromagnetic observations. Advanced LIGO has partnered with over 60 electromagnetic astronomy projects covering wavelengths from radio to gamma ray to search for electromagnetic transients associated with gravitational wave events [44]. As aLIGO data is taken, candidate gravitational wave events with a false alarm rate less than one per month are shared with electromagnetic partners [45]. The first new LIGO data since 2010 provides the opportunity to make new and more sensitive measurements of Fermi unassociated sources. The pilot search discussed in Chapter VI is ready to search for gravitational wave signals and contribute gravitational wave observations to the search for gamma-ray pulsars.

7.2 Advanced LIGO and Beyond

The improvements made from the iLIGO instrument give aLIGO the astrophysical reach to make the first direct gravitational wave detection. The estimated detection rates for binary neutron star inspirals range from 0.01 - 10 events per $\mathrm{Mpc}^{-3}\mathrm{Myr}^{-1}$ [11], corresponding to a range of 0.003 to 3 events per year at the current range of 70 Mpc. At these rates, accumulating the four events set as the threshold for open sharing of gravitational wave triggers [45] could take anywhere from 14 months to over a thousand years. The sensitivity of gravitational wave instruments must be increased to advance the progress of gravitational wave astronomy.

Between the aLIGO observing runs, the input power will be increased from 25 W to 125 W, increasing the stored power in the arms from 100 kW [78] to 710 kW [101]. This will allow aLIGO to reach its design range of 200 Mpc, with an event rate from 0.08 to 80 binary neutron star coalesences per year. Further improvements are beyond the scope of the Advanced LIGO project, but research and development is in progress to further expand the range of gravitational wave interferometry. As discussed in Chapter III, there are two noise sources that limit the effectiveness of power increases; the thermal noise contribution increases with stored power, and the balance between shot noise and radiation pressure noise sets a standard quantum limit on sensitivity. Research is in progress to reduce thermal noise through coatings research and cryogenic cooling of test masses, and audio-band frequency-dependent squeezing has recently been demonstrated by the LIGO group at the Massachusetts Institute of Technology [126].

The field of gravitational wave interferometry stands on the verge of a new era of discovery, operating the most sensitive instruments ever made, analyzing the most sensitive data ever taken. It is a time of great uncertainty and great excitement, full of anticipation and promise. The first direct gravitational wave detection may arrive soon. What comes after detection - a new field of astronomy, bringing new insights into some of the strangest and most extreme objects in the universe - is more exciting still.

APPENDICES

APPENDIX A

Optical Table Layout for Arm Length Stabilization Wavefront Sensors

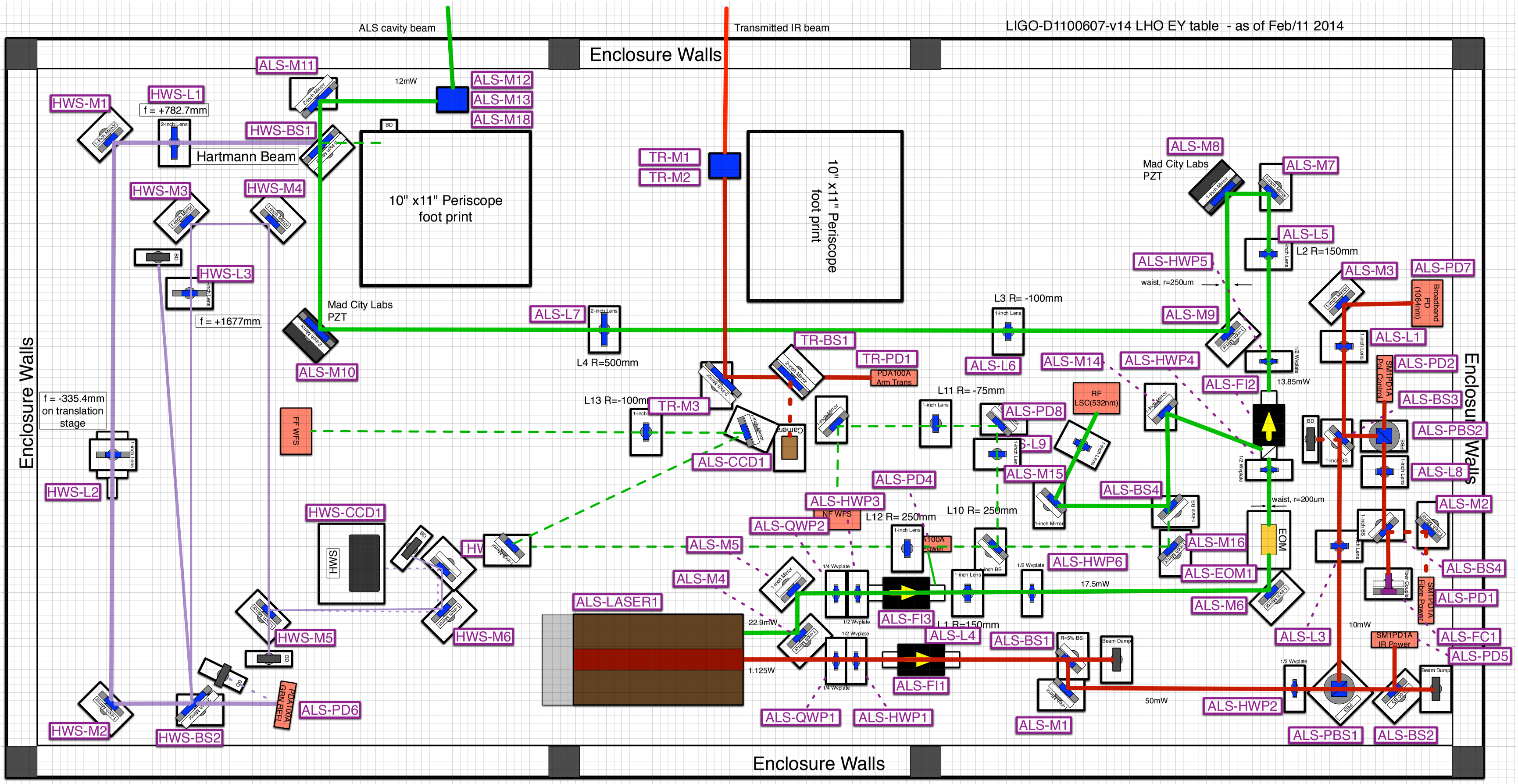
LIGO-D1100607-v14 LHO EY table - as of Feb/11 2014
ALS cavity beam
Transmitted IR beam
Enclosure Walls
Enclosure Walls
Enclosure Walls
Enclosure Walls
12mW
ALS-M11
ALS-M12
ALS-M13
ALS-M18
HWS-M1
HWS-L1
f = +782.7mm
HWS-BS1
Hartmann Beam
10" x11" Periscope foot print
10" x11" Periscope foot print
BD
HWS-M3
HWS-M4
HWS-L3
f = +1677mm
Mad City Labs PZT
ALS-M10
ALS-L7
L4 R=500mm
TR-M1
TR-M2
TR-BS1
TR-PD1
PDA100A Arm Trans
TR-M3
L13 R=-100mm
FF WFS
ALS-CCD1
Camera
f = -335.4mm on translation stage
HWS-L2
HWS-CCD1
HWS
HWS-M5
HWS-M6
HWS-M2
HWS-BS2
PDA100A GRN REFL
ALS-PD6
ALS-LASER1
ALS-M4
ALS-M5
ALS-QWP2
ALS-HWP3
NF WFS
ALS-PD4
L12 R= 250mm
PDA100A Power
22.9mW
1.125W
1/4 Wvplate
1/2 Wvplate
ALS-FI3
ALS-FI1
ALS-QWP1
ALS-HWP1
ALS-L4
L1 R=150mm
ALS-BS1
R=5% BS
Beam Dump
ALS-M1
50mW
ALS-HWP2
ALS-PBS1
ALS-BS2
L10 R= 250mm
L11 R= -75mm
ALS-L6
L3 R= -100mm
ALS-PD8
ALS-L9
ALS-M15
RF LSC(532nm)
ALS-M14
ALS-HWP4
ALS-BS4
ALS-HWP6
17.5mW
ALS-M16
ALS-EOM1
EOM
waist, r=200um
ALS-M6
ALS-L3
ALS-FI2
13.85mW
ALS-M9
ALS-HWP5
waist, r=250um
Mad City Labs PZT
ALS-M8
ALS-M7
ALS-L5
L2 R=150mm
ALS-M3
ALS-PD7
Broadband PD (1064nm)
ALS-L1
ALS-PD2
SM1PD1A Pol. Control
ALS-BS3
ALS-PBS2
ALS-L8
ALS-M2
ALS-BS4
ALS-PD1
SM1PD1A Fibre Power
ALS-FC1
ALS-PD5
SM1PD1A IR Power
10mW
1-inch Lens
1-inch BS
2-inch Lens
Fiber Coupler

APPENDIX B

Computational Cost for 3FGL Searches

The following table gives the maximum frequency to which a source can be searched with N templates, $f_{\max}^{(N)}$ and the estimated cost in CPU-months required for the search.

Source Name	Galactic Latitude	$f^{(1)}_{\mathrm{max}}$ (Hz)	CPU-months	$f^{(3)}_{\mathrm{max}}$ (Hz)	CPU-months	$f^{(5)}_{\mathrm{max}}$ (Hz)	CPU-months
3FGL J1155.3-1112	49.3222	778.5	24.6988	830.8	46.7913	1000.0	223.7118
3FGL J0312.7-2222	-57.6824	703.9	16.4835	768.0	37.1988	1000.0	257.4911
3FGL J0843.4+6713	35.6055	650.7	12.0223	808.7	62.2804	1000.0	255.6410
3FGL J1129.0+3758	69.5961	637.1	11.0443	691.6	23.9825	1000.0	284.4327
3FGL J1549.9-3044	18.1415	603.1	8.8603	636.1	15.2039	1000.0	297.5651
3FGL J2006.6+0150	-15.7820	588.8	8.0459	619.2	13.4571	1000.0	301.4444
3FGL J0725.4-5007	-15.3940	555.0	6.3444	631.0	19.1882	1000.0	303.2955
3FGL J1130.7-7800	-15.8129	534.8	5.4659	614.4	17.7076	1000.0	307.2108
3FGL J1544.6-1125	32.9844	514.0	4.6600	588.8	14.8177	1000.0	311.8236
3FGL J2024.8-2331	-30.3613	491.0	3.8764	544.3	9.8476	982.1	294.1827
3FGL J2333.0-5525	-58.3470	475.1	3.3956	525.5	8.4897	950.3	257.8956
3FGL J2144.6-5640	-45.7486	472.9	3.3328	523.5	8.3828	945.8	252.9922
3FGL J2209.8-0450	-45.5583	457.0	2.9043	539.9	11.2268	914.1	218.0535
3FGL J2244.6+2503	-29.5328	435.0	2.3812	514.6	9.2833	870.0	178.7670
3FGL J1632.8+3838	42.8468	432.6	2.3288	504.1	8.2707	865.2	175.3822
3FGL J0251.1-1829	-61.1657	423.3	2.1337	485.0	6.8006	846.7	161.3402

3FGL J2022.2-7220	-32.5962	416.7	2.0029	430.2	2.8259	833.4	153.7776
3FGL J1221.5-0632	55.5518	413.6	1.9435	545.1	13.8176	827.3	141.9317
3FGL J1824.2-5427	-18.0392	411.0	1.8948	452.3	4.5683	822.1	144.3221
3FGL J1810.7+5335	27.4063	401.1	1.7176	514.6	10.6106	802.2	126.4907
3FGL J2043.6+0001	-24.7194	383.6	1.4350	478.0	7.5692	767.2	106.6254
3FGL J0609.7-1841	-17.3860	382.1	1.4126	437.4	4.4786	764.3	107.0038
3FGL J0430.1-3103	-42.5319	379.5	1.3742	419.3	3.4125	759.1	104.7418
3FGL J0330.6+0437	-40.1435	371.7	1.2639	467.8	7.0437	743.5	93.7636
3FGL J2131.1-6625	-40.2745	369.3	1.2313	427.0	4.1667	738.6	93.1006
3FGL J1722.7-0415	17.5166	356.7	1.0705	456.0	6.4954	713.4	79.0769
3FGL J1203.9-1745	43.6546	347.3	0.9612	407.2	3.5532	694.6	72.5587
3FGL J1301.5+3333	83.2058	341.9	0.9024	391.5	2.8689	683.8	68.4460
3FGL J2047.9-3119	-37.3789	341.0	0.8928	503.5	11.0809	682.0	62.2307
3FGL J2044.0+1035	-19.1962	328.6	0.7689	332.1	0.8696	657.2	59.4169
3FGL J1421.0-2431	34.0058	324.3	0.7291	344.0	1.3166	648.6	56.0278
3FGL J1628.1+0254	32.9081	316.0	0.6566	361.9	2.0913	632.0	49.8843
3FGL J1544.1-2555	22.6115	310.0	0.6077	453.9	7.2620	620.1	42.6692

3FGL J1346.2-2608	35.1212	309.3	0.6022	398.6	3.8201	618.7	44.5344
3FGL J1258.4+2123	84.0382	305.0	0.5691	373.5	2.7280	610.1	42.6884
3FGL J2024.6+0309	-19.0435	304.3	0.5639	401.1	4.0250	608.7	41.4149
3FGL J0749.5+1320	18.8201	297.5	0.5147	359.2	2.2740	595.0	38.7274
3FGL J2250.6+3308	-23.2571	295.7	0.5022	324.5	1.1883	591.4	38.4819
3FGL J2056.3-5925	-38.8560	294.2	0.4920	339.8	1.6567	588.4	37.3754
3FGL J0048.1-6343	-53.3927	288.2	0.4527	398.6	4.1192	576.4	32.6764
3FGL J1813.6-6845	-21.8461	288.0	0.4514	351.3	2.1172	576.0	33.9125
3FGL J2259.9-1553	-61.8380	273.1	0.3642	304.6	0.9700	546.2	27.8873
3FGL J0935.2+0903	40.3669	267.7	0.3359	339.2	1.9500	535.5	25.0537
3FGL J2331.9-1609	-68.5669	266.5	0.3299	342.8	2.0762	533.0	24.4777
3FGL J1309.0+0347	66.2871	264.1	0.3180	314.0	1.2841	528.3	24.1021
3FGL J1829.2+3229	18.5189	257.1	0.2852	267.9	0.4403	514.3	22.1104
3FGL J0456.2-6924	-35.2829	247.8	0.2457	378.5	3.5877	495.6	16.9119
3FGL J1804.1+2532	21.1678	244.9	0.2343	257.3	0.3899	489.8	18.1513
3FGL J2010.0-2120	-26.3986	237.0	0.2051	332.1	1.9972	474.0	14.8052
3FGL J1421.8-7920	-17.2327	233.5	0.1931	284.4	0.9009	467.0	14.5987

3FGL J2253.1-1237	-58.7697	230.8	0.1842	280.6	0.8506	461.6	13.9376
3FGL J1858.0-5423	-22.6789	214.5	0.1368	309.1	1.5283	429.1	9.7943
3FGL J1528.7-2247	27.2713	214.3	0.1363	295.0	1.2196	428.6	9.9490
3FGL J1911.1-5318	-24.2908	207.2	0.1189	254.6	0.5848	414.5	9.0170
3FGL J1936.6-4215	-25.8358	197.7	0.0982	256.8	0.6553	395.5	7.3508
3FGL J2006.5-0939	-21.0295	197.3	0.0974	233.3	0.3825	394.7	7.4694
3FGL J1304.6+1200	74.5619	189.2	0.0821	269.7	0.8743	378.5	5.9419
3FGL J1815.1+5919	27.6275	186.4	0.0773	253.0	0.6473	372.9	5.7130
3FGL J0010.5-1425	-74.1117	183.8	0.0730	264.7	0.8169	367.7	5.2620
3FGL J0016.5+1713	-44.8503	183.0	0.0717	223.1	0.3382	366.0	5.4735
3FGL J2029.5-4232	-35.4883	183.0	0.0717	228.2	0.3845	366.0	5.4426
3FGL J1403.1+1304	68.1186	182.8	0.0714	282.0	1.1011	365.7	4.9464
3FGL J0905.8-2127	16.9488	180.2	0.0673	265.7	0.8430	360.5	4.7999
3FGL J1630.2-1052	24.7818	168.1	0.0507	223.0	0.3794	336.2	3.7942
3FGL J1741.4+0938	19.8906	164.0	0.0458	203.6	0.2405	328.1	3.5079
3FGL J1817.7+2530	18.3023	161.1	0.0425	198.9	0.2169	322.3	3.2691
3FGL J0420.4+1448	-24.2149	156.7	0.0380	213.2	0.3246	313.5	2.8366

3FGL J1239.1-1158	50.7814	154.8	0.0361	179.9	0.1283	309.7	2.8209
3FGL J1727.4+0634	21.6464	138.2	0.0226	165.3	0.0966	276.4	1.7717
3FGL J0240.0-0253	-54.4921	136.7	0.0216	180.9	0.1619	273.5	1.6517
3FGL J1806.2+2744	21.5120	135.7	0.0210	159.8	0.0815	271.5	1.6539
3FGL J1408.0-2924	30.5678	110.0	0.0087	209.0	0.3520	220.1	0.4961
3FGL J1002.0-2837	21.0263	79.8	0.0021	121.8	0.0359	159.7	0.1744

BIBLIOGRAPHY

BIBLIOGRAPHY

[1] J. Aasi et al. Directed search for continuous gravitational waves from the Galactic center. *Phys Rev D*, 88:102002, Nov 2013.

[2] J. Aasi et al. Einstein@Home all-sky search for periodic gravitational waves in LIGO S5 data. *Phys Rev D*, 87, 2013.

[3] J. Aasi et al. Enhanced sensitivity of the LIGO gravitational wave detector using squeezed states of light. *Nat Photonics*, 7:613–619, 2013.

[4] J. Aasi et al. Application of a hough search for continuous gravitational waves on data from the 5th ligo science run. *Classical Quantum Grav*, 31, 2014.

[5] J. Aasi et al. First all-sky search for continuous gravitational waves from unknown sources in binary systems. *Phys Rev D*, 90, 2014.

[6] J. Aasi et al. Gravitational waves from known pulsars: Results from the initial detector era. *Astrophys J*, 785, 2014.

[7] J. Aasi et al. Searches for continuous gravitational waves from nine young supernova remnants. *arXiv*, 2014.

[8] J. Aasi et al. Advanced LIGO. *Classical Quantum Grav*, 32, 2015.

[9] J. Aasi et al. A search of the Orion spur for continuous gravitational waves using a ”loosely coherent” algorithm on data from LIGO interferometers. arxiv:1510.03474, 2015.

[10] J. Abadie et al. First search for gravitational waves from the youngest known neutron star. *Astrophys J*, 722, 2010.

[11] J. Abadie et al. Predictions for the rates of compact binary coalescences observable by ground-based gravitational-wave detectors. *Classical Quantum Grav*, 27, 2010.

[12] J. Abadie et al. All-sky search for periodic gravitational waves in the full S5 LIGO data. *Phys Rev D*, 85, 2011.

[13] J. Abadie et al. Beating the spin-down limit on gravitational wave emission from the Vela pulsar. *Astrophys J*, 737, 2011.

[14] J. Abadie et al. A gravitational-wave observatory operating beyond the quantum shot-noise limit. *Nat Phys*, 7:962–965, 2011.

[15] B. Abbott et al. LIGO: The Laser Interferometer Gravitational Wave Observatory. *Rep Prog Phys*, 72, 2009.

[16] B. Abbott et al. Searches for gravitational waves from known pulsars with Science Run 5 LIGO data. *Astrophys J*, 713:671–685, 2010.

[17] A. Abdo et al. Detection of 16 gamma-ray pulsars through blind frequency searches using the Fermi LAT. *Science*, 325:840–844, 2009.

[18] M. Abernathy et al. Einstein gravitational wave Telescope conceptual design study. ET-0106C-10, 2011.

[19] A. Abramovici et al. LIGO: The Laser Interferometer Gravitational-Wave Observatory. *Science*, 256, 1992.

[20] T. Accadia et al. Virgo: a laser interferometer to detect gravitational waves. *J Instrum*, 7, 2012.

[21] F. Acernese et al. The variable finesse locking technique. *Classical Quantum Grav*, 23, 2006.

[22] F. Acernese et al. Advanced Virgo: a second-generation interferometric gravitational wave detector. *Classical Quantum Grav*, 32(2), 2015.

[23] F. Acero et al. Fermi Large Area Telescope third source catalog. *Astrophys J Suppl S*, 218(23), 2015.

[24] R. Adhikari. Gravitational radiation detection with laser interferometry. *Rev Mod Phys*, 86, 2014.

[25] Advanced LIGO Systems Group. Advanced LIGO system description. Technical Report T010075-v3, LIGO Laboratory, 2001.

[26] P. Amaro-Seoane et al. eLISA/NGO: Astrophysics and cosmology in the millihertz regime. arXiv:1201.3621, 2012.

[27] D. Z. Anderson. Alignment of resonant optical cavities. *Appl Optics*, 23(17), 1984.

[28] N. Andersson et al. Gravitational waves from neutron stars: Promises and challenges. *General Relat Gravit*, 43, 2011.

[29] N. Andersson and K. Kokkotas. The r-mode instability in rotating neutron stars. *Int J Mod Phys D*, 10, 2001.

[30] K. Arai et al. New signal extraction scheme with harmonic demodulation for power-recycled Fabry-Perot-Michelson inteferometers. *Phys Lett A*, 273:15–24, 2000.

[31] K. Arai, Y. Michimura, and K. Kawabe. alog 9520. `https://alog.ligo-wa.caltech.edu/aLOG/index.php?callRep=9520`, 2014.

[32] M. Arain and G. Mueller. Design of the Advanced LIGO recycling cavities. *Opt Express*, 16, 2008.

[33] H. Armandula, G. Billingsley, G. Harry, and W. Kells. Core optics components final design. Technical Report E080494, LIGO Laboratory, 2008.

[34] M. Armano et al. Free-flight experiments in LISA Pathfinder. *J Phys Conf Ser*, 610(1):012006, 2015.

[35] W. Atwood et al. A time-differencing technique for detecting radio-quiet gamma-ray pulsars. *Astrophys J Lett*, 652:L49–L52, 2006.

[36] W. B. Atwood et al. The Large Area Telescope on the Fermi gamma-ray space telescope mission. *Astrophys J*, 697(2):1071, 2009.

[37] M. J. Benacquista. Relativistic binaries in globular clusters. *Liv Rev Relativ*, 2006.

[38] G. Billingsley. ETM02 characterization. Technical Report E1000776, LIGO Laboratory, 2010.

[39] G. Billingsley. ETM04 characterization. Technical Report T1400083, LIGO Laboratory, 2014.

[40] G. Billingsley and L. Zhang. ETM02 absorption result and burn report. Technical Report T1100337, LIGO Laboratory, 2011.

[41] E. D. Black. An introduction to Pound-Drever-Hall frequency stabilization. *Am J Phys*, 69, 2000.

[42] R. Bondarescu et al. Spinning down newborn neutron stars: Nonlinear development of the r-mode instability. *Phys Rev D*, 79, 2009.

[43] P. Brady et al. Searching for periodic sources with LIGO. *Phys Rev D*, 57, 1998.

[44] M. Branchesi. Observational prospects in the electromagnetic domain of gravitational wave sources. In *Frontier Objects in Astrophysics and Particle Physics*, 2014.

[45] M. Branchesi, P. Shawhan, and L. Price. EM follow-up: partner status, target rate of alerts, and testing plans. Technical Report G1500323, LIGO Laboratory, 2015.

[46] A. Brooks. Merger and collision insurance: Advanced LIGO Thermal Compenation System (TCS). Technical Report G1101270, LIGO Laboratory, 2012.

[47] A. Brooks. Results from thermal compensation testing in the One Arm Test. Technical Report T1200465, LIGO Laboratory, 2012.

[48] A. Brooks, P. Willems, M. Jacobson, and C. Vorvick. Ring heater and Hartmann sensor testing as part of commissioning Advanced LIGO's first arm cavity. Technical Report T1100127, LIGO Laboratory, 2011.

[49] A. Buonanno and Y. Chen. Quantum noise in second-generation, signal-recycled laser interferometer gravitational wave detectors. *Phys Rev D*, 64, 2001.

[50] B. Burke and F. Graham-Smith. *An Introduction to Radio Astronomy.* Cambridge University Press, 2002.

[51] H. Callen and T. Welton. Irreversibility and generalized noise. *Phys Rev*, 83(1), 1951.

[52] S. Caride. *Search for continuous gravitational waves from globular cluster NGC6544 using barycentric resampling.* PhD thesis, University of Michigan, 2015.

[53] T.-P. Cheng. *Relativity, Gravitation, and Cosmology: A Basic Introduction.* Oxford University Press, 2005.

[54] C. Clark et al. PSR J1906+0722: an elusive gamma-ray pulsar. *Astrophys J Lett*, 809(1), 2015.

[55] C. F. D. S. Costa and O. D. Aguiar. Spherical gravitational wave detectors: MiniGRAIL and Mario Schenberg. *J Phys Conf Ser*, 484(1):012012, 2014.

[56] J. Creighton and W. Anderson. *Gravitational-wave physics and astronomy: an introduction to theory, experiment, and data analysis.* Wiley-VCH, 2011.

[57] T. Creighton. Tumbleweeds and airborne gravitational noise sources for LIGO. *Classical Quantum Grav*, 25(12), 2000.

[58] C. Cutler and B. F. Schutz. Generalized F-statistic: Mulitple detectors and multiple gravitational wave pulsars. *Phys Rev D*, 72, 2005.

[59] R. Dannenberg. Advanced LIGO End Test Mass (ETM) coating specification. Technical Report E0900068, LIGO Laboratory, 2008.

[60] K. Dooley et al. Angular control of optical cavities in a radiation-pressure-dominated regime: the Enhanced LIGO case. *J Opt Soc Am*, 2013.

[61] R. Drever et al. Laser phase and frequency stabilization using an optical resonator. *Appl Phys B-Lasers O*, 31:97–105, 1983.

[62] R. Drever et al. Laser phase and frequency stabilization using an optical resonator. *Appl Phys B-Lasers O*, 31:97–105, 1983.

[63] S. Dwyer. alog 9191. `https://alog.ligo-wa.caltech.edu/aLOG/index.php?callRep=9191`, 2014.

[64] S. Dwyer et al. Gravitational wave detector with cosmological reach. *Phys Rev D*, 91, 2015.

[65] H. P. et. al. Binary millisecond pulsar discovery via gamma-ray pulsations. *Science*, 338, 2012.

[66] P. S. et al. Eight γ-ray pulsars discovered in blind frequency searches of Fermi LAT data. *Astrophys J*, 725:571–584, 2010.

[67] M. Evans et al. Lock acquisition of a gravitational-wave interferometer. *Opt Lett*, 27(8), 2002.

[68] P. Fritschel. Common mode servo block diagram. Technical Report D1002416, LIGO Laboratory, 2011.

[69] P. Fritschel and V. Frolov. Documentation of two-hour lock milestone for L1. Technical Report L1400119, LIGO Laboratory, 2014.

[70] P. Fritschel and V. Frolov. Integration testing report for the L1 DRMI. Technical Report T1400053, LIGO Laboratory, 2014.

[71] P. Fritschel and D. Sigg. Documentation of two-hour lock milestone for H1. Technical Report L1500028, LIGO Laboratory, 2015.

[72] V. Frolov and P. Fritschel. Summary of the L1 Input Mode Cleaner testing. Technical Report L1300018, LIGO Laboratory, 2013.

[73] LIGO optics. `https://galaxy.ligo.caltech.edu/optics/`, 2015.

[74] L. Gendelev et al. The contribution of Fermi gamma-ray pulsars to the local flux of cosmic-ray electrons and positrons. *J Cosmol Astropart P*, 2010, 2010.

[75] M. Gertsenshtein and V. Pustovoit. On the detection of low frequency gravitational waves. *Sov Physics JETP-USSR*, 16(2):433–435, 1963.

[76] N. K. Glendenning. *Compact Stars: Nuclear Physics, Particle Phyiscs, and General Relativity.* Springer-Verlag, 1997.

[77] E. Goetz and K. Riles. Coherently combining short data segments for all-sky semi-coherent continuous gravitational wave searches. In preparation, 2015.

[78] E. Hall. Circulating arm power from tidal offloading. `https://alog.ligo-wa.caltech.edu/aLOG/index.php?callRep=20347`, 2015.

[79] O. Hamil. Braking index of isolated pulsars: open questions and ways forward. arxiv:1503.09110, 2015.

[80] A. Harding. Polar cap and outer gap models. `http://heasarc.gsfc.nasa.gov/docs/cgro/images/epo/gallery/index.html`.

[81] G. Harry. Advanced LIGO Input Test Mass (ITM) coating specification. Technical Report E0900041, LIGO Laboratory, 2008.

[82] G. Harry et al. Titania-doped tantala/silica coatings for gravitational-wave detection. *Classical Quantum Grav*, 24:405–415, 2007.

[83] B. Haskell et al. Are neutron stars with crystalline color-superconducting cores relevant for the LIGO experiment? *Phys Rev Lett*, 99, 2007.

[84] M. Heintze. TCS installation and commissioning progress. Technical Report G1400960, LIGO Laboratory, 2014.

[85] J. W. Hessels et al. A radio pulsar spinning at 716 Hz. *Science*, 311(5769), 2006.

[86] J. D. Jackson. *Classical Electrodynamics*. Wiley, 3 edition, 1999.

[87] P. Jaranowski and A. Królak. *Analysis of Gravitational-Wave Data*. Cambridge University Press, 2009.

[88] P. Jaranowski and A. Królak. Searching for gravitational waves from known pulsars using the F and G statistics. *Classical Quantum Grav*, 27, 2010.

[89] N. K. Johnson-McDaniel and B. J. Owen. Maximum elastic deformations of relativistic stars. *Phys Rev D*, 88, 2013.

[90] I. Jones. R-modes and gravitational wave searches: frequencies and frequency derivatives. Technical Report T1100355, LIGO Scientific Collaboration, 2011.

[91] K. Kawabe. H2 One Arm Test beam geometry. Technical Report T1200200, LIGO Laboratory, 2012.

[92] K. Kawabe. alog 11437. `https://alog.ligo-wa.caltech.edu/aLOG/index.php?callRep=11437`, 2014.

[93] S. Kawamura. Current status of KAGRA. G1500410.

[94] S. Kawamura et al. The Japanese space gravitational wave antenna: DECIGO. *Classical Quantum Grav*, 28, 2011.

[95] J. Kissel. H1 calibrated sensitivity spectra Oct 1 2015 (representative for start of O1). Technical Report G1501223-v2, LIGO Laboratory, 2015.

[96] H. Kogelnik and T. Li. Laser beams and resonators. *Appl Optics*, 5(10), 1966.

[97] M. Kramer et al. Tests of general relativity from timing the double pulsar. *Science*, 314(5796):97–102, 2006.

[98] K. Kuroda. Status of LCGT. *Classical Quantum Grav*, 23, 2006.

[99] D. Lai et al. Hydrodynamic instability and coalescence of close binary systems. *Astrophys J Lett*, 406L:63L, 1993.

[100] J. Leigh. *Control Theory*. Institution of Engineering and Technology, 2 edition, 2004.

[101] LIGO Scientific Collaboration. Instrument science white paper. Technical Report T1500290, LIGO Laboratory, 2015.

[102] V. M. Lipunov. *Astrophysics of Neutron Stars*. Springer-Verlag, 1992.

[103] D. Lorimer. Radio pulsar populations. In N. Rea and D. Torres, editors, *High-Energy Emission from Pulsars and their Systems*. Springer-Verlag, 2011.

[104] D. Lorimer et al. The Parkes multibeam pulsar survey - VI. discovery and timing of 142 pulsars and a galactic population analysis. *Mon Not R Astron Soc*, 372:777–800, 2006.

[105] LSC Data Analysis Software Working Group. LALSuite. `https://www.lsc-group.phys.uwm.edu/daswg/projects/lalsuite.html`, 2010–2015.

[106] LSC/Virgo Continuous Wave Search Group. All-sky searches for isolated spinning neutron stars. Technical Report T1400191, LIGO-Virgo Collaboration, 2014.

[107] LSC/Virgo Continuous Wave Search Group. Directed searches for gravitational waves from isolated neutron stars. Technical Report T1400599, LIGO-Virgo Collaboration, 2014.

[108] A. Lyne. The double pulsar system J0737-3039. *New Astron Rev*, 54:135–139, 2010.

[109] A. Lyne et al. A double-pulsar system: A rare laboratory for relativistic gravity and plasma physics. *Science*, 303(5661):1153–1157, 2004.

[110] A. Lyne and F. Graham-Smith. *Pulsar Astronomy*. Cambridge University Press, 2012.

[111] M. Maggiore. *Gravitational Waves Volume 1: Theory and Experiments*. Oxford University Press, 2008.

[112] R. Manchester et al. The Australia Telescope National Facility pulsar catalog. *Astron J*, 2005.

[113] R. Manchester et al. The Australia Telescope National Facility pulsar catalog. `http://www.atnf.csiro.au/people/pulsar/psrcat/`, 2015.

[114] L. Matone. An overview of control theory and digital signal processing. Technical Report G1100863, LIGO Scientific Collaboration, 2011.

[115] G. Meadors, E. Goetz, and K. Riles. TwoSpect: search for a simulated Scorpius X-1. In preparation, 2015.

[116] A. Melatos and D. Payne. Gravitational radiation from an accreting millisecond pulsar with a magnetically confined mountain. *Astrophys J*, 623, 2005.

[117] J. Miller et al. Prospects for doubling the range of advanced LIGO. *Phys Rev D*, 91, 2015.

[118] J. Ming. Optimization of search set up for CW directed targets updates. Technical Report G1500321, LIGO Laboratory, 2015.

[119] C. W. Misner, K. S. Thorne, and J. A. Wheeler. *Gravitation*. W.H. Freeman and Company, 1973.

[120] J. Mizuno et al. Resonant sideband extraction: a new configuration for interferometric gravitational wave detectors. *Phys Lett A*, 175:273–276, 1993.

[121] A. Mullavey. alog 10423. `https://alog.ligo-la.caltech.edu/aLOG/index.php?callRep=10423`, 2014.

[122] A. Mullavey. alog 10529. `https://alog.ligo-la.caltech.edu/aLOG/index.php?callRep=10529`, 2014.

[123] A. Mullavey et al. Arm-length stabilisation for interferometric gravitational-wave interferometers using frequency-doubled auxiliary lasers. *Opt Express*, 20(1), 2011.

[124] J. W. Murphy et al. A model for gravitational wave emission in neutrino-driven core-collapse supernovae. *Astrophys J*, 707, 2009.

[125] Nobelprize.org. Press release: The 1993 Nobel Prize in Physics. `http://www.nobelprize.org/nobel_prizes/physics/laureates/1993/press.html`, 1993.

[126] E. Oelker et al. Audio-band frequency-dependent squeezing. arxiv/1508.04700, 2015.

[127] M. Ohashi et al. Design and construction status of CLIO. *Classical Quantum Grav*, 20, 2003.

[128] R. O'Shaughnessy et al. Short gamma-ray bursts and binary mergers in spiral and elliptical galaxies: Redshift distribution and hosts. *Astrophys J*, 675:566–585, 2008.

[129] B. Owen. Maximum elastic deformations of compact stars with exotic equations of state. *Phys Rev Lett*, 95, 2005.

[130] B. Owen et al. Gravitational waves from hot young rapidly rotating neutron stars. *Phys Rev D*, 58, 1998.

[131] P. Patel et al. Implementation of barycentric resampling for continuous wave searches in gravitational wave data. *Phys Rev D*, 81, 2010.

[132] P. Peters and J. Mathews. Gravitational radiation from point masses in a Keplerian orbit. *Phys Rev*, 131(1):436–439, 1963.

[133] H. Pletsch et al. Discovery of nine gamma-ray pulsars in Fermi Large Area Telescope data using a new blind search method. *Astrophys J*, 744:105–125, 2012.

[134] H. Pletsch et al. Einstein@Home discovery of four young gamma-ray pulsars in Fermi LAT data. *Astrophys J*, 779, 2013.

[135] R. Pound. Electronic frequency stabilization of microwave oscillators. *Rev Sci Instrum*, 17:490, 1946.

[136] R. Prix. The F-statistic and its implementation in ComputeFstatistic_v2. T0900149.

[137] R. Prix. Gravitational waves from spinning neutron stars. In *Neutron Stars and Pulsars*. Springer-Verlag, 2009.

[138] R. Prix and B. Krishnan. Targeted search for continuous gravitational waves: Bayesian versus maximum-likelihood statistics. *Classical Quantum Grav*, 26, 2009.

[139] M. Rakhmanov et al. Dynamic resonance of light in Fabry-Perot cavities. *Phys Lett A*, 2002.

[140] M. Rakhmanov et al. Characterization of the LIGO 4 km Fabry-Perot cavities via their high-frequency responses to length and laser frequency variations. *Classical Quantum Grav*, 21, 2004.

[141] M. Rakhmanov, M. Evans, and H. Yamamoto. An optical vernier technique for in situ measurement of the length of long Fabry-Perot cavities. *Meas Sci Technol*, 10, 1999.

[142] V. Ravi et al. Does a "stochastic" background of graviational waves exist in the pulsar timing band? *Astrophys J*, 761(84), 2012.

[143] P. Ray et al. Radio searches of Fermi LAT sources and blind search pulsars: The Fermi Pulsar Search Consortium. arxiv:1205.3089, 2012.

[144] K. Riles. Gravitational waves: Sources, detectors, and searches. *Prog Part Nucl Phys*, 2012.

[145] B. Saleh and M. Teich. *Fundamentals of Photonics*. John Wiley and Sons, 2 edition, 2007.

[146] B. Sathyaprakash and B. F. Schutz. Physics, astrophysics, and cosmology with gravitational waves. *Living Rev Relativ*, 12(2), 2009.

[147] P. R. Saulson. *Fundamentals of Interferometric Gravitational Wave Detectors*. World Scientific Publishing, 1994.

[148] B. F. Schutz. Data processing, analysis, and storage for interferometric antennas. In D. Blair, editor, *The Detection of Gravitational Waves*. Cambridge University Press, 1991.

[149] D. Shoemaker. Advanced LIGO reference design. Technical Report M060056, LIGO Laboratory, 2006.

[150] D. Sigg. Common mode servo board. Technical Report D040180, LIGO Laboratory, 2004.

[151] D. Sigg. Common mode servo design. Technical Report T040148, LIGO Laboratory, 2004.

[152] D. Sigg. Common mode servo specifications. Technical Report E1200177, LIGO Laboratory, 2012.

[153] D. Sigg. Eliminating the ALS wavefront sensors. Technical Report E1200935, LIGO Laboratory, 2012.

[154] D. Sigg. Adding auto-alignment for ALS. Technical Report E1400071, LIGO Laboratory, 2014.

[155] D. Sigg and K. Kawabe. Executive summary of the LHO HIFO-XY test. Technical Report L1400110, LIGO Laboratory, 2014.

[156] D. Sigg, K. Kawabe, and P. Fritschel. Executive summary of the LHO HIFO-Y test. Technical Report L1300176, LIGO Laboratory, 2013.

[157] D. Sigg, K. Kawabe, B. Slagmolen, and P. Fritschel. Executive summary of the One Arm Test. Technical Report L1200261, LIGO Laboratory, 2012.

[158] N. Smith. Intro to thermal noise. G1500273, 2015.

[159] A. Staley et al. Achieving resonance in the Advanced LIGO gravitational-wave interferometer. *Classical Quantum Grav*, 31(24), 2014.

[160] stellarcollapse.org. Gravitational wave signal catalog. `stellarcollapse.org`, 2015.

[161] A. Stochino et al. Technique for in-situ measurement of free spectral range and transverse mode spacing of optical cavities. *Appl Optics*, 51(27), 2012.

[162] J. Taylor and J. Weisberg. A new test of general relativity: Gravitational radiation and the binary pulsar PSR 1913+16. *Astrophys J*, 253:908–920, 1982.

[163] J. Taylor and J. Weisberg. Further experimental tests of relativistic gravity using the binary pulsar PSR 1913+16. *Astrophys J*, 345:434–450, 1989.

[164] The Fermi Collaboration. Fermi Science Support Center. `http://fermi.gsfc.nasa.gov/ssc/`.

[165] A. Watts et al. Detecting gravitational wave emission from the known accreting neutron stars. *Mon Not R Astron Soc*, 389:839–868, 2008.

[166] J. Weber. Detection and generation of gravitational waves. *Phys Rev*, 17(1):306–313, 1960.

[167] J. Weisberg, D. Nice, and J. Taylor. Timing measurements of the relativistic pulsar PSR B1913+16. *Astrophys J*, 722:1030–1034, 2010.

[168] R. Weiss. Electromagnetically coupled broadband gravitational wave antenna. *Quarterly Progress Report, MIT Research Lab of Electronics*, 1972.

[169] K. Wette et al. Searching for gravitational waves from Cassiopeia A with LIGO. *Classical Quantum Grav*, 25, 2008.

[170] J. Whelan. Update on stage 2 of the Sco X-1 MDC. Technical Report G1501085, LIGO Laboratory, 2015.

[171] P. Willems, A. Brooks, M. Smith, and K. Mailand. Advanced LIGO Thermal Compensation System preliminary design. Technical Report T090034, LIGO Laboratory, 2009.

[172] B. Willke et al. The GEO600 gravitational wave detector. *Classical Quantum Grav*, 19, 2002.

[173] B. Willke et al. The GEO-HF project. *Classical Quantum Grav*, 23, 2006.